This is to certify that the

dissertation entitled

Effects of Nickel, Niobium and Titanium Fiber-Coatings
On the Interfacial Properties of NiAl-Al_2O_3 Composites

presented by

Richard L. Schalek

has been accepted towards fulfillment
of the requirements for

Ph.D. degree in Materials Science

Major professor

Date August 20, 1996

EFFECTS OF NICKEL, NIOBIUM, AND TITANIUM FIBER COATINGS ON THE INTERFACIAL PROPERTIES OF NiAl-Al_2O_3 COMPOSITES

by

Richard L. Schalek

A DISSERTATION

Submitted to
Michigan State University
in partial fulfillment of the requirements
for the degree of

DOCTOR of PHILOSOPHY

Department of Materials Science and Mechanics

1996

ABSTRACT

EFFECTS OF NICKEL, NIOBIUM, AND TITANIUM FIBER COATINGS ON THE INTERFACIAL PROPERTIES OF NiAl-Al_2O_3 COMPOSITES

By

Richard L. Schalek

An assessment of the effects of nickel, titanium, and niobium fiber coatings on the interfacial behavior of diffusion bonded NiAl-Al_2O_3 composites has been investigated. The three coating materials were chosen to provide a broad spectrum of coating-fiber chemical activity and to improve the normally poor high-temperature fiber-matrix adhesion. As-extracted fiber fragment distributions indicate a uniform distribution of fragments for the weakly chemically reactive uncoated and niobium-coated fibers, while the nickel and titanium coatings, representing highly reactive coatings, consisted only of short fragments. The effects of the fiber coatings on the fiber surface morphology were documented using scanning electron microscopy and atomic force microscopy. Small morphological changes occurred for the uncoated fiber composite, while the coated fibers showed significant increases in surface roughness.

The longitudinal thermal strain of small volume fraction, aligned composites (5- and 7-vol.%) were measured by dilatometry from room temperature to 1450 K. From these data, the nickel- and niobium-coated fiber composites showed distinct knees in the heating half-cycle, accompanied by hysteresis and residual compressive strains. This behavior indicates that compressive creep strains accumulated during the high temperature expansion, and hence, good fiber-matrix load transfer occurs. In contrast to this behavior, the uncoated fiber composite showed only a slight knee and small hysteresis strain, and no residual compressive strain, indicating poor high-temperature load transfer. The titanium-coated fiber composite displayed an intermediate behavior. Of the three fiber coating materials investigated, niobium emerges as the most favorable for increasing high-temperature fiber-matrix load transfer.

ACKNOWLEDGMENTS

The graduate study environment permits the forging of many lasting relationships. I have been fortunate to develop friendships with a number of people from a variety of different departments. I thank all of the following for being friends. From the Materials Science and Mechanics department Luiwen Chen, Zhewie Cai, Seungho Nam, Tony Ozzello, and Michelle Hlvacek. From the Chemical Engineering Department Jay Kalantar, Shri Iyer, and Brent Jones, and from the Mechanical Engineering Department, Todd Rachel. Finally, from the Physics and Astronomy Department Dr. R.M. Ronningen and Dr. N.O. Birge, and from the Center for Electron Optics Dr. Karen Klomparens.

The technical demands required of any scientific project are many. The personnel that train the students and provide a creative, problem solving environment, are sometimes under appreciated for their contributions to the work. With this in mind I thank the "Physic's Shop Guys", Tom Palazzoa, Tom Hudson , and Jim Muns for freely and willingly sharing with me their time, expertise and problem solving skills. The Composite Materials and Structures Center stands as an exemplary entity for conducting research. Thanks are required for the director of the center, Dr. L.T. Drzal, for providing and maintaining the facility. Also thanks to the manager of the facility, Mike Rich, for all of the technical help, walks in the woods, golf outings, and general good-guy behavior. I would also like to thank Brian Rook, for all his help and, in particular, for making a gold crown for my wisdom tooth. Two other people provided a great working atmosphere include Dr. Kevin Hook and Dr. Pedro Herrera.

I would also like to thank my advisory committee, consisting of Dr. M.J. Crimp, Dr. L.T. Drzal, Dr. D.S. Grummon, Dr. W. C. McHarris, and Dr. H. Schock for providing guidance and providing critical suggestions. I would particularly like to thank them for their patience while I completed this work. In addition, I thank my advisor Dr. D.S. Grummon for providing interesting conversations and for providing financial support. I would also like to thank my mother, who, lacking formal education, taught me the virtues of education, responsibility, loyalty, and commitment.

Finally, I would like to thank my wife, Dr. Diandra Leslie-Pelecky for her constant companionship, love, and devotion.

TABLE OF CONTENTS

LIST OF TABLES

LIST OF FIGURES

GLOSSARY OF SYMBOLS AND ABBREVIATIONS

Symbols (with units)

A	effective roughness amplitude (nm)
α_i	average coefficient of thermal expansion (CTE, K^{-1}); i stands for fiber (f) or matrix (m)
b	Burgers vector (nm)
β	load transfer parameter (unitless)
β'	proportionality constant for the interfacial shear strength (m^{-1})
c	crack flaw size (nm)
D	diffusion coefficient (m^2-s^{-1})
D_o	preexponential term (m^2-s^{-1})
E	elastic modulus (Pa)
E_m^*	hardening slope (matrix modulus above the yield point (Pa)
$\dot{\varepsilon}$	strain rate (s^{-1})
ε_i	strain; i stands for fiber (f) or matrix (m)
G	shear modulus (Pa)
G_c^*	strain energy release rate (J-m^{-2})
Γ_c	interface energy (J-m^{-2})
γ_i	surface energy; i stands for ceramic (c), metal (m), or metal-ceramic (mc) (J-m^{-2})
K	constant (Pa)
k	Boltzmann's constant (J-K^{-1})
K_{IC}	mode I critical stress intensity factor (Pa-$m^{-0.5}$)
K_τ	intrinsic matrix shear constant (Pa)
l	fiber length (mm)
l_c	critical fiber length (μm)
m	strain rate sensitivity exponent (unitless)
μ	coefficient of kinetic friction (unitless)
n	true plastic strain exponent (unitless)
ν	Poissons ratio (unitless)
Q	activation energy (eV)
R	gas constant (J-mol^{-1}-K^{-1})
r	fiber radius (μm)
s	creep stress exponent (unitless)
σ_r	radial stress (Pa)
σ_θ	hoop (circumferential) stress (Pa)

σ_z	axial (longitudinal) stress (Pa)
σ_{rough}	fiber surface roughness induced radial stress (Pa)
σ_m	matrix stress (Pa)
σ_f	fiber stress (Pa)
σ_c	composite stress (Pa)
$\overline{\sigma_m}$	current matrix yield stress (Pa)
t	time (seconds)
τ	shear strength (Pa)
τ_{ys}	matrix yielding shear stress (Pa)
ΔT	$T_{upper} - T_{lower}$ (K)
V_i	volume fraction; i stands for fiber (f) or matrix (m) (unitless)
x	distance (m)
W_{ad}	work of adhesion (J-m^{-2})

Abbreviations

AFM	atomic force microscopy
BDTT	brittle-to-ductile transition temperature
CTE	coefficient of thermal expansion
EDM	electrodischarge machine
EDX	energy dispersive x-ray
LVDT	linear variable differential transformer
MMC	metal matrix composites
IMC	intermetallic matrix composites
ROM	rule-of-mixtures
SEM	scanning electron microscopy
TEM	transmission electron microscopy

CHAPTER ONE

INTRODUCTION

1.1 Introductory Comments

Operational conditions for projected aerospace, energy conversion, and advanced transportation designs demand materials with high temperature structural properties substantially exceeding those of currently available superalloys. The ordered intermetallic alloys Ti-Al, Ni-Al, and Fe-Al show particular promise for producing the next significant advancement. In particular, NiAl -- by virtue of its high thermal conductivity, low density, excellent oxidation resistance and high low-to-intermediate temperature strength -- has received the most attention for applications in the temperature range of 300 K to 1473 K. Unfortunately, before NiAl can be used in high-temperature structural engineering applications, its high temperature strength, creep resistance, and low temperature fracture toughness must be significantly improved. The metallurgical processing routes being pursued for remedying these inadequacies include traditional monolithic alloying, and compositing with advanced particulate reinforcements.

1.2 Problem Statement

Though NiAl possesses many attractive properties, deficiencies in the mechanical properties include low high-temperature strength, lack of creep strength resistance, and absence of low-temperature fracture toughness (~5 $\mathrm{MPa/m^{0.5}}$). One route to eliminate (or minimize) these inadequacies is by compositing the matrix with an advanced reinforcement. The appropriate reinforcement phase must meet a stringent requirement of high temperature strength, combined with both mechanical and chemical matrix compatibility. Mechanical compatibility includes matching the reinforcement-matrix coefficients of thermal expansion (CTE) and maintaining adequate high-temperature reinforcement-matrix adhesion, while promoting low temperature fracture toughness. Interfacial chemical reactions occurring both during composite fabrication, and under long-term thermal cycling service conditions, severely limit the types of acceptable reinforcement materials. The requirement for chemical compatibility is, thus, the most restrictive prerequisite for potential reinforcements.

Maintaining high-temperature chemical compatibility suggests the use of an inert reinforcement such as Al_2O_3 fibers or whiskers. Two drawbacks of Al_2O_3 reinforcements, however, are a large CTE mismatch ($\sim 6 \times 10^{-6} K^{-1}$) with NiAl, and the lack of high-temperature adhesion due to the absence of reinforcement-matrix chemical reactivity. The CTE mismatch generates interfacial residual stresses when cooling from consolidation temperature to room temperature, causing a combination of radial, circumferential, and longitudinal stresses within the matrix. These stresses may cause interfacial debonding and matrix cracking, and effectively increase the low-temperature adhesion, further reducing the fracture toughness of the composite.

1.3 Proposed Solution

Central to the NiAl composite design problem is appropriate control of the interface properties to obtain both high-temperature interfacial adhesion and low-temperature fracture toughness, while maintaining both thermochemical and thermomechanical interfacial stabilities. This suggests that the fiber-matrix interface should have the characteristics of a ceramic matrix composite at room temperature (a weak fiber-matrix interface), but have those of a metal matrix composite at high temperatures (a relatively strong interface). One potential solution is the creation of a graded interface through the application of a suitable reinforcement coating material. For example, the coating material may act as a transient reactivity layer to improve high temperature adhesion and long term chemical stability, or may simultaneously provide a ductile interface that increases the fracture toughness of the composite. Upon processing, the coatings form a graded interphase that provides a smoother transfer of stress from fiber to matrix.

The selection of fiber-coating materials must be commensurate with acceptable alloying practices for the NiAl matrix and available thermodynamic data on the possible fiber-coating reactions must be considered. In light of these requirements, the coating materials Nb, Ti, and Ni were selected for detailed study. Niobium is attractive for several reasons. For instance, the Nb-Al_2O_3 high-temperature reaction produces a very thin (monolayer) reaction zone and has a CTE close to that of the fiber [Morozuni, 1981; Pierik, 1990]. In addition, niobium is ductile at room temperature and several investigations have been directed toward understanding the alloying behavior of Nb and NiAl [Cotton, 1993]. Titanium, on the other hand, is highly reactive with Al_2O_3, forming extended reaction zones, and producing a strong chemical bond between the fiber and matrix [Clark, 1984]. The high-temperature reaction, Ni-Al_2O_3, provides chemical bonding and fiber wetting, and readily dissolves into the matrix upon consolidation.

This study investigates the properties of niobium-, titanium-, and nickel-coated polycrystalline and single-crystal Al_2O_3 continuous fibers composited with NiAl. The three primary areas investigated are: (1) interfacial thermochemical stability, (2) thermomechanical behavior, and (3) high-temperature fiber-matrix bonding. Investigation and characterization of the interfacial thermochemical stability, including the oxidation behavior, was approached by thermally cycling model composites in laboratory air. Qualitative and quantitative fiber surface morphology studies are reported and described. The thermochemical behavior of low volume fraction composites (5-7 vol.%) is investigated using dilatometry to measure thermal strain of composites as a function of temperature (300 K - 1425 K). The instantaneous CTE and the matrix stresses may be calculated from these data, which provide qualitative information on the high temperature interfacial shear strength. The thermochemical studies also provide qualitative information on interfacial metallurgical stability. Results of process-induced fiber damage, and its relationship to the effectiveness of load transfer, are also included.

1.4 Thesis Organization

This introduction has defined the engineering problem and suggested a proposed solution. The second chapter presents a literature review beginning with a description of the thermodynamic and chemical aspects of the fiber-matrix interface. This is followed by a brief description of fiber-matrix adhesion mechanisms and an examination of fiber coating design considerations. The next section reviews the mechanical and thermomechanical behavior of NiAl and NiAl composites. Chapter Three describes the experimental details and procedures used in acquiring the various data.

The results and discussion are presented in Chapter Four, with the fiber surface morphology and composite microstructure discussed first. Composite thermal cycling, thermochemical stability and composite fracture behavior are then discussed. Finally, the thermal expansion behavior of Saphikon composites and stress analysis results are presented. Conclusions are enumerated in Chapter Five.

CHAPTER 2

REVIEW OF THE LITERATURE

2.1. Thermodynamic and Chemical Aspects of the Fiber-Matrix Interface Region

Composite technology exploits the stiffness and strength of the reinforcement phase through dispersion and control of the load transfer from the matrix to the reinforcement. The role the reinforcement-matrix interface plays in strengthening the material is, therefore, crucial to understanding the mechanical behavior of a composite [Metcalfe, 1974]. As a background to the complex physico-chemical interactions at the reinforcement-matrix interface that ultimately determine the mechanical response of the composite, the interfacial chemical thermodynamics will be discussed first.

2.1.1 Thermodynamics of Metal-Ceramic Interface Formation The formation of a metal-ceramic bond yields energy when intimate contact (distances approaching 10 nm) is established between the metal and ceramic surfaces. The simplest description of this interface formation considers the differences in the metal and ceramic surface energies. Surface energies for liquid metals generally range from 0.072 J-m^{-2} for Cs to 3.24 J-m^{-2} for Re [Murr, 1975]. Surface energies for solid metals are generally less than these values, and anisotropy effects corresponding to different crystallographic orientations must be considered. Experimental measurements of the surface energies of ceramics are less abundant, but the known values are generally lower than those for metals, and range from 0.06 J-m^{-2} for liquid B_2O_3 to 1.19 J-m^{-2} for TiC (0.905 J-m^{-2} for solid Al_2O_3) [Kingery, 1976].

The thermodynamic criterion for a liquid metal to wet a solid ceramic requires that the surface energy of the ceramic be greater than that of the metal [Howe, 1993]. Since this is generally not the case, wetting of ceramic fibers by liquid metals rarely occurs unless a chemical reaction takes place. Unfortunately, fiber-matrix reactions may compromise the fiber mechanical properties and, in most cases, should be limited. On the other hand, inadequate wetting produces fiber-matrix interfacial voids that act as stress raisers and potentially degrade the composite mechanical properties. These interrelated and opposing effects make choosing appropriate fiber reinforcements for a given matrix material difficult.

The Dupré equation puts these ideas into a thermodynamic and mathematical basis by describing the change in free energy, ΔG, during the formation of a metal-ceramic interface,

$$\Delta G = \gamma_m + \gamma_c + \gamma_{mc}, \qquad 2\text{-}1$$

where γ_m and γ_c are the surface energies of the metal and ceramic, respectively, and γ_{mc} is the metal-ceramic interfacial energy [Adamson, 1960]. For practical cases, when chemical bonding occurs at the interface, and interfacial separation produces metal or ceramic plasticity, the Dupré equation can be rewritten as

$$\gamma_m + \gamma_c - \gamma_{mc} \leq W_{ad}, \qquad 2\text{-}2$$

where W_{ad} is the work of adhesion. This equation indicates improvement in metal-ceramic bonding (adhesion) requires a decrease in the interfacial energy, γ_{mc}.

A general observation regarding γ_{mc} can be made for metal-Al_2O_3 systems [Nicholas, 1989]: in chemical bonding, the interfacial energy between various metals and Al_2O_3 increases roughly with the melting point of the metal, and appears to depend equally on the interaction of the metal with the metallic or nonmetallic element of the ceramic. Furthermore, a qualitative estimate of the wetting characteristics of ceramics by metals can be obtained by using the semi-empirical relationship, between the ionicity and the electronegativities of the component elements [Pauling, 1948]. For example, Al_2O_3 is about 63% ionic, AlN is 40%, Si_3N_4 is 30% and SiC is only 12% ionic. In general, highly ionic ceramics, such as Al_2O_3, are difficult to wet and are chemically stable since their electrons are tightly bound. Ceramics with more metallic bonding character, such as SiC, tend to have a higher surface energy and are more easily wetted, and are more chemically reactive than the ionically bonded ceramics.

Evaluation and comparison of studies correlating the interfacial strength and the chemical bonding of metal-ceramic systems are difficult because the structure and extent of reactions at the interface are often not well characterized, and different testing techniques are employed. With this proviso, several recent studies performed on well characterized interfaces in metal-Al_2O_3 systems allow some insight into bond-strength relationships [Klomp, 1987]. Table 1 gives the dependence of the interface strength, expressed in terms of a critical energy release rate G_c, on the crystallographic orientation for single and polycrystalline bcc Nb diffusion bonded to hcp Al_2O_3 under high vacuum conditions [Elssner, 1985]. The interface fracture energy is highest when the metal-ceramic interface parallels the close packed planes —(110) || (0001)— and directions —[110] || [$11\bar{2}0$]— and decreases for other orientations. The interfacial energy is lowest in close packed planes making W_{ad} higher. In the case of polycrystalline samples, the fracture energy is lower because of the high defect density, large number of slip systems, and poor atomic matching across the interface provide crack initiation sites.

The room temperature tensile strength versus the work of adhesion is compared for various metal-Al_2O_3 systems is shown in Figure 1a [Klomp, 1987]. These data indicate that the tensile strength scales with the melting point of the metal. A similar trend, displayed by the data in Figure 1b, show the tensile strength of several pure molten metals- and Ni alloy-Al_2O_3 interfaces versus the oxygen affinity of the metals or alloying

Table 1 Interface energy, Γ_c, and crystallographic relationships for Nb-Al_2O_3 joints.

	Nb Polycrystalline (g.s. ≈ 370 μm)	Nb Single Crystal (110) Plane
Sapphire (0001)	$\Gamma_c = 26\ J\ m^{-2}$	$\Gamma_c > 150\ J\ m^{-2}$ $[1\bar{1}0]_{Nb} \parallel [11\bar{2}0]_{Sapphire}$
Sapphire $(1\bar{1}00)$	$\Gamma_c = 55\ J\ m^{-2}$	$\Gamma_c = 74\ J\ m^{-2}$ $[001]_{Nb} \parallel [0001]_{Sapphire}$ $\Gamma_c = 110\ J\ m^{-2}$ $[001]_{Nb} \parallel [11\bar{2}0]_{Sapphire}$

elements [Crispin, 1976]. These data emphasize that the chemical affinity of the elements across the metal-ceramic interface may provide a useful estimate of the strength of a metal-ceramic interface.

2.2 Fiber-Matrix Bonding Mechanisms

. The composite system, combined with the consolidation process (e.g., squeeze casting, diffusion bonding), determines the type and extent of the fiber-matrix bonding; however generalities apply to all systems. Mechanical and chemical bonding are the two main categories of interfacial bonding and will be discussed below [Chawla, 1987].

2.2.1 Mechanical Bonding A purely mechanical bond implies that all chemical sources of bonding are absent. The origins of mechanical bonding can be either a

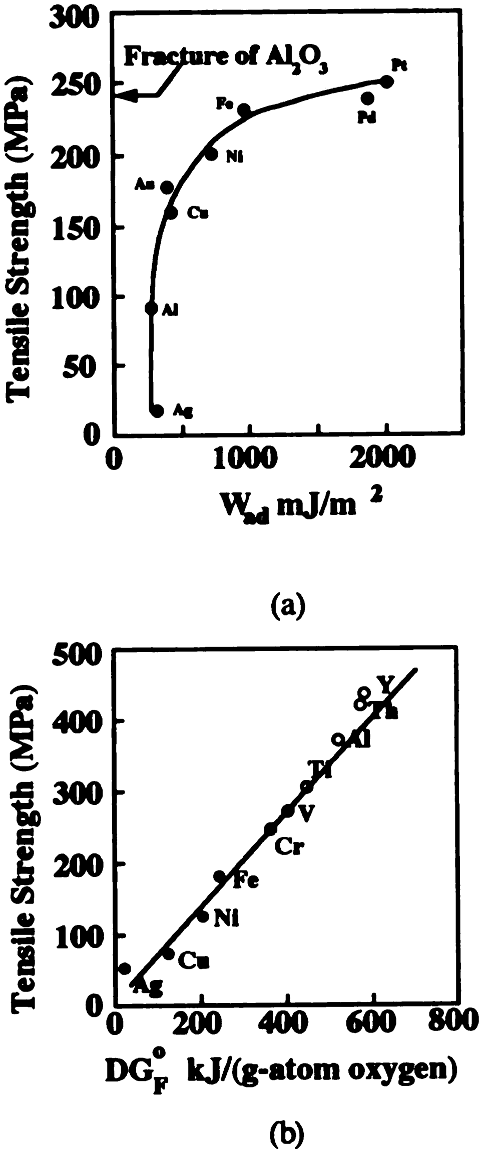

Figure 1 Strength versus (a) the work of adhesion and (b) the oxygen affinity of metal.

mechanical interlocking, resulting from irregularities on the fiber surface, or from frictional effects arising from stresses produced by differences between the coefficient of thermal expansion of the matrix and the fiber. In addition to providing a higher debond stress and increasing the strength of the composite, increasing the fiber surface roughness can increase the fracture toughness of the composite by increasing the amount of energy required for fiber pull-out [Paransarthy, 1992]. The fiber surface roughness can change by surface faceting transitions that take place during consolidation, such as occurs in the MgO-NiO system [Handwerker, 1990]. Other fiber surface roughening processes include dissolution of the fiber into the matrix [Howe, 1993]. Also, fibers may be naturally rough.

2.2.2 Chemical Bonding Chemical bonding involves transfer and interactions of electrons on an atomic scale [Howe, 1993]. Chemical bonding can be classified according to four types [Metcalfe, 1974]: (1) dissolution and wetting bond; (2) reaction bond; (3) exchange-reaction bond; and (4) oxide bond. For the case of dissolution and wetting bonds, interaction forces develop when the atoms of the constituents approach within a few atomic diameters of each other. This attraction produces wetting and dissolution. An example of this bonding condition is niobium reinforced aluminum. On the other hand, reaction bonding requires the diffusion controlled transfer of atoms from one or more of the constituents to the interface reaction site and, hence, depends on the reaction kinetics for interphase growth. The exchange-reaction bond is a special case of the reaction bond and proceeds by two sequential, distinguishable, reactions (though from a practical viewpoint the reactions may appear indistinguishable). An example of this type of reaction is a titanium-aluminum alloy reinforced with boron, which forms a boride containing both titanium and aluminum, followed by an exchange between the titanium in the matrix and the aluminum in the diboride [Klein, 1969]. Finally, in contrast to the previous types of bonding mechanisms, the oxide type bond classification occurs when an oxide reinforcement is present. Though no new principles of bonding are involved with oxide bonds, and the three former bond types are applicable, developments in the fabrication and cost of oxide reinforcements, such as single crystal and polycrystal Al_2O_3 fibers, combined with extensive industrial use, makes this classification subset sensible [Weddell, 1990].

2.2.2.1 Classifications of Metal-Ceramic Interfaces To help minimize confusion between different metal-ceramic systems, four interface classifications, based on the type of the chemical bonding and interphase formation, are summarized in Table 2 [Reddy, 1989]. Class I consists of a pure metal oxide at the interface and is represented as $AO_x|MO_y|M$, with the interface between the ceramic and the metal being a thin layer of the lowest valent metal oxide, MO_y. This type of interface is quite common and examples include oxide glass or ceramic $|NiO|Ni$ and $Al_2O_3|Cu2O + Cu$. Class II interfaces have ternary oxides at the interface. This system is represented as $AO_x|AMO_{x+y}|M$ and occurs only when a compound of the type AMO_{x+y} exists in the ternary system A-M-O. Typical examples of these interfaces are $ZrO_2|NiZrO_3|Ni$, $Al_2O_3|CuAlO_2|Cu$, and $Al_2O_3|NiAl_2O_4|Ni$.

Class III represents the formation of a solid solution in the ceramic near the interface. This system is represented as $AO_x|AO_x - MO_y|M$. In this case no new phase is formed, but a concentration gradient of MO_y in the ceramic exists near the interface. An example of this class is the formation of MgO-NiO solid solution at the interface. Finally, Class IV represents the formation of a solid solution in the metal, and is represented as $AO_x|M(A,O)$. Certain reactive metals react with oxide ceramics, resulting in metallic solid solution without forming a new phase at the interface. An example of this class is Al_2O_3-Nb, where Nb has a high solubility for both Al and O_2 and the dissolved components have low thermodynamic activity.

Table 2 Metal-ceramic interface classification scheme (adopted from Reddy, 1989).

Class	Symbol	Interface	Example
I	$AO_x|Mo_y|M$	Metal Oxide	$Al_2O_3|NiO|Ni$
II	$AO_x|AMO_{x+y}|M$	Ternary Oxide	$Al_2O_3|NiAl_2O_4|Ni$
III	$AO_x|AO_x\text{-}MO_y|M$	Solid-solution in ceramic	$MgO|NiO|Ni$
IV	$AO_x|M(A,O)$	Solid-solution in metal	Al_2O_3-Nb

2.3 Fiber-Coating-Matrix Design Considerations in NiAl IMCs and MMCs

In addition to the thermodynamic issues previously addressed, a number of other factors must be considered when choosing an appropriate fiber coating material for a NiAl-Al_2O_3 composite. Among these factors are the metallurgical and mechanical properties of NiAl, and those of the fiber coating. In this section, a review of the main issues regarding tailoring the interfacial properties of NiAl-Al_2O_3 composites is given. First a survey of relevant properties of NiAl and Al_2O_3 are presented, followed by chemical compatibility and metallurgical stability requirements for NiAl-(coated-Al_2O_3) composites. Finally, some theoretical and experimental examples of coated fiber composites systems are given.

2.3.1 Review of the Mechanical and Physicochemical Properties of NiAl The physical and mechanical properties of NiAl have been published in two review articles by Miracle and Noebe[Miracle, 1993; Noebe, 1993]. In addition to these reviews, three papers detailing the potential uses of NiAl in the aerospace industry have recently been reported [Darolia, 1993; Walston, 1993; Darolia, 1991]. These cited works provide an excellent summary of the current metallurgical understanding of both single crystal and polycrystal NiAl.

2.3.1.1 Crystal Structure and Thermophysical Properties of NiAl NiAl is a Hume-Rothery β-phase electron compound with a valence electron/atom ratio of 3/2, that crystallizes in the primitive cubic B2 structure (space group Pm3m, CsCl prototype) as shown in Figure 2. Stoichiometric Ni-50 at.% Al melts congruently at 1911 K and, as Figure 3 indicates, has a wide phase field consisting of a B2-ordered intermetallic over the composition range of 65 -76 wt.% (45 to almost 60 at.%) Ni [Okamoto, 1993]. The room temperature lattice constant of stoichiometric Ni-50Al is 0.2887 nm and the lattice parameter of NiAl on either side of stoichiometry can be described by a linear relationship of the form,

$$a_o(\text{nm}) = 0.299839 - 0.000222 * (x), \text{ for } x = 50 - 60 \text{ at.\%Ni or}$$

$$a_o(\text{nm}) = 0.266819 - 0.000438 * (x), \text{ for } x = 45 - 50 \text{ at.\%Ni} \qquad 2\text{-}4$$

[Noebe, 1993]. Using x-ray measurements, Cooper concluded that no ionic bonding occurs in NiAl, but that d-band filling by Al-to-Ni charge transfer occurs and results in a mixture of covalent and metallic bonds [Cooper, 1963].

Another thermophysical property closely related to the bonding structure of the material is the coefficient of thermal expansion. The atomistic cause of thermal expansion is explained by the changing curvature of the interatomic potential energy function. In general, strongly bonded solids expand at lower rates than weakly bonded solids [Speyer, 1994] and the coefficient of thermal expansion decreases as the melting point of the material increases. The thermal expansion behavior of polycrystalline NiAl has been studied by a number of investigators and is found to be a strong function of temperature, but not of composition [Clark, 1984]. The thermal expansion coefficient for NiAl is about 30% less than that for pure Ni, but is very similar to that of Ni-base superalloys [Darolia, 1991] and can be described by

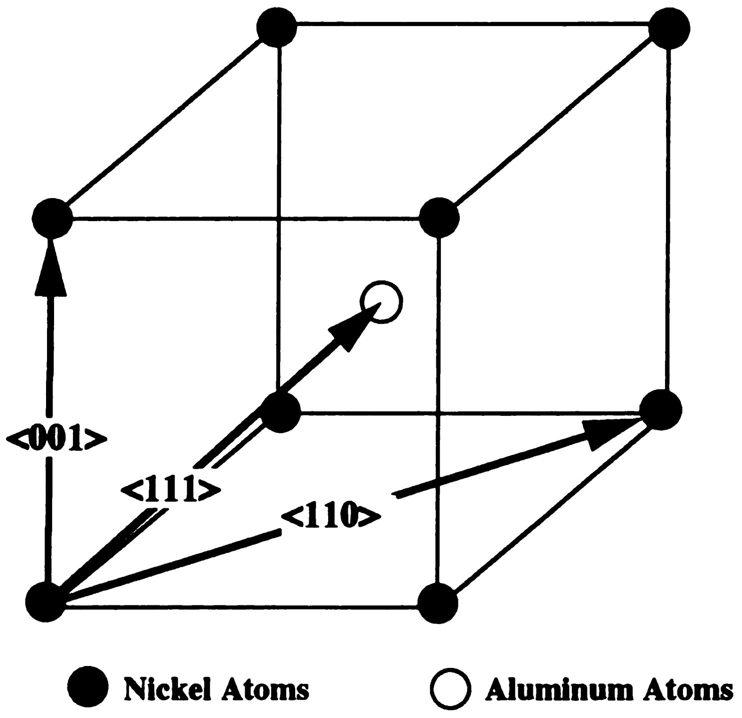

Figure 2 The crystal structure (primitive cubic CsCl (B2)) of NiAl.

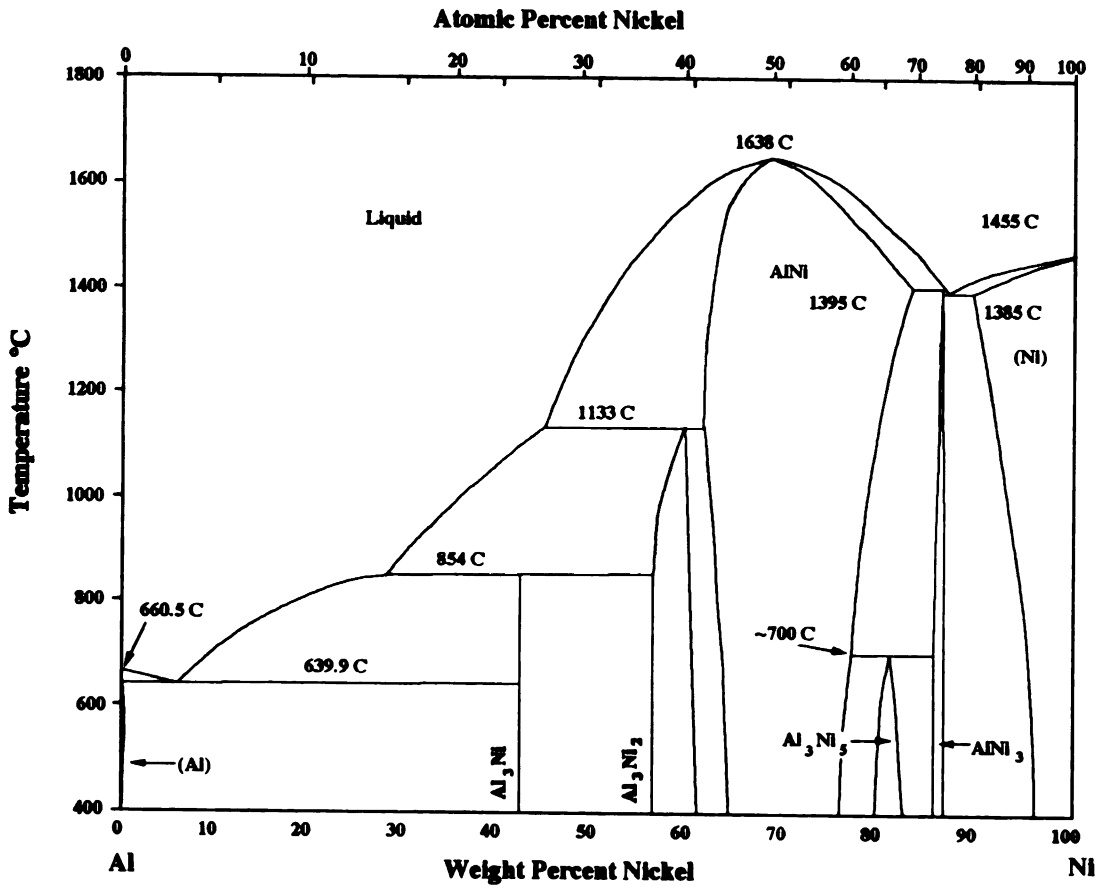

Figure 3 The Ni-Al equilibrium phase diagram.

$$\alpha(K^{-1}) = 1.1602x10^{-5} + 4.085331x10^{-9}T - 1.58368x10^{-12}T^{2}$$
$$+4.18374x10^{-16}T^{3} \qquad 2\text{-}5$$

in the temperature range of 300 K to 1500 K [Clark, 1984].

2.3.1.2 Mechanical Properties of NiAl The mechanical properties of NiAl have been investigated in numerous ways with, an unusual variety in results reported by different investigators. This lack of agreement may be attributed to differences in grain size, interstitial contents, texture, and chemistry of the material being tested. Only the major mechanical properties will be summarized here. Further details may be found in the reports by Noebe, et al. and Miracle [Noebe, 1993; Miracle, 1993].

The Young's modulus of NiAl was found to be sensitive to processing technique, because of induced <111> texture, but not to composition [Khadjikar, 1990; Rusovic, 1979]. The reported modulus for extruded NiAl powder can be described by the following equation [Hellman, 1990],

$$E(GN - m^{-2}) = 249.3 - 0.072T + 3x10^{-5}T^{2}. \qquad 2\text{-}6$$

Other temperature dependent mechanical properties include the shear modulus, G, and the Poisson's ratio which are described by

$$G(GN - m^{-2}) = 76.6 - 0.017T \text{ and}$$

2-7

$$\nu = 0.307 + 2.15x10^{-5}T, \qquad 2\text{-}8$$

respectively [Hellman, 1990].

The flow properties of NiAl are highly sensitive to variables such as composition, strain rate, grain size, cooling rate, and specimen fabrication. Like bcc metals, the flow stress of NiAl, shown in Figure 4 for a number of compositions, exhibits a strong temperature dependence at low absolute temperatures, attributable to a large Peierls stress [Pascoe, 1968]. Though the yield stress is sensitive to metallurgical processing properties, all studies agree that increasing the testing temperature decreases the yield

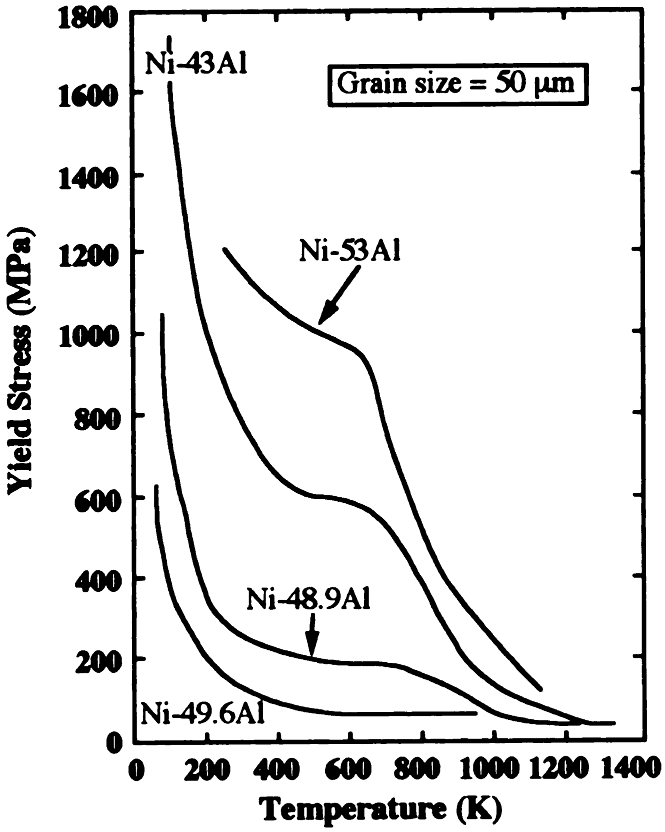

Figure 4 The flow stress of NiAl for a number of compositions.

stress and, that for stoichiometric compositions, the yield stress is independent of grain size [Nagpal, 1990]. The insensitivity of the yield stress to the grain size is apparently due to the lack of dislocation pile-ups providing grain boundary strengthening and is more sensitive to the lattice resistance to dislocation motion [Baker, 1991].

At low temperatures, NiAl deforms predominantly by <100>{011} slip (and occasionally by slip on {001}) Consequently, only three independent slip systems are available for deformation [Groves and Kelly, 1963]. Since no cross-slip is known to occur, two additional independent slip systems are required to satisfy von Mises criterion for extensive, uniform crack free deformation of a NiAl polycrystal. This lack of an adequate number of slip systems is the principle origin of the low temperature brittleness. At elevated temperatures, dislocation climb and glide mechanisms are activated and cause increases in both the ductility and the fracture stress of NiAl. [Bowman, 1992]. This behavior is illustrated by the brittle-to-ductile transition temperature (BDTT) occurring in the range of 550-700 K [Noebe, 1993].

The high-temperature creep behavior of NiAl follows that for metals and alloys in which the second stage, or steady state creep being expressed by the Dorn formulation [Meyers and Chawla, 1984]. A summary of the stress exponents and activation energies determined by various investigators for creep of NiAl is presented in Table 3.

The results of these investigations indicate that, with a stress exponent ~ 5 - 7, the high temperature creep in NiAl is climb controlled. Strategies for improving the creep resistance of NiAl include solid solution strengthening [Rudy, 1986], precipitation strengthening [Polvani, 1976], dispersion strengthening [Whittenberger, 1990], and composite reinforcement [Bowman, 1992]. Though improving creep resistance is vital for producing the necessary mechanical response of the material, generally these improvements must be balanced with a decline in other properties, such as strength or oxidation resistance.

2.3.1.3 Ternary Alloying Effects in NiAl As mentioned above, studies of alloying NiAl with a ternary element have been performed in an effort to understand the effects of enhancing the strength or creep resistance by second phase precipitation, solid solution hardening or grain refinement. When choosing a fiber coating material, the alloying behavior between the fiber coating and NiAl matrix must be considered. Cotton et al. [1993] have shown that the alloying behavior of NiAl appears to correlate with group number in the periodic table. Figure 5 illustrates an NiAl alloying behavior classification scheme of the periodic table: Type-A (Groups IIIB, IVB, and VB), where the solubility of the third element is usually low and at least one ternary intermetallic phase occurs; Type-B (Group VIB), in which the third phase forms a pseudobinary eutectic with NiAl; and Type C (Groups VIIB,and VIIIB), in which the third element exhibits a large solubility and may form an isostructural B2 intermetallic. Both Ti and Nb fall into the Type-A category, and commonly form either a Heusler or Laves, phase

Table 3 Summary of creep parameters for NiAl.

Al (at.%)	Grain Size (μm)	Temp. (K)	n	Q (kJ-mol^{-1})	Ref.
48.25	5 - 9	1000 - 1400	6.0 - 7.5	313	Whittenberger, 1988
44 - 50.6	15 - 20	1100 - 1400	5.75	314	Whittenberger, 1987
50	12	1200 - 1300	6	350	Whittenberger, 1990
50	450	1073 - 1318	10.2 - 4.6	283	Yang, 1973
50	500	1173	4.7	—	Rudy, 1986
50.4	1000	1075 - 1750	7.0 - 3.3	230 - 290	Vandervoort, 1966

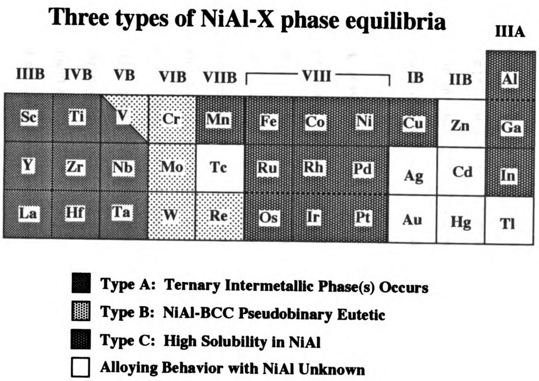

Figure 5 Correlation between the periodic table and the alloying behavior of NiAl.

with a solute preference for the Al site [Polvani, 1976; Stoloff, 1984]. The solubility of Type-A elements is usually limited at ambient temperatures, and precipitation is expected for alloying levels above about one percent. Nickel belongs to Type-C, where the ternary additions show a large solubility in NiAl and, generally, form B2 compounds.

2.3.2 Oxidation and Thermochemical Behavior of Monolithic NiAl and NiAl Composites Two essential properties required of high-temperature composite materials are resistance to cyclic oxidation, and good interfacial metallurgical stability. Gains in improving composite properties, such as stiffness and strength, will be of limited value if oxidation becomes the limiting factor in determining the upper use temperature. NiAl has excellent cyclic oxidation resistance, due to the easy formation of strictly Al_2O_3 protective oxide layers occurring after a brief transient stage of metastable Al_2O_3 phase formation [Doychak, 1989; Pettit, 1967].

2.3.2.1 Fiber-Matrix Chemical Compatibility in NiAl Composites The fiber-matrix chemical reactions that continuously occur during thermal cycling of composite systems present major concerns for long-term stability. Thermodynamic analyses of fiber-matrix combinations help screen different reinforcement materials for their chemical compatibility with a given matrix. A reinforcement material-matrix combination can be considered to be chemically incompatible for either of the following reasons: (1) the reinforcement material is reduced by an element of the intermetallic matrix, thus releasing an element of the reinforcement material or, (2) two-product compounds form at unit activity [Misra, 1989]. If neither process occurs, then either the product compounds are formed at reduced activities, or the elements of the reinforcement material are dissolved in the matrix. In such cases, the magnitudes of the equilibrium activities of the reaction products, at a specified temperature, determine whether a reinforcement is compatible with the matrix. For screening purposes, an activity value of 0.001 was chosen by Misra, and the ceramic reinforcements in Table 4 were determined to be chemically compatible with NiAl at the expected use temperature between 1273 and 1573 K.

Recently, Misra, et al. have discussed the requirements of the ideal fiber-matrix interface in NiAl-Al_2O_3 composites [Misra, 1992][1]. They concluded that a strong chemical fiber-matrix bond is required to increase interface shear strength and to withstand radial stresses experienced during heating. In addition, the ideal coating would be ductile at room temperature and would be thick enough to effectively reduce the interfacial stresses and confer some ductility to the interface.

Table 4 Reinforcement-NiAl chemical compatibility table.

Carbides	Borides	Borides	Oxides	Nitrides
HfC	*CrB_2	*TaB_2	Al_2O_3	AlN
TiC	HfB_2	TiB_2	BeO	HfN
NbC	*LaB_6	TiB	Y_2O_3	*TiN
TaC	*NbB_2	ZrB_2	HfO_2	ZrN
ZrC	ScB_2		La_2O_3	

* Borderline situations

Pierik, et al. also reported on NiAl-fiber interfacial compatibilities by studying different types of ceramic reinforcements, including Sumitomo and Nextel-480 Al_2O_3 fibers [Pierik, 1990]. Since the compositions of Nextel 480 and Sumitomo fibers consist of Al_2O_3 grains with ~15 wt.% of SiO_2 located at the grain boundaries the glassy phase boundary reacts with the NiAl matrix during consolidation. The reaction products include mullite ($Al_6Si_2O_{13}$) and isolated grains of Ni, Si, and Al at the fiber-matrix

---

[1] Borderline situations

interface. No mechanical property information was reported, so the effects of the reaction products on the bond strength cannot be assessed. These results, however, do suggest that alumina fibers with a significant amount of second phase are not likely to be considered candidate reinforcements.

2.3.2.2 Oxidation Behavior of NiAl and NiAl Composites Among the various environmental effects, thermal cycling to temperatures greater than 0.5 T_m in corrosive atmospheres provides one of the most severe tests to determine if a composite system is potentially useful. Studies of monolithic NiAl oxidation have characterized scale-growth mechanisms and kinetics, scale microstructures and morphologies, and oxide-substrate adherence [Doychak, 1989]. These studies indicate that the oxidation mechanisms in NiAl are different from those of other alumina formers because of the strong tendency to form strictly Al_2O_3 at high temperatures. In addition, a transient stage of oxidation at intermediate temperatures results in the formation of metastable Al_2O_3 phases such as θ-Al_2O_3 and γ-Al_2O_3 [Doychak and Rhule, 1989].

Only a few studies of the oxidation behavior of NiAl composites have been performed. So as a starting point, considerations of reinforcement-induced changes in the oxidation resistance of other composite systems will be presented. In most cases, the reinforcement increases the oxidation rate of the composite by providing a fast diffusion path along the interface, or by disrupting the formation of a protective interfacial scale. Surface-related interfacial problems are more severe for continuous fiber composites when the interface emerges at a free surface, and thus acts as a long-range path for transport of oxygen into the matrix interior. As an example, titanium alloys reinforced with SiC monofilaments suffer progressive interfacial oxidation after prolonged periods at relatively modest temperatures (573 - 873 K) [Hartley, 1988]. These temperatures are too low to cause internal fiber-matrix attack, but oxygen egress from the free surface is rapid and causes degradation of the interfacial structure, and hence of the composite mechanical properties.

In contrast to the oxidation induced degradation behavior, some research groups report either no decrease in oxidation resistance, or an increase in oxidation resistance. For example, Wei studied the isothermal oxidation behavior of Al-SiC monofilament composites up to 673 K and found no change in the oxidation behavior due to the presence of the fiber [Wei, 1990]. These results were explained on the basis of a high degree of fiber-matrix adhesion, combined with a large amount of matrix plasticity which blocked a fast diffusion path along the interface. An improvement in composite oxidation resistance is illustrated by Stott and Ashby, who report an increase in the oxidation resistance for 3 μm SiC particles in a Ni matrix (with a volume fraction > 10%, and exposure to pure oxygen at 1373 K) [Stott and Ashby, 1978]. The SiC particles apparently impede the transport of Ni^{2+} ions through the growing NiO layer, producing an increase the composite oxidation resistance.

Doychak, et al. reported on the isothermal and cyclic oxidation behavior of aligned, continuous fiber, NiAl-Saphikon and NiAl-(Ni-Saphikon) composites [Doychak, 1992]. Extensive interfacial scale formation for both the composite and the bulk materials were seen in the isothermal experiments. The thermal cycling experiments revealed oxide growth rate constants for the composited materials consistent with alumina formers . Composites reinforced with fibers coated with ~1 μm nickel had rate constants 2-10 times higher than the uncoated fibers. This increased rate constant was attributed to Kirkendall interfacial porosity and suggests that the oxidation behavior of coated fiber composites may be substantially different than uncoated fiber composites.

2.3.2.3 The Effects of Thermal Cycling on the Mechanical Properties of Composites The CTE mismatch, $\Delta\alpha$, for IMCs and MMCs range from $4 \times 10^{-6}\,K^{-1}$ (W/Ti system) to $24.6 \times 10^{-6}\,K^{-1}$ (C/Al system). This mismatch produces a thermal strain of 10^{-3} or greater, which is on the order of most matrix yield strains, and may thus damage the composite through nucleation and growth of interfacial micro-damage. Thermal cycling damage has been reported in several metal matrix composite systems:

tungsten fiber/copper [Yoda, 78; Yoda, 79], Al_2O_3 fiber (FP)/magnesium [Bhatt, 1983], and SiC/titanium [Park, 1983]. The thermal cycling damage reported in these investigations include microvoids or cracks at the interfaces, which leads to interface debonding. This micro-damage results in degradation of mechanical properties, as shown by the results of Grimes et al. [1977] where the ultimate tensile strength of continuous boron fiber/6061 Al composites, that were cycled between room temperature and 693 K for various numbers of cycles, was reduced by ~15%.

Micro-damage, which has been observed in several continuous fiber MMC systems [Write, 1975], often results in permanent dimensional changes. Although the majority of investigations report that the major dimensional changes occur along the fiber axis, Kyono, et al. [1986] observed dimensional changes in a continuous graphite fiber/5056 Al composite in the transverse direction. This transverse dimensional change appears to have been caused by complete debonding of the matrix-fiber interfaces during the early stages of cycling, followed by transverse swelling.

2.3.3 Coating Fibers to Fabricate Engineered Interfaces Several deposition techniques are available to coat long fibers and, to a lesser extent, to coat short fibers and particulate reinforcements. These techniques may be divided into chemical vapor deposition (CVD) [Alam, 1990] and physical vapor deposition (PVD), which includes electron beam evaporation, ion beam sputtering, and magnetron sputtering [Everett, 1991; Cai, 199?]. Other procedures that are used to coat fibers include spraying and plating techniques [Everett, 1991].

Among the possible roles of the fiber coating, the encouragement of wetting and the production of a reaction barrier are the most common. Promotion of wetting is usually brought about through the stimulation or modification of some local reaction [Delannay, 1988]. Various other fiber-coating wetting agents have been explored, particularly for carbon fibers in aluminum and magnesium [Amateau, 1976; Katman, 1987].

From a thermodynamic point of view, highly stable compounds emerge as strong contenders for barrier coating materials. In practice, most barrier coatings only slow down the interfacial reactions, rather than providing thermodynamically stable interfaces [Pierson, 1978]. In addition to thermodynamic stability, or at least reduced reaction kinetics, the barrier must impair transport of reactants through the coating [Kieschke, 1991]. Some coatings are designed to protect the fiber surface from damage (or oxidation) prior to incorporation into the matrix. An example of this is the application of a 50 nm SiC layer on C fibers to protect them from oxidation [Vincent, 1989].

2.3.3.1 Theoretical Studies of the Effects of Fiber Coatings on the Mechanical Behavior of Composites Theoretical analysis of the effects of fiber coatings on the axial tensile stresses and strengths of MMCs has been investigated by Xia et al. [Xia, 1993]. The analytical investigation by Xia et al. focused on composites composed of aligned fibers in which the central core of the coated fiber was surrounded by a reaction zone, and the matrix layer was exposed to a longitudinal applied stress. Two conditions were analyzed: low interfacial bond strength, and high interfacial bond strength. For low interface strengths, with debonding occurring before matrix yielding, the composite yield stress increased with increasing debonding strength. If matrix yielding took place before debonding (high interfacial strength), the composite yielding stress became constant until debonding. Furthermore, with increasing reaction zone thickness, debonding and yielding occur at a lower stress level regardless of the interfacial strength. These results indicate that interfacial debonding relaxes the stress concentration in fibers, and matrix yielding increases the stress concentration.

Theocaris and Demakos also investigated the effects of fiber coating thickness and modulus (assumed to be proportional to the yield stress) on the room temperature elastic properties of composites [Theocaris, 1992]. The types of fiber coating systems considered include coatings, not exceeding 20% of the fiber radius, with a modulus greater or less than the matrix. In the case of a coating stiffer than the matrix, the composite longitudinal modulus was greater than the transverse modulus. For a coating less stiff than the matrix, a fall in composite longitudinal modulus was seen as coating thickness increased. Although the moduli of the uncoated fiber composites are slightly higher than those of the matrix, the composite moduli always vary between the respective moduli for the matrix and the less stiffer coating.

Other researchers have used finite element analysis to study the role of the mechanical properties of the coating material in reducing the thermal residual stresses, by applying a compensating, or compliant, coating to the fiber [Arnold, 1990 and 1992; Morel and Saravanos, 1990]. This approach suggests that the two most important fiber coating parameters for reducing the matrix and in-plane stresses are the coating-matrix CTE mismatch, and the thickness of the coating. Of particular interest is the reduction of the tensile hoop stresses, which are believed to be responsible for generating radial matrix cracks. The calculated results, presented in Figures 6 to 8, indicate that the compliant layer indeed reduces the radial and circumferential stresses within the fiber and the matrix, but increases the longitudinal stresses. In addition, the mechanical properties of the compliant layer, such as yield stress, strain hardening slope, and stiffness, dominate the reduction of the interfacial stress state and have little, if any, effect on the fiber or matrix stress state.

An analytical study on the reduction of thermal stresses in MMC by Jansson and Leckie [1992] produced results similar to that of Arnold et al. [Arnold, 1992]. In the study by Jansson and Leckie, the CTE of the interface layer was determined to be the most important parameter for reducing the matrix stresses. If the CTE of the interlayer material is significantly higher (greater than 2 times) than either the matrix or fiber (compensating layer), substantial reductions in the matrix stresses may be realized. For most interlayer materials, the longitudinal matrix stress is the least affected, while the radial stress is the most affected. Reduction of the hoop stress, close to the fiber can be reduced substantially, suggesting that coatings may be successful in preventing cracking in composites.

The theoretical studies mentioned above are all limited to room temperature analysis. In addition to the temperature dependence shortcoming, a number of issues still remain to be incorporated into the formalism, particularly the effects of fiber-fiber interaction, spacing and volume fraction.

Warwick and Clyne have presented an analytical model predicting the principal stresses in coated fiber composites undergoing thermomechanical loading [Warwick and Clyne, 1991]. A general trend of large residual stresses (300-500 MPa) generated at the fiber-matrix interface leads to interfacial matrix plasticity both during heating and cooling cycles. Metcalfe established a theoretical framework for understanding the effect of the reaction layer thickness, and properties on the fracture behavior of Ti-B filament composites [Metcalfe, 1974]. In this system, a fiber-matrix interfacial reaction results in the growth of a TiB_2 layer. The mechanical properties of the composites were analyzed by assuming that the flaw size for crack initiation is proportional to the reaction layer thickness and that cracks do not initiate in the matrix. When the reaction layer is $< 1 \mu m$ thick, the size and quantity of reaction-layer flaws is less than the existing population in the fiber and, consequently, fracture is controlled by the fiber. As the reaction layer thickens, a critical point is reached where the stress intensity associated with the reaction-zone crack exceeds that in the fiber and results in failure within the reaction zone.

2.3.3.2 Experimental Investigations of Fiber-Coated NiAl Composites Only a few studies have investigated the effects of fiber coatings on the mechanical properties of NiAl-Al_2O_3 composites. As an example, Misra et al. studied the properties of a NiAl-(molybdenum-Saphikon) composite and found that, though the coating did not degrade the fiber tensile strength, the coating did not protect the fiber from damage during consolidation [Misra, 1993]. Furthermore, room temperature tensile tests revealed debonding at the fiber-molybdenum interface, indicating that the Mo-NiAl bond is

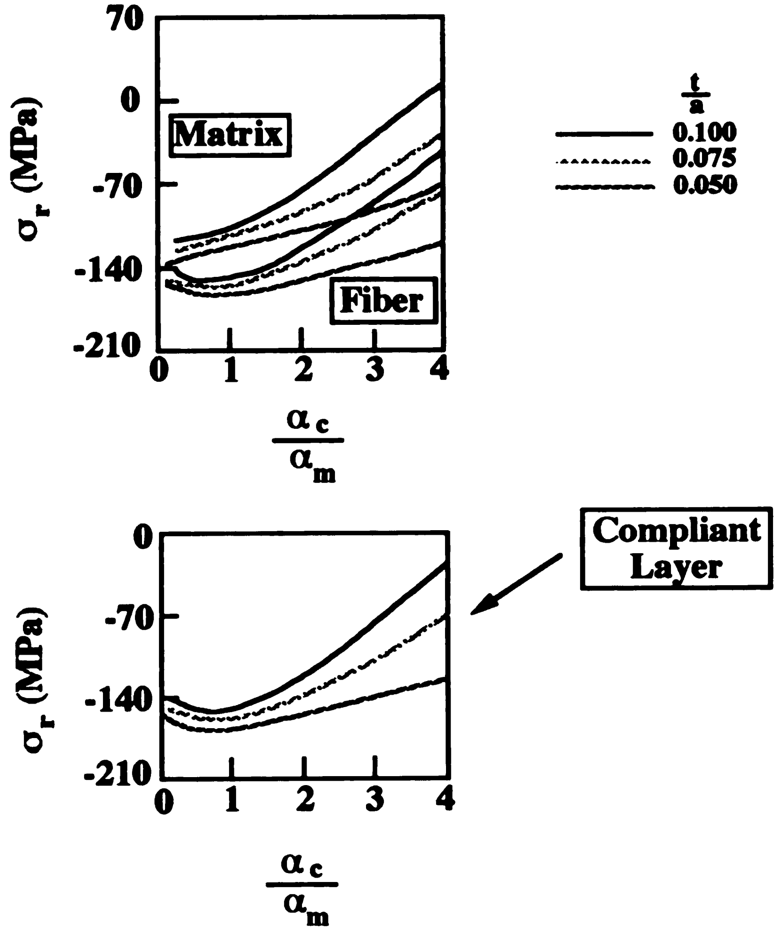

Figure 6 Radial stress versus CTE and compliant layer thickness.

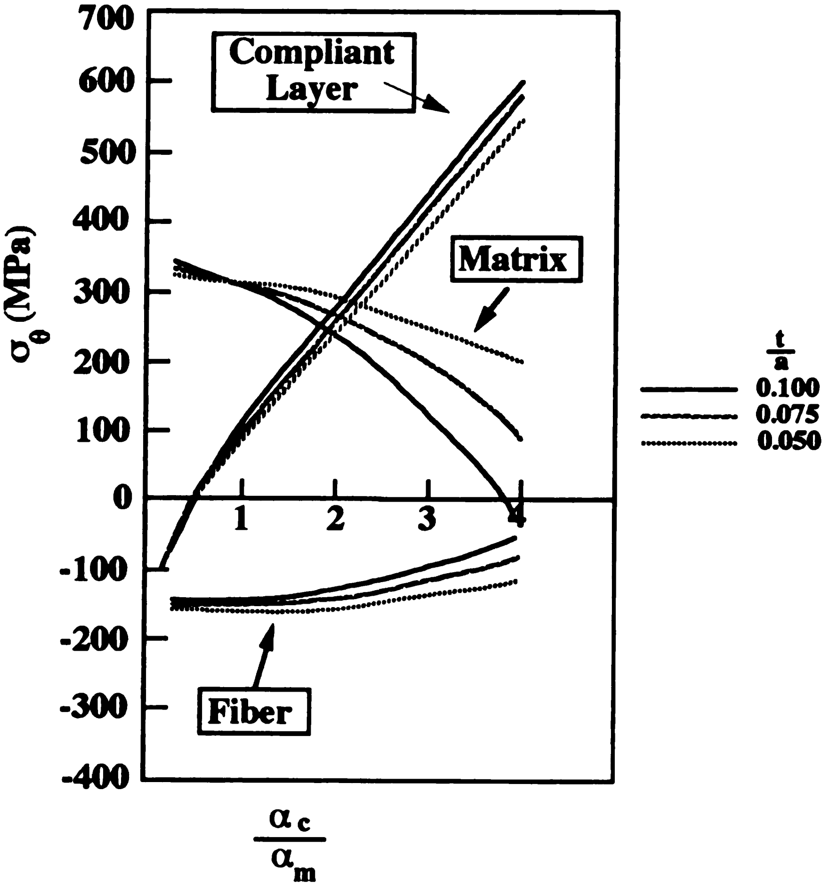

Figure 7 Circumferential stress versus the CTE and compliant layer thickness.

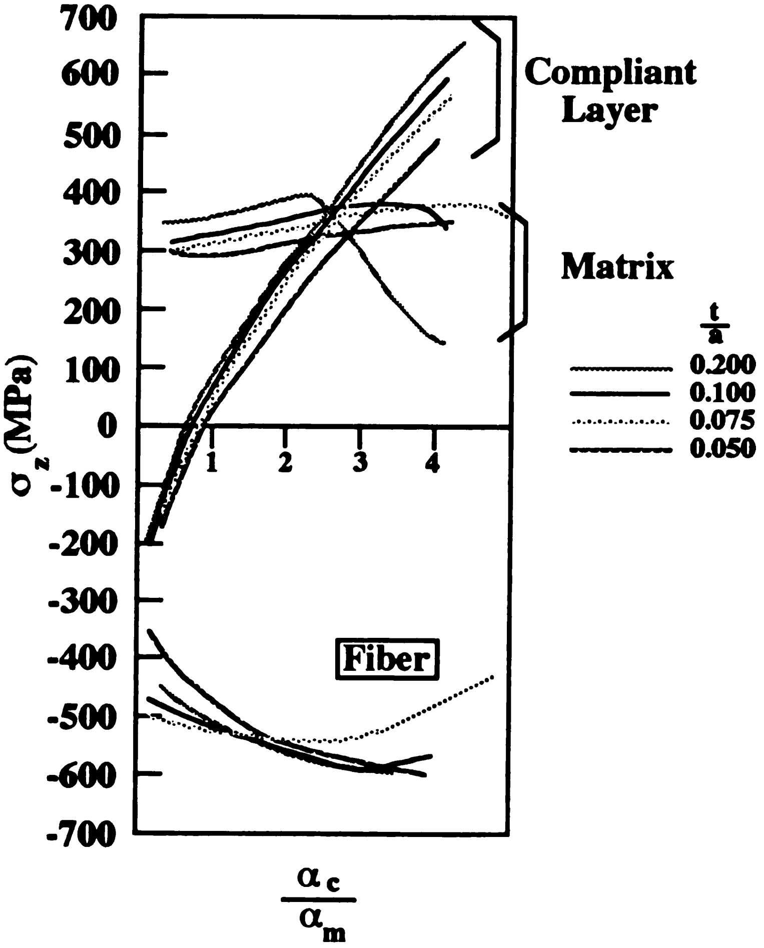

Figure 8 Longitudinal stress versus the CTE and the thickness of a compliant layer.

stronger than the Mo-Al_2O_3 bond. Additional evidence of low Mo-Al_2O_3 bond strength was obtained when high-temperature tensile tests revealed composite modulus and tensile strength that were less than bulk NiAl material. These results indicate that no fiber-matrix load transfer occurs. In contrast to these results, Bowman and Noebe reported preliminary fiber push-out results on nickel-coated Al_2O_3 fibers composited with NiAl and indicated an increase in the interfacial shear strength [Bowman, 1990]. They attribute this increase to the nickel coating reacting with the Al_2O_3 fiber and forming a chemical bond.

2.4 Mechanical and Thermomechanical Behavior of NiAl and NiAl Composites

Significant efforts, reviewed by Amato and Yang, have centered on enhancing the mechanical properties of NiAl through grain refinement, macro- and micro-alloying, and incorporating a second phase [Amato, 1994]. The purpose of the following section is to summarize some of the studies investigating the mechanical and thermomechanical properties of NiAl-based composites. In addition to these discussions, the thermal expansion behavior and residual stresses in IMCs and MMCs will be addressed.

2.4.1 Mechanical Properties of NiAl-Al_2O_3 Composites The mechanical behavior of a composite can be classified according to either bulk or interfacial properties. An evaluation of the interfacial shear strength, as measured by a fiber pushout test, of continuous fiber reinforced NiAl-Saphikon composites by Noebe et al. found that the NiAl-Al_2O_3 debond shear strength varied between 25-100 MPa, and that the bond strength was purely frictional [Noebe, 1990]. Although improvement in the low-temperature fracture toughness was achieved, little or no increase in the high-temperature tensile strength was observed. Subsequent investigations indicated an interfacial shear strength of 87 MPa at room temperature [Moose, 1990] and that organic binders applied to the NiAl powder prior to processing the composites resulted in a weak bond, 50-100 MPa, compared to the bond strength of virgin NiAl powder, which was 280 MPa [Bowman, 1992]. Bowman also found that low-temperature fracture toughness was improved by compositing, but that high-temperature toughness was nil, due to the brittleness and lack of interfacial bonding of the Saphikon fibers. Thermal cycling experiments showed that a weak interfacial bond resulted in reduced oxidation resistance [Bowman, 1992] and suggested that fiber coating(s) may be necessary to provide adequate oxidation resistance.

Bowman et al. report that the mechanical properties of monolithic NiAl are inferior to 25 vol.% NiAl-Al_2O_3 composites at high temperatures [Bowman, 1995]. Typical tensile curves acquired at 300 K and 1200 K are shown in Figure 9, with the corresponding measured properties tabulated in Table 5. These results indicate that the high-temperature behavior of the composites are inferior to the high-temperature behavior of the monolithic NiAl. Furthermore, both the composite strength (flow and fracture) and failure strain were less than that of the monolithic material. A combination of poor fiber-matrix bonding, and degradation of fiber properties, appears to be responsible for the lack of mechanical property improvement at high temperatures.

Table 5 Property summary of NiAl and NiAl-Al_2O_3 composites [Bowman, 1995].

Temp (K)	NiAl			NiAl-Al_2O_3			
	E (GPa)	σ_y (MPa)	ε_f (%)	E_I (GPa)	E_{II} (GPa)	σ_y (MPa)	ε_f
300	241	120	0.4	262	170	73.6	0.17
1200	227	70	> 20	276	—	105	—

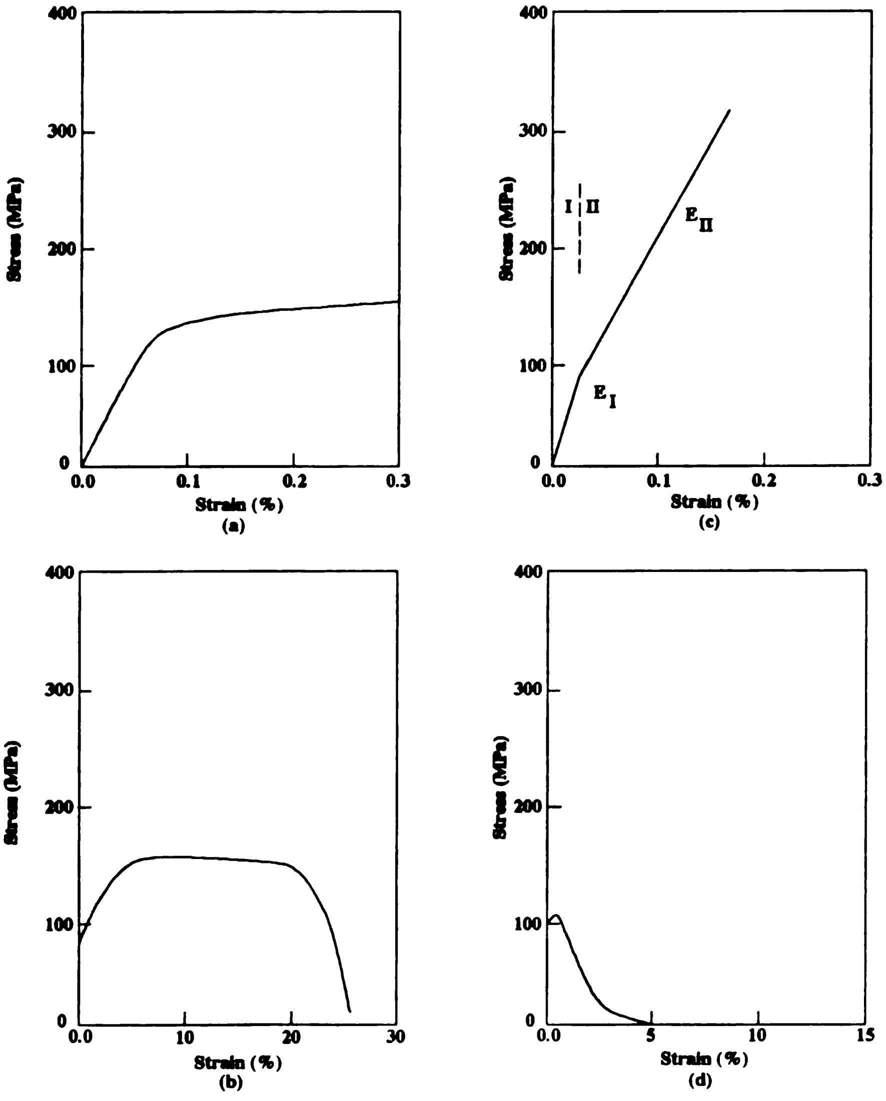

Figure 9 Tensile response for NiAl (a, b) and NiAl-Al_2O_3 composite (c, d).

N

investig

pressed

a substa

1473 K.

may be

implyin

realizat

expansi

on the

adhesio

solidifi

micron

numeri

Tyson

depend

These

cumula

mechan

reinforc

physioc

describi

interface

---

[1] The term
system of n

NiAl composited with 10 μm diameter Al_2O_3 (FP) fibers has been less thoroughly investigated: Anton and Shah focused on the mechanical properties of hot isostatically pressed NiAl-FP composites [Anton, 1992]. The bend tests obtained in this study showed a substantial increase in tensile strength at room temperature, but only a slight increase at 1473 K. Together, these studies indicate that, though acceptable mechanical behavior may be achieved in one area, deficiencies in the total composite behavior may exist, implying that the fiber-matrix interface must be properly tailored to achieve full realization of the required mechanical properties.

2.4.2 Thermal Expansion Behavior of IMCs and MMCs The thermal expansion behavior of IMCs and MMCs can provide a substantial amount of information on the temperature dependence of the composite stresses and the level of fiber-matrix adhesion. A three-part study on the thermal expansion behavior of directionally solidified eutectics and monolithic 6061 Al provides a basis for understanding the micromechanics associated with expanding composites [Garmong, 1974]. (Note that the numerical results initially reported were incorrect and were, subsequently, corrected by Tyson [Tyson, 1975].) The study by Garmong identified and modeled the temperature dependent behavior of several effects typically observed in composite thermal expansion. These effects include heating and cooling hysteresis, plastic shakedown[1], and a cumulative net strain. Furthermore, when the composites were thermally cycled, the mechanical properties tended to degrade through four basic types of damage: reinforcement failure, specimen shape instability, matrix plastic deformation, and physiochemical instability.

Another one-dimensional model, presented by Yoda et al., includes an expression describing the fiber-matrix interface, which is presumed to consist of a fiber, a thin interface region and matrix [Yoda, 1978]. The model limits the fiber to purely elastic

---

[1] The term shakedown is used in the analysis of plastically deforming structures to indicate approach to a system of residual stresses sufficient to inhibit further plastic flow.

deformation; allows the matrix to deform as an elastic/plastic body; and the allows the interface to slide by Newtonian viscous flow. Comparison of the model predictions to experimental results for a continuous W/Cu composite confirmed the predicted dependence change in plastic strain on the fiber length, fiber diameter, and the volume fraction. Wakashima and co-workers, on the other hand, assume an elastic perfectly plastic matrix, with interfacial sliding, and predict that the net strain per cycle as the fiber volume fraction increases, in agreement with data for the W/Cu system [Wakashima, 1974].

As an example of a typical thermal expansion study, Warwick and Clyne investigated the thermal fatigue of Mg-11wt%Li/20vol%SiC whisker composites. During thermal cycling, a progressive increase in composite length (strain ratchetting[2]) occurred [Warwick, 1990]. Though an exact explanation of this behavior remains to be made, the response is probably the result of asymmetrical stress relaxation processes occurring during the heating and cooling cycle. Other studies correlate the thermal expansion curves to the axial tensile behavior of the composite and indicate that the plastic matrix accommodation occurring during thermal cycling controls the mechanical response of the composite [Wakashima, 1975].

Unlike the cases involving continuous fibers, the modeling of dimensional changes in short fiber MMCs requires a three-dimensional analysis. Taya and Mori proposed such a 3D model to predict the dimensional change of short fiber and particulate reinforced metal matrix composites, using an Eshelby-type model in which the average matrix stress is monitored at intervals during the thermal cycle, and the possibility of both creep and plastic deformation of the matrix considered [Taya, 1989]. Table 6 summarizes the numerous models and the assumed deformation modes of the matrix and interfaces. One common conclusion of these models (assuming perfect bonding) is the

---

[2] Progressive length changes in aligned fibrous composites is referred to as strain ratchetting.

prediction of increases in the net plastic strain per cycle with increasing fiber volume fraction, and fiber aspect ratio.

2.4.3 Residual Stresses in MMCs and IMCs The thermomechanical response of either a MMC or IMC is a complicated interaction between the fiber-matrix load transfer, the yield and creep behavior of the matrix, and the thermally induced interfacial residual stresses. Two recent publications by Clyne and Withers [1993] and Taya and Arsenault [1989] of the thermomechanical behaviors of MMC's illustrate the veracity of this statement. Since fabrication of MMCs and IMCs occurs at high temperatures, the resulting composites contain a significant amount of macroscopic elastic stresses that are produced by differential thermal contraction strains after cooling to ambient temperatures. These residual stresses are difficult to control, as they arise from the inherent fiber-matrix CTE mismatch and can continuously regenerate during thermal cycling.

To illustrate the origins of the residual stresses, Figure 10 shows a schematic illustration of the in-plane (circumferential and radial) stresses occurring in continuously reinforced MMCs. This schematic indicates that, upon cooldown from consolidation, the circumferential (or hoop stresses) are tensile, while the radial stresses are compressive. (In this discussion, as in most MMCs or IMCs, the CTE of the fiber is assumed to be less than the matrix.) The magnitude of these stresses can be large and many times are greater than the yield stress of the matrix. As an example, the interfacial stress state about a spherical SiC inclusion in a titanium matrix is shown in Figure 11 [Clyne, 1993]. Two cases are illustrated. The first case illustrates purely elastic behavior and displays the magnitudes of the calculated stresses. The second case, which is more realistic, includes a plastic zone around the fiber. The differences between the two cases include a decrease in the magnitude of the stresses, along with a change in the sign of the circumferential stress.

Table 6 Summary of models used to predict dimensional changes in IMCs and MMCs.

Model	Deformation Mode of Matrix and Interface				
	T_{min}	T_{max}	Target Composite System	Applications	Reference
Garmong	Elastic-plastic	Creep	Continuous and unidirectional fiber composites	Hypothetical	Garmong, 1974
Yoda *et al.*	Elastic-plastic	Interface diffusion	Unidirectional (short and contiuous fiber) composite	W-Cu	Yoda *et al., 1978*
Taya-Mori	Elastic-plastic	Creep and interface diffusion	Short fiber composite	SiC-Al	Taya, 1987
Min	Elastic-plastic	Elastic-plastic	Laminated Composite	Graphite-Al	Min, in press
Taya *et al.*	Elastic-plastic	Plastic-creep	Unidirectional (short and continuous fiber) composite	W-ThO2-FeCrAlY	Taya, 1991
Zhang *et al.*	Elastic-plastic	Plastic-creep	Unidirectional (continuous) and spherical inclusion composites	Computer simulation	Zhang, et al. 1993

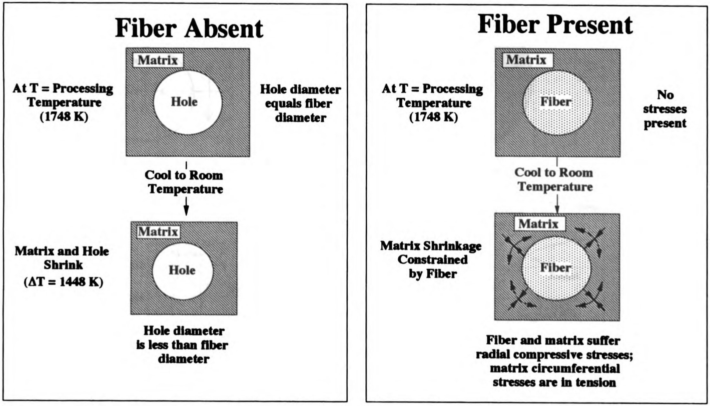

Figure 10 A schematic illustration of the origin and types of in-plane residual stresses.

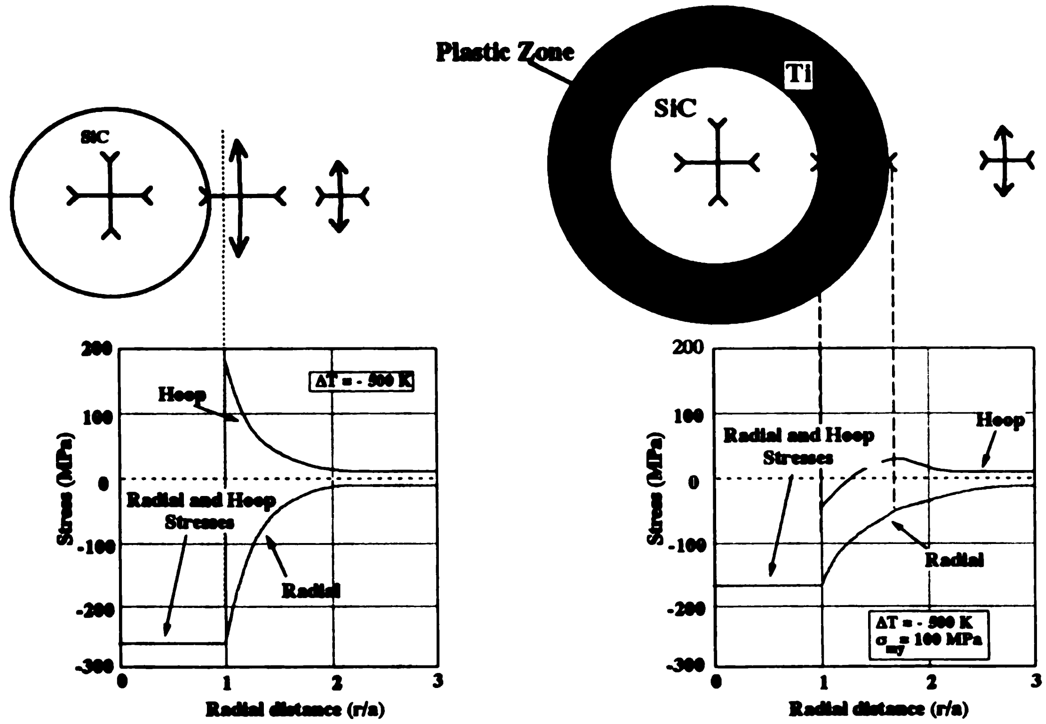

Elastic Only

Elastic + Plastic Flow

Figure 11 The stress field of a spherical particle of SiC: (a) elastic and (b) elastic-plastic.

A schematic diagram depicting the origin of residual stresses in the axial direction (parallel to the longitudinal direction of the fiber) is shown in Figure 12. In this case the thermal expansion behavior and the residual stress state of an unbonded and perfectly bonded composite are depicted during one complete thermal cycle. For the unbonded composite case, the relative expansion differences between the two constituents appear at different stages of the temperature cycle, but no stresses develop in either constituent. When perfect bonding exists, interactions between the constituents cause changes in thermal expansion and, hence, create stresses in each of the constituents. From the diagram, the matrix is in residual tension at room temperature, while the fibers are in residual compression. The evolution of these stresses is shown at different stages during thermal cycling and indicates a stress free state and a temperature when the signs of the stresses reverse. Upon cooling the original state of the stresses is recovered.

Residual stresses are traditionally categorized into three types according to the length scale over which they act [Bourke, 1993]. Type I stresses act over distances measured in millimeters and are often referred to as macroscopic. These stresses arise when different cooling rates occur within a specimen (i.e., large temperature gradients present over an extended area). Examples of Type I stress generation are forming and welding operations. Type II stresses act over lengths comparable to the microstructure (typically 1-100 μm), while Type III stresses exist at an atomic scale, such as dislocation pileups, and vary over individual grains. Type-II thermal stresses in MMCs and IMCs result from a mismatch of CTEs or intergranular interactions between the fiber and matrix. Type I stress may be minimized by cooling the composite slowly, but Type II stresses are inherent and always produce stresses. In continuous fiber composites, Type II stresses are generally dominant [Bourke, 1993].

The fiber-matrix interfacial stresses behave dynamically during thermal excursions and relaxation processes take place to lower the internal strain energy. Table

7 lists several mechanisms that reduce the load carried by the reinforcement, and hence can be classified as relaxation processes [Clyne, 1993]:

Table 7 Interfacial relaxation processes in MMCs.

Catastrophic Processes	Detrimental Processes
Inclusion Fracture	Dislocation motion
Interfacial debonding/sliding	Dislocation rearrangement
Matrix cavitation	Diffusion
—	Structural transformation
	Recrystallization

The mechanisms on the left represent catastrophic processes and ultimately lead to composite failure, while the right hand mechanisms are less detrimental to composite behavior, but do reduce the composite load-bearing capacity. For any matrix-reinforcement system, the relative incidence of these processes is a complex function of variables such as temperature, inclusion aspect ratio, the applied load, and the rate at which loads are applied.

The effect of the residual stresses on the thermomechanical behavior of well-bonded MMCs is convincingly illustrated by the yield stress asymmetry displayed in tensile-compression testing [DeSilva, 1969]. This asymmetry results when the fiber-matrix CTE mismatch prestresses the matrix in residual tension and thus lowers the macroscopic yield stress during tensile testing. Relaxation of these stresses occurs through dislocation motion and rearrangement, diffusion, creep, structural transformations and recrystallization [Clyne, 1993] that occur as the temperature increases; all of these processes reduce the load transferred to the reinforcing phase. Arsenault and Taya investigated the magnitude of the thermally induced residual stresses in short fiber SiC-Al metal matrix composites by determining the difference in the yield stresses ($\Delta\sigma_y$) between tension and compression [Arsenault, 1987]. A three-dimensional theoretical model, based on the Eshelby method, predicted residual stresses, the difference in yield stress, $\Delta\sigma_y$, and matrix stress values to be less than the experimentally determined values. The yield stress and the work-hardening rate in the compressive stress-strain curve, however, were well predicted by the model.

Larsson [1978] studied the influence of thermal stresses on the mechanical properties of tungsten fiber reinforced stainless steel metal matrix composites using thermal expansion behavior. Two methods, with terms including plasticity and creep effects, were derived for calculating the internal stresses appearing in fibrous composites. The analysis showed that thermal stresses were of such magnitude that fiber damage and matrix fatigue were possible when the composite was subjected to heating and cooling cycles. Calculations using higher fiber volume fractions accelerated the amount of thermal cycling damage, while for lower volume fractions, higher loads are imposed on each fiber. For example, the compressive fiber stress at room temperature for $V_f = 0.25$ is about 10 % higher than for $V_f = 0.75$. A similar effect can be seen on the maximum fiber tensile stress around 800 K when the composite is heated. The experimental analysis also indicated that the cooling and heating rates do not affect the expansion behavior significantly.

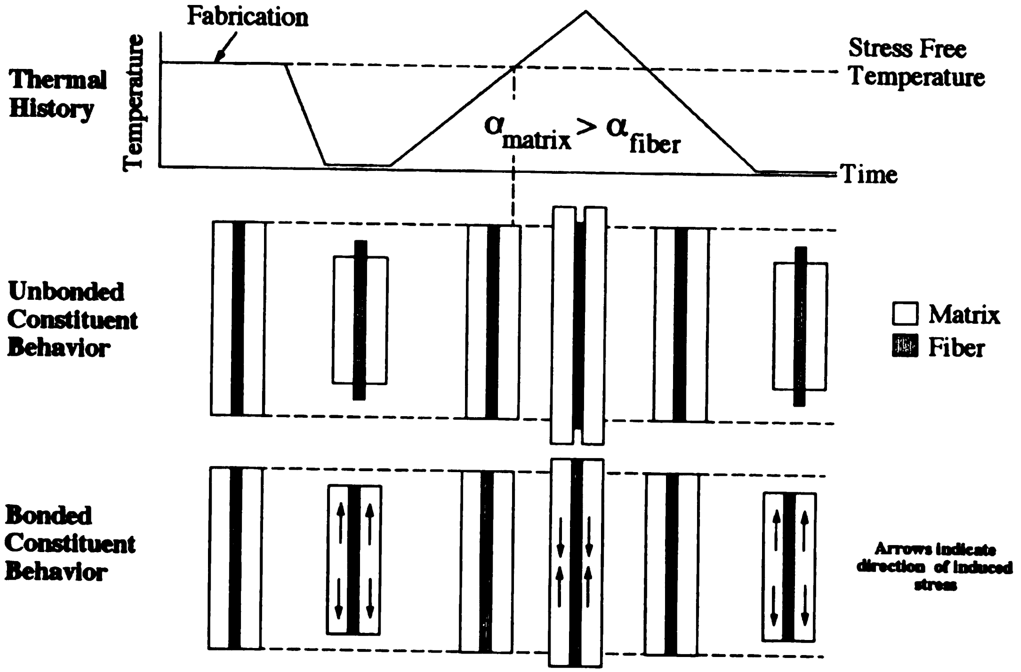

Figure 12 A schematic illustration of the origin of the longitudinal residual stresses.

CHAPTER THREE

EXPERIMENTAL PROCEDURES

3.1 Description of Materials

3.1.1 FP and Saphikon Fibers Polycrystalline FP (Dow Chemical) and c-axis single-crystal Saphikon™ (Saphikon, Inc.) Al_2O_3 fibers, having the properties described in Table 8, were used as reinforcements for a NiAl matrix. Tows of the FP fibers were cut from a large spool, then ultrasonically washed in acetone for 2 hours to remove any loose dirt, oil and contaminants from the fiber surface. The fibers were covered and allowed to dry at ambient temperature for a minimum of 5 hours. The FP fibers have a reported composition of > 99 wt.% Al_2O_3 with minor (0.01-0.1%) impurity elements of Mg, Si, Ca, Zr, and Fe [Pysher and Tressler, 1992]. The Saphikon fibers were received with a E15-LV hydroxypropyl methylcellulose (Dow Methocel™) sizing applied by the manufacturer to minimize surface damage. The sizing was removed by soaking the fibers in ice water for 1 hour and rinsing with deionized water according to the procedure outlined by Traumbauer, et al. [1992]. The fibers were subsequently allowed to dry for a minimum of 24 h. The cleaned and dried fibers were wrapped in acetone-washed aluminum foil and stored in a vacuum dessicator until used.

3.1.2 NiAl Matrix Material The extruded NiAl material used in this study was provided by Ron Noebe from the NASA-Lewis Research Center in Cleveland, Ohio. The composition of the material was Ni-49.5 at.%Al, as determined by EDX analysis, with no intentionally doped impurities.

Table 8 Properties of Al_2O_3 fibers.

Fiber	Tensile Str. (GPa)	Elastic Modulus (GPa)	Shear Modulus (GPa)	Poisson Ratio	CTE ($x10^{-6}$/°C)	wt% Al_2O_3	Fiber Diameter (μm)	Grain Size (μm)
FP	1.4	380	159	0.220	6.8	>99	20	0.5
Saphikon	2.1-3.4	414			9 (c-axis) 8.3 (a-axis)	100	150	Single crystal

3.1.3 Coating Materials The fiber coating materials consisted of niobium, titanium, and nickel. Both the nickel and titanium were in the form of 6 mm diameter rod with 99.95 purity and were purchased from Aesar Chemical Co. These rods were cut to alength 125 mm for use in a specially designed down-firing Thermionics electron-gun (see Figure 3.2.2). The dimensions of the niobium (donated by Teledyne Wah Chang Albany) were 75 mm x 100 mm x 3.17 mm with a nominal composition of 0.2 wt.% Ta, 0.05 wt.% W, and 0.02 wt.% Zr. Approximately 0.01 wt.% N, C, and O were also present. Niobium rectangles, 5 x 75 mm, were cut from the sheet an used as feed stock in the electron gun. The coating materials were lightly polished with 340 grit SiC paper to remove the surface oxidation layer, and other gross impurities, then ultrasonically washed in acetone for ~5 minutes.

3.2 Fiber Coating and Diffusion Bonding Procedures

3.2.1 Fiber Mounting Procedures The ends of 20.3 cm (8 in.) long fibers were taped onto a aluminum frame. To ensure that the fibers remained in place during the deposition process, the fiber ends were lightly coated with carbon paint as schematically depicted in Figure 13. The carbon paint was allowed to dry for at least 12 hours before connecting the aluminum frame to a mechanical feedthrough inside the vacuum chamber. This connection allowed the fiber frame to be rotated during the coating process. The geometry of the fiber coating deposition is schematically depicted in Figure 14.

3.2.2 Fiber Coating Deposition Process A custom designed rod fed, water-cooled, Thermionics 3 kV electron-beam evaporation system was used to deposit the coatings which fired downward at an angle of 30° to the vertical. The coating deposition rate was controlled by adjusting the electron-beam emission current, the length of rod protruding from the hearth, and the rod feed rate. Since deposition rates greater than 1

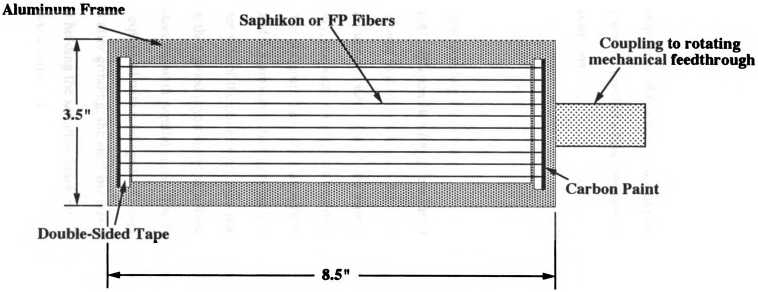

Figure 13 Schematic of fibers mounted onto an aluminum frame.

3.

w

bo

$nm \cdot s^{-1}$ generally resulted in large pieces of material spewing from the melt pool, rates less than 0.8 $nm \cdot s^{-1}$, as measured by a Leybold Inficon film thickness monitor periodically moved into position above the fibers, were utilized. The fiber holder was rotated 45° every 3 minutes to expose different areas of the fiber to the evaporated flux of atoms. This procedure resulted in an approximately uniform fiber coating thickness. Typical evaporation times of 6 hours produced coating thicknesses of ~1-2 μm. The vacuum chamber was pumped to a base pressure of $\sim 1 \times 10^{-5}$ Pa, but increased to $\sim 4 \times 10^{-5}$ Pa during the depositions.

3.2.3 The Diffusion Bonding Procedure

3.2.3.1 NiAl Diffusion Bonding Plate Fabrication Diffusion bonding plates of NiAl were sectioned to dimensions of 1.5 x 1.5 x 0.2 cm and 0.7 x 2.7 x 0.2 cm using a low speed diamond saw. The plates were polished using a sequential grinding procedure. Initially, one side of the plates was mechanically polished with SiC papers ranging from 240 to 600 grit. The plates were further polished using alumina grit (600 grit, 5 μm, and 0.3 μm) on polishing wheels covered with syvelt cloths. Similarly, the other side of the plates were then polished to a surface finish of 5 μm. These plates were then glued (cyanoacrylate adhesive), with the 0.3 μm surface down, to a rectangular steel bar with parallel sides. The NiAl plates were then machined on a surface grinder equipped with a 600 grit SiC impregnated grinding wheel. To remove the plates after grinding, the steel bar was ultrasonically cleaned in acetone until the adhesive holding the samples dissolved. This procedure produced diffusion bonding plates with parallel sides.

Continued fabrication of the NiAl diffusion bonding plates consisted of using a Materials Science Ltd. Model MK-II electro-discharge machine (EDM), with

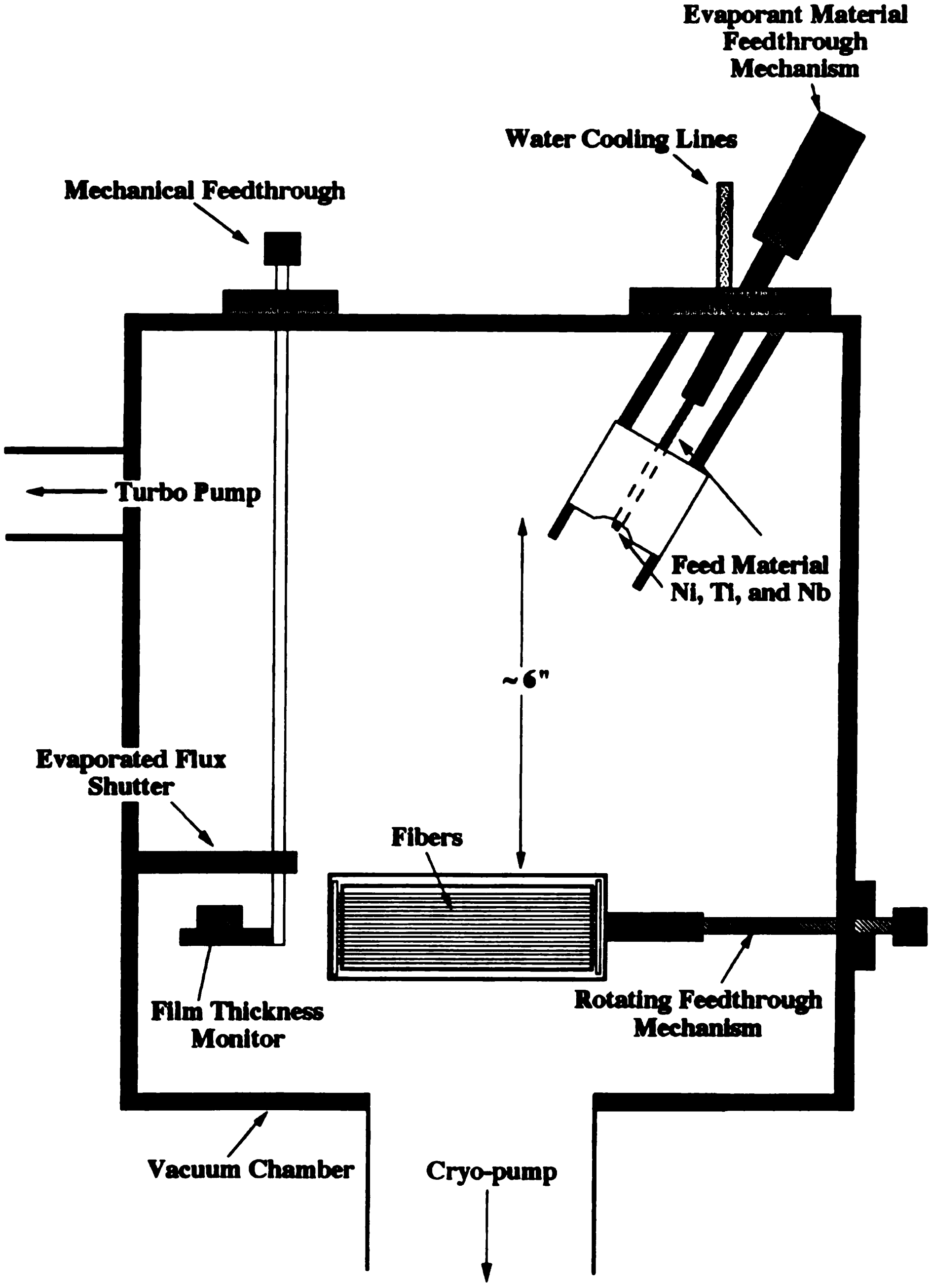

Figure 14 Schematic of the e-gun, fibers, and film thickness monitor.

settings of R = 3, C = 3, and V = 4, and custom plunger tool, as shown in Figure 15, to machine ~230 μm diameter grooves approximately 190 μm apart into the plates. Figure 16 shows a portion of an EDMed bonding plate where it can be noted that the grooves do not extend to the end of the plate. This design ensures that the fiber ends are not directly exposed to the environment. After machining, the plates were scrubbed with a nylon brush dipped in a household cleaner ultrasonically washed in warm water for 3 minutes, acetone for 15 minutes, and hexanes for 15 minutes. After the first and second washings, the plates were dried with a hot air gun, and allowed to dry naturally after the last washing.

3.2.3.2 Fiber Lay-up Methods The fiber lay-up procedure for the FP-fiber composites began with the positioning of ~10 fibers on the polished side of one of the bonding plates using a small amount of double-sided tape as shown in Figure 17, to ensure that the fibers remained in place. The polished side of the second bonding plate was then placed on top of the first plate and pressed against the fibers. The resulting specimens were approximately 9 mm wide, 18 mm long and 2 mm thick.

To fabricate the NiAl-Saphikon composites, two-ply rectangular specimens (25 mm x 6 mm x 1mm) consisting of either 5 or 7 vol% were fabricated in a manner similar to the foil-fiber-foil technique [Mackay, 1991]. The fiber volume fraction was determined by counting the number of fibers, measuring the length of the fibers, and assuming a fiber diameter of 140 μm. The fiber lay-up procedure was performed under a low power optical microscope and proceeded by placing individual fibers into each groove until all of the grooves were filled. To keep the fibers in place during handling, an extremely small amount of cyanoacrylate was placed on the fiber ends using a sharpened toothpick. The three components of the composite were then positioned together as shown in Figure 18. To prevent the NiAl plates from bonding to the TZM compression platens, boron nitride coated alumina plates were placed between the platens and the composite.

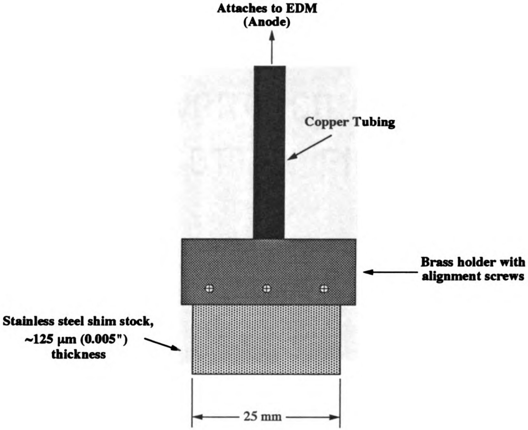

Figure 15 Electrodischarge machine plunger tool used to fabricate fiber channels.

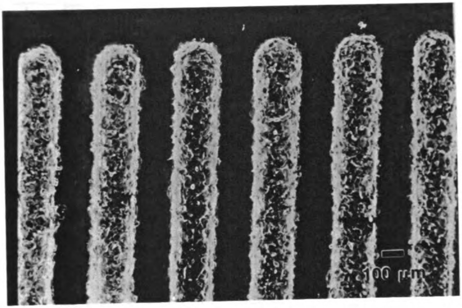

Figure 16 SEM micrograph illustrating EDMed fiber channels in NiAl.

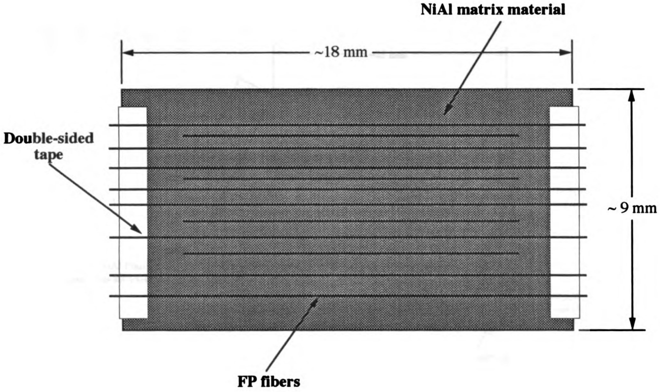

Figure 17 FP fiber composite lay-up diagram for exposed and unexposed fibers.

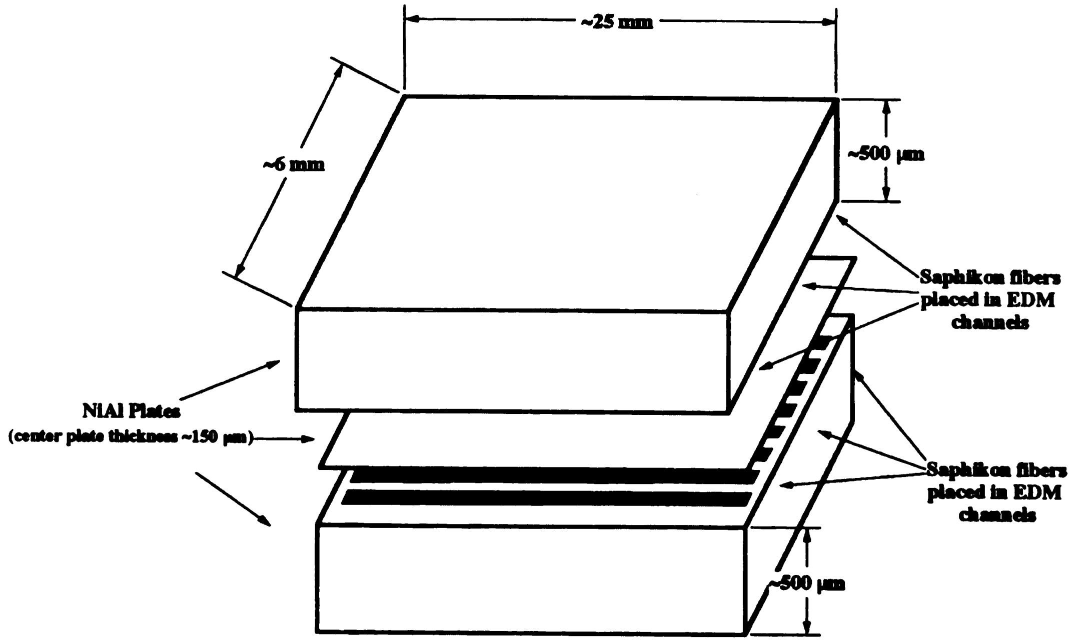

Figure 18 Schematic diagram of the Saphikon fiber composite lay-up process.

3.2.3.3 The Diffusion Bonding Process Table 3-2 shows the diffusion bonding processing schedules carried out at a pressure of ~5x10^{-3} Pa in a Centorr vacuum furnace coupled to a MTS 810 system. The heating rate was controlled at ~36 K-min^{-1} from room temperature to the maximum temperature, while the cooling rate was ~34 K-min^{-1} from the maximum temperature to 723 K, when the furnace power was turned off and the composite cooled. To minimize slipping during the heating stage of the process, a preload of ~0.5 MPa was applied to the couple. Once the maximum processing temperature was attained and held for 5 minutes, the full stress was then slowly applied over a period of 5 minutes. Just as the cooling cycle began, the load was decreased to ~0.5 MPa to minimize composite fracture during cooldown. Figure 19 is an optical micrograph of a typical NiAl-Saphikon composite.

3.3 Composite Thermal Cycling and Post-Testing Sample Preparation

3.3.1 Composite Thermal Cycling in the Temperature Range of 373 and 1173 K Composites with uncoated FP and uncoated Saphikon fibers composites were consolidated and placed in a stainless steel wire gauze envelope, sewn together with alumnel wire. The envelope was then suspended by alumnel wire attached to a motor driven pulley system which lowered the specimens to the approximate center of a tube furnace held at a constant temperature of 1173 K. After soaking for 5 minutes the specimens were raised into a forced-air cooling chamber. The temperatures and cycling limit were controlled by a CN8600 Series Process Controller from Omega Engineering, Inc. The high-temperature and cooling soak times were 5 minutes. After cooling, the specimen temperature was approximately 373 K as measured by a K-type thermocouple attached to the specimen.

3.3.2 Composite Thermal Cycling in the Temperature Range of 373 to 1423 K

NiAl-Saphikon composites were fabricated as described in section 3.2 and with fibers exposed to the atmosphere. The small hot zone of the heating lamps required composite dimensions of approximately 7 mm x 5 mm x 2 mm. As schematically depicted in Figure 20, the composites were positioned at the center of the exit hole of the heaters and were surrounded by Kaowool™ thermal insulation. A K-type thermocouple was spot-welded directly to the specimen for accurate determination of the specimen temperature. The thermal cycling experiments took place in ambient atmosphere with direct radiant heat from two parabolically focused infrared spot heaters (Research Inc.) outfitted with 750 Q/C1 quartz lamps. The cycling temperatures and times were controlled by a CN8600 Series Process Controller (Omega Engineering, Inc) connected to a 140 volt Variac and cycled between 373K to 1423 K with a high-temperature soak time of 5 minutes. The composites were allowed to cool naturally and were thermally cycled 75, 150 and 300 times with approximate cooling rate of 569 K-min.$^{-1}$ and a soak time of 5 minutes.

Table 9 Table detailing the diffusion bonding processing parameters.

Process Name	Time (hr)	Temp. (K)	T/T_m	Stress (MPa)	Comments
DB1	3	1623	0.82	20	Incomplete matrix bonding
DB2	4	1573	0.80	20	Lack of matrix infiltration
DB3	4	1673	0.85	15	Lack of matrix infiltration
DB4	4	1673	0.85	20	Fibers show substantial Creep
DB5	4	1723	0.88	5	Complete bonding for FP fibers; minimal amount of matrix deformation
DB6	4	1748	0.90	5	Saphikon Only

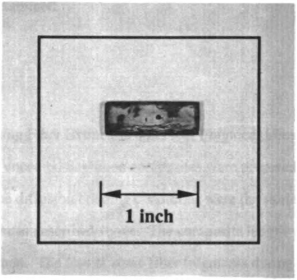

Figure 19 Optical micrograph of a typical NiAl-Al_2O_3 dilatometry composite.

3.3.3 Electroetching Procedures Matrix removal was accomplished by electroetching the surfaces transverse to the fiber direction as illustrated in Figure 21. Initially, the composite was coated with Microshield lacquer to protect all surfaces except one end of the composite. The specimen was then suspended into a beaker filled with 10% perchloric acid and 90% acetic acid which was continuously stirred by a magnetic stirring bar. The applied voltage was kept approximately constant at 12 volts, while the current varied (depending on the specimen dimensions) from 0.15 to 0.35 amps. Approximately 200 μm of the matrix was removed so that the fiber surfaces could be examined.

3.4 Post-Compositing Fiber Extraction and Fiber Fragment Length Determination

Coated and uncoated Saphikon composites were prepared as described in Section 3.2.3.2. The diffusion bonding conditions were the same as for the dilatometry composites described above. The composite length was 17 mm and with 10 fibers per specimen. The loss of some fiber fragments during filtering and transferring was unavoidable, so to minimize these losses, two composites of the coated fibers were tested, while three uncoated fiber composites were tested.

Fiber length distributions for as-composited and tensile tested composites were determined by measuring the lengths of fibers etched from the composites using a heated (340 K) bath of 50% water, 33% nitric acid, and 17% hydrochloric acid. Higher temperatures were initially tried; however, the boiling etchant caused the specimen to bounce, potentially fracturing the fibers and distorting the fiber length distribution. Typical dissolution times were 5 h. After allowing the etchant to cool, the mixture was filtered through a piece of Whatman filter paper. When the filtering was complete, fibers caught in the filter paper and left in the beaker were carefully

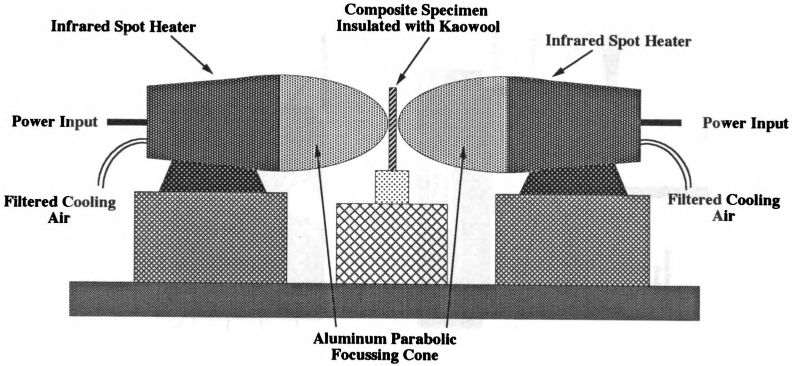

Figure 20 Schematic illustration of the high-temperature thermal cycling apparatus.

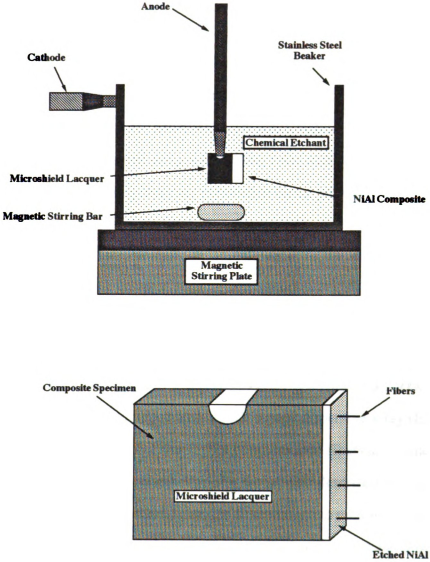

Figure 21 Schematic diagram of the electroetching procedure used to expose fibers.

rinsed with water to remove the remaining etchant. All of the fibers in the beaker were then transferred to filter paper and dried.

The extracted fibers were carefully place into a 60 mm x 3 mm polycarbonate petri dish lined with a 10 squares per millimeter grid. The fibers were then imaged with an Olympus optical microscope outfitted with a Polaroid camera. Photos were then taken at a 60 x nominal magnification until the entire set of fiber fragments were photographed. The grid served as one calibration source, while a 10 mm rule was periodically placed in a frame for additional scale confirmation. The fibers in the photographs were then measured using a millimeter ruler with an accuracy of 0.5 mm. Multiplying this value by the appropriate conversion factor provides the fiber length.

3.5 Fiber-Matrix Interface and Fiber Surface Morphology Characterization

3.5.1 Scanning Electron Microscopy The fiber surface morphological and interfacial chemical characterization was performed using a Hitachi S-2500C scanning electron microscope (SEM) equipped with a Link energy dispersive x-ray (EDX) analysis system operating at energies of 5-15 keV. For both uncoated fibers and coated fibers extracted from the matrix after consolidation by the process described in Figure 16. A gold coat ~ 15 nm thick was sputtered onto the fiber surface to minimize charging effects.

3.5.2 Fiber Surface Morphology Characterization Using Atomic Force Microscopy

Saphikon fiber surface scans were performed in height mode on a Digital Nanoscope III atomic force microscope (AFM) with the scan range and the resolution (number of data points per line) held constant. Control and composited fibers approximately 3 - 5 mm long were extracted from NiAl composites and placed on a steel sample holder coated with double-sided tape. On a captured image, the section command was used to display the cross-sectional profile. Linear roughness measurements were made on the reference centerline. The RMS (Standard Deviation) is calculated as

$$RMS = \sqrt{\frac{\sum (Z_i - Z_{avg})^2}{N}} \qquad 3\text{-}1$$

where Z_{ave} is the average of the Z values between the scan length, Z_i is the current Z value, and N is the number of points. The mean roughness, R_a, is the mean value of the roughness curve relative to the center line and is calculated as

$$R_a = \frac{1}{L}\int_0^L |f(x)| dx \qquad 3\text{-}2$$

where f(x) is the roughness curve relative to the center line and L is the length of the roughness curve. On the same images, the roughness command was used to calculate the area roughness for the entire image. Analogous relations for the area roughness parameters were calculated using:

$$RMS = \sqrt{\frac{\sum (Z_i - Z_{avg})^2}{N}}, \quad \text{and} \qquad 3\text{-}3$$

$$R_a = \frac{1}{L_x L_y}\int_0^{L_x}\int_0^{L_y} |f(x,y)| dxdy, \qquad 3\text{-}4$$

where $Z_{avg.}$ is the average of the Z values within the given area, Z_i is the current Z value, and N is the number of points within the given area.

3.6 Thermomechanical Testing Procedures

3.6.1 Dilatometry: Physical Description and Measurement Technique As shown in Figure 22, the Orton Model 10ES-1 dilatometer has a horizontal furnace design which utilizes a fused silica pushrod to transmit sample length changes to a linear variable differential transformer (LVDT). The heating rates of 2.54 K-min.$^{-1}$, 3.75 K-min^{-1}, and 4.54 K-min.$^{-1}$ were controlled by varying the starting position of the variable transformer which supplies the power to the furnace. The composite temperature was measured using a platinum/platinum-10% rhodium thermocouple placed directly on top of the composite. The outputs for both the temperature and the LVDT were connected to an Omega A-D board on a dedicated IBM XT 80086 computer. Data was taken at 1 minute intervals for both the heating and cooling segments of each cycle. The cooling segment of the cycle commenced when the furnace was automatically turned off after reaching the maximum temperature. During cooling, the rate was not controlled, since the dilatometer is not capable of decreasing the temperature, so the initial cooling rate was very fast and decreased at lower temperatures.

3.6.2 Calculation of the Instantaneous CTE Instantaneous CTE data ($\alpha = d\varepsilon_c/dT$) were calculated by fitting a straight line through 15 strain versus temperature points and assigning the slope of the line to the central temperature data point. A linear least square program was written and executed with a tolerance of 0.05. The rule-of-mixtures (ROM) instantaneous CTE was calculated from

$$\alpha_{axial} = \frac{\alpha_m E_m V_m + \alpha_f E_f V_f}{E_m V_m + E_f V_f}, \qquad 3\text{-}5$$

where the subscripts m and f represent the matrix and fiber, respectively, E is the temperature dependent elastic modulus and V is the volume fraction [Schapery, 1968].

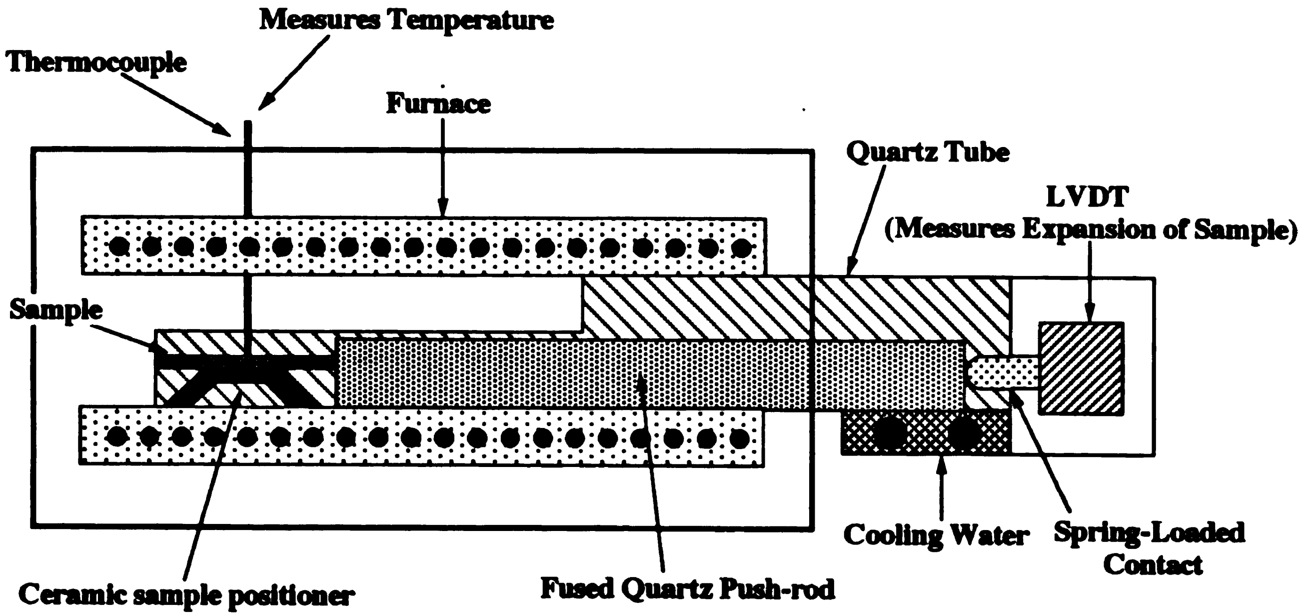

Figure 22 Schematic of the Orton Model 10ES-1 dilatometer.

3.6.3 Procedure for Fracturing NiAl-Saphikon Composites Fabricated composites, and the gripping ends of steel tongs, were placed in a Ney Model 6-525 muffle furnace at a temperature of 1323 K for 15 minutes. One end of the composites were grasped, while still in the furnace, with the tongs and fractured in bending mode either transverse or parallel to the fiber direction. The low temperature fracture specimens were produced by fracturing in bending mode at ambient temperatures. Fracture specimens were coated with ~15 nm of gold and analyzed in the SEM.

The experimental procedures are summarized and the three areas of investigation are schematically described by Figure 23.

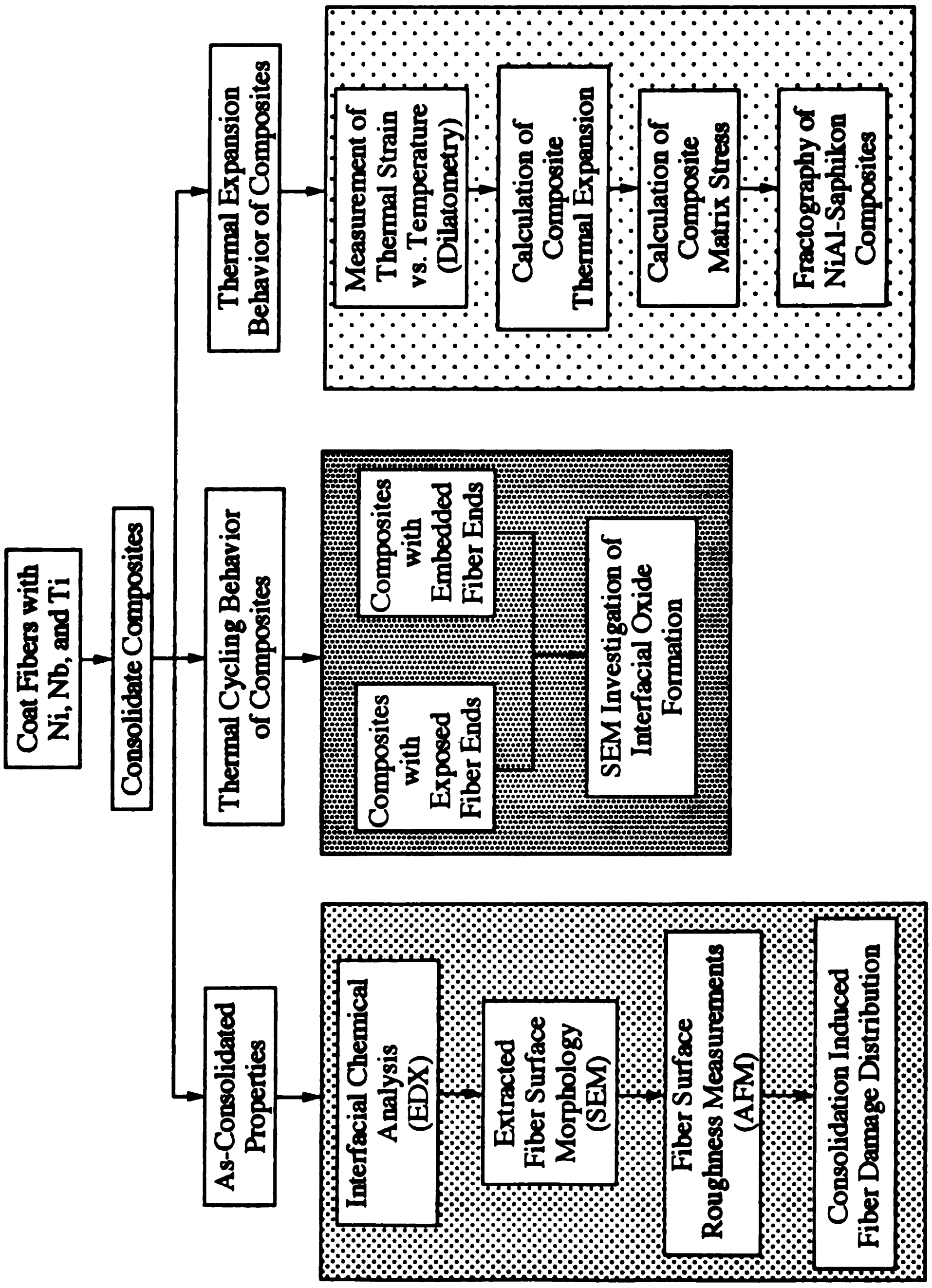

Figure 23 Flow diagram of the experimental procedures used in this investigation.

CHAPTER FOUR

RESULTS AND DISCUSSION

4.1 Surface Morphologies of Uncoated and Coated Fibers

4.1.1 FP Fibers The SEM micrograph in Figure 24 illustrates that the as-received FP fiber surface morphology consists of a cobblestone texture with no clearly defined grain boundaries. E-beam deposition of the nickel, niobium, and titanium coatings onto the FP fibers resulted in the conformally coated surfaces shown in Figure 25. All of the coatings appeared to have good adhesion to the fiber, and coating cracks were rarely seen. Figure 26 shows a cross-sectional view of a fractured Ni-coated FP fiber and illustrates a ductile coating with a thickness of ~1 μm.

4.1.2 Saphikon Fibers The surface morphology of a washed and uncoated Saphikon fiber is shown in Figure 27. The low magnification view shown by the micrograph in Figure 27a indicates a smooth surface, while the higher magnification view in Figure 27b indicates a periodic ridge structure. The small ridges on the fiber surface are oriented perpendicular to the c-axis and are presumed to be a consequence of the fiber growth process. As a typical example of a coated Saphikon fiber, Figure 28a shows the surface morphology of a titanium coated fiber. The numerous large particles scattered throughout the surface of the coating correspond to "spitting" events that occur when melt pool instabilities are caused by entrapped gases within the feed material, too high an e-beam current, and feed material extending beyond the crucible. The higher magnification micrograph in Figure 28b shows submicron grain-like regions. A crossectional view of a fractured Ti-Coated Saphikon fiber is shown in Figure 29 and illustrates a coating

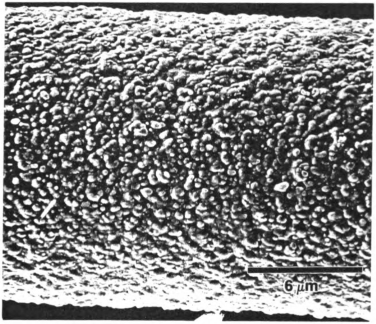

Figure 24 SEM micrograph illustrating the FP fiber "cobblestone" surface morphology.

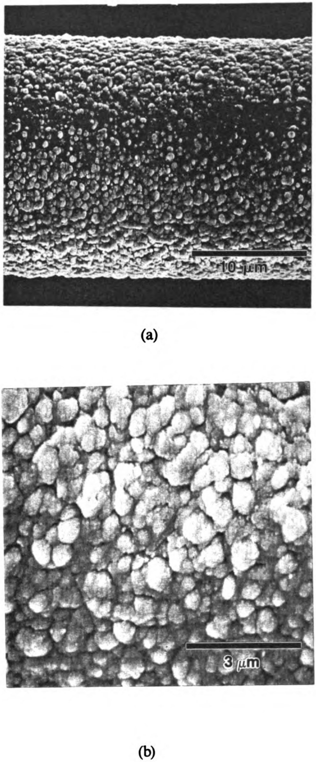

Figure 25 SEM micrographs of a Ni-coated FP fiber.

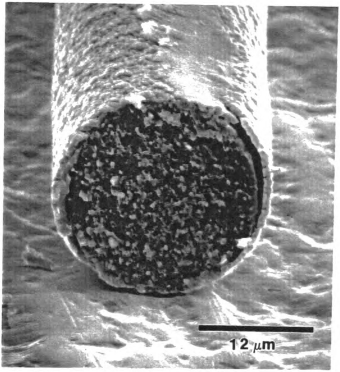

Figure 26 SEM micrograph of the cross-sectional of a Ni-coated FP fiber.

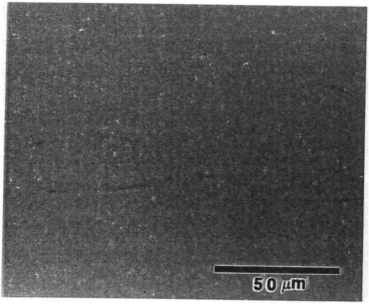

(a)

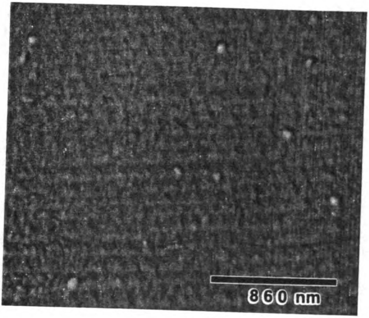

(b)

Figure 27 SEM micrographs of an as-received Saphikon fiber.

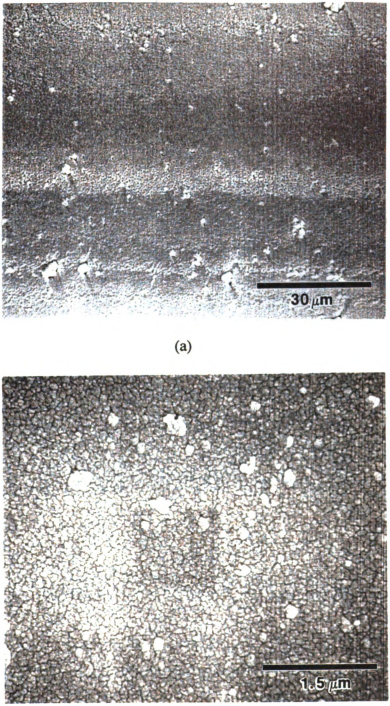

(a)

(b)

Figure 28 SEM micrographs of a Ti-coated Saphikon fiber.

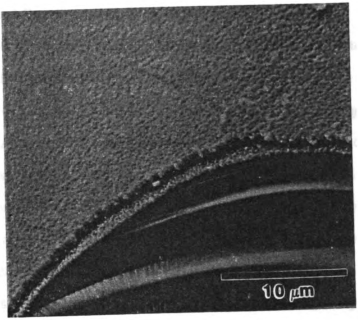

Figure 29 SEM micrograph of a fractured Ti-coated Saphikon fiber.

thickness between 1 and 2 μm. No macroscopic cracks were observed in any of the fiber coatings, and adequate fiber coating adhesion was achieved. These results suggest that the Saphikon fiber coatings were adequate for this study.

4.2 As-Fabricated Composite Microstructure

Figure 30 shows a transverse SEM micrograph of NiAl-(uncoated-FP) composite processed for 4 hours at 1723 K under an applied stress of 5 MPa. The FP fiber exhibited a substantial amount of creep, under all processing conditions, resulting in ellipsoidal cross-sections. A conservative calculation assuming an initial circular cross-section and constancy of fiber cross-sectional area indicates a transverse creep strain on the order of 25% for the fiber shown in Figure 30. Table 10 indicates other diffusion bonding conditions tried and lists comments. Lower temperatures and higher stresses, in general, lead to incomplete matrix infiltration and lack of pore closure. Since diffusion bonding is a uniaxial process, mass flow around the fiber is required to completely infiltrate the fiber.

Figure 31 shows a transverse optical micrograph of an as-fabricated NiAl/Saphikon composite indicating almost complete matrix infiltration and good fiber alignment. No tangential matrix cracks were observed, in any of the composites, though a sparse number of radial matrix cracks occurred in the Ni- and Ti-coated fiber composites. In contrast to the FP fibers, no detectable creep of the Saphikon fibers occurred. A polished longitudinal NiAl-Saphikon specimen, processed under an applied stress of 7 MPa, at a temperature of 1723 K for a time of 4 hours, is shown in Figure 32, and indicates the presence of some voids, but mostly macroscopically well-bonded interface regions. No composite curvature in the thickness direction was noted, and

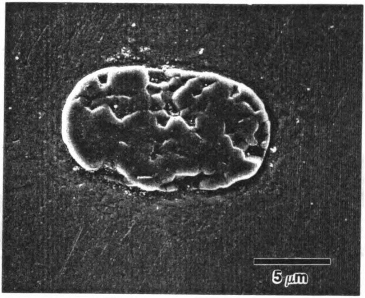

Figure 30 SEM micrograph of a transverse section of a NiAl-uncoated FP fiber.

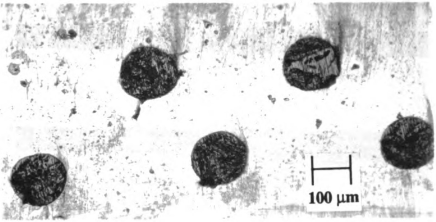

Figure 31 An optical micrograph of a cross section of a NiAl-(Ni-Saphikon) composite.

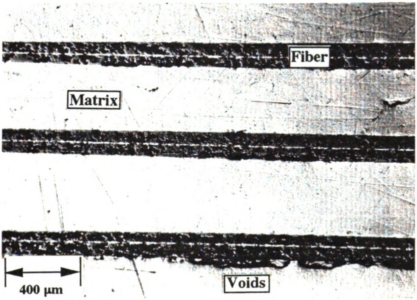

Figure 32 Optical micrograph of a longitudinal section of a NiAl-Saphikon composite.

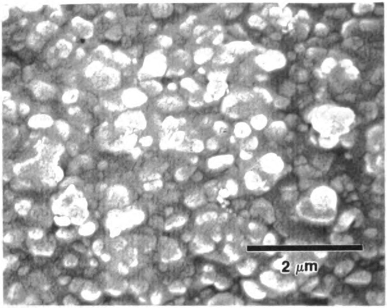

Figure 33 SEM micrograph of an as-received FP fiber after submersion in etchant.

consistent with other composite processing schemes, the consolidated fibers are often coincident with grain boundary triple points.

4.3 Extracted-Fiber Surface Morphology

4.3.1 Uncoated Fibers Figure 33 is an SEM micrograph of an as-received FP fiber subjected to the same etching treatment as composited fibers. The absence of pitting or surface morphology alterations illustrates that the etching procedure has no observable effect on the fiber. In contrast to this result, Figure 34 illustrates many changes in the surface morphology of an uncoated FP fiber processed for 4 hours at 1723 K with an applied stress of 5 MPa. In general, the effects of the consolidation were dominated by extensive grain growth (~300 % increase), though fiber fracture in the longitudinal and transverse directions occasionally occurred. The SEM micrograph in Figure 34b reveals that the grain boundaries remain cohesive and pitting is not observed. (Note the particulate material dotting the fiber surface corresponds to NiAl particles that were not completely dissolved during the etching process.) As illustrated in Figure 35, lower processing temperatures, combined with higher applied stresses, resulted in severe grain boundary decohesion and surface pitting. As a trend, the severity of the induced fiber surface damage depends primarily on the consolidation temperature and the applied stress, with the processing time exerting a lesser influence.

The fiber surface morphology of an extracted uncoated Saphikon fiber processed for 4 hours at 1748 K and an applied stress of 5 MPa is shown in Figure 36. One difference between the as-received fiber surface morphology and the as-processed surface morphology is the appearance of thermally grooved grain boundary imprints, with widths ranging from 1.2 μm to 0.33 μm, and an average height of ~287 nm. In addition, numerous pores, ~ 350 nm in diameter, are randomly distributed on the fiber surface. As in the FP fiber case, the exact cause(s) of the pitting is unknown. (To determine if the etchant affected the fiber surface morphology, cleaned as-received fibers were also subjected to the matrix etchant dissolution process, and no fiber surface morphology alterations were observed.) Similar features have been reported by other workers investigating Al_2O_3-NiAl composites fabricated by the powder cloth technique and by binderless techniques [Draper, 1994; Asthana, 1995].

4.3.2 Nickel-Coated Fibers The surface morphology of an extracted nickel-coated FP fiber, consolidated for 4 hours at 1748 K and an applied stress of 5 MPa, is shown in Figure 37a. Along with the increased grain size, a significant amount of intergranular cracking has occurred. A small amount of pitting is also apparent, though no obvious gross chemical reaction has occurred.

Figure 37b shows the fiber surface morphology of a Ni-coated Saphikon fiber processed for 4 hours at 1748 K and a stress of 5 MPa. The micrograph displays a random distribution of smooth and rough regions decorated with submicron pits. According to Table 11, a spinel reaction product forms at high temperature from nickel-Al_2O_3 reactions. (A large negative value of ΔG_0 is indicative of a reaction with a large thermodynamic driving force.) The EDX spectrum, shown in the inset of Figure 37c, contains a nickel signal, which indicates the possibility of a reaction product, though the signal may correspond to small amounts of matrix material adhering to the fiber surface. Since the consolidation temperature was 20 K above the melting point of nickel , and, since only a finite amount of nickel was available for reaction, the Al_2O_3-nickel chemical reactions probably occurred during the early stages of the consolidation process.

4.3.3 Titanium-Coated Fibers The SEM micrograph shown in Figure 38a illustrates how the chemical reactions between the titanium coating and Al_2O_3 affects the surface morphology of a FP fiber processed for 4 hours at 1748 K with an applied stress of 5 MPa. The titanium-Al_2O_3 chemical reaction(s) are so extensive that the grain boundary structure of the fiber is difficult to discern. Large pits appear both in the grain

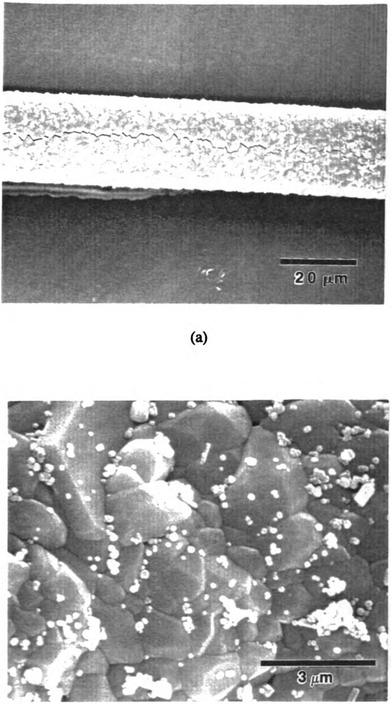

(a)

(b)

Figure 34 SEM micrographs of an uncoated FP fiber showing grain growth.

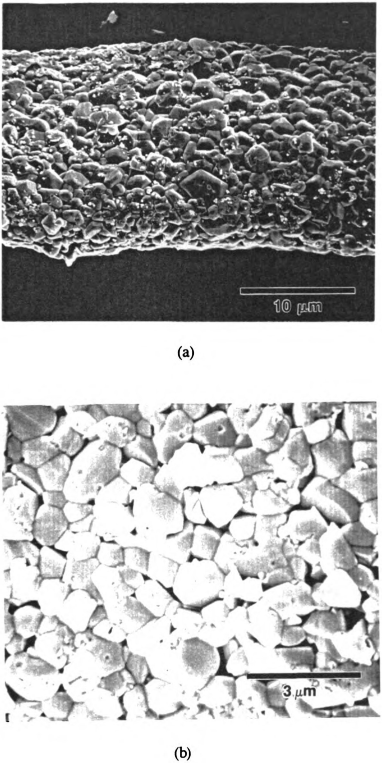

Figure 35 SEM micrographs of an uncoated FP fiber consolidated with a high stress.

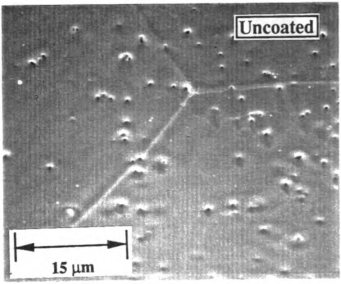

Figure 36 SEM micrograph of an extracted uncoated Saphikon fiber.

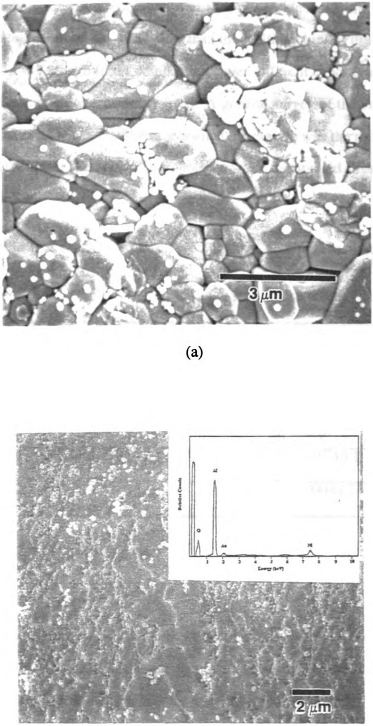

(a)

(b)

Figure 37 SEM micrographs of a nickel-coated (a) FP fiber, (b) a Saphikon fiber.

interior and at the grain boundaries, while smaller pits reside inside the larger pits. The consolidation temperature was 125 K less than the melting point of titanium (1623 K). Similar behavior was seen in fibers composited under different conditions, but in all cases significant fiber-coating reactions occurred. A general survey of the various diffusion bonding parameters indicates that the processing temperature was the most significant parameter in determining the surface morphology, while the applied stress and time were less important.

Table 10 Gibbs free energy for nickel, niobium, and titanium reactions with Al_2O_3.

Reaction	ΔG_R^0 (1000 - 1400K) (kJ)	Ref.
$(1/3)Al_2O_3 + Ti = TiO + (2/3)\ Al$	3.49 (1300K)	Barin, 1973
$(2/3)Al_2O_3 + Ti = TiO_2 + (4/3)\ Al$	133.59 (1300K)	Barin, 1973
$8Ti + Al_2O_3 = 3Ti_{0.67}O_{0.33} + 2Ti_3Al$	$-1807.8 + 0.0167\ T \ln(T) - 0.367\ T$	Kang, 1990
$(1/3)Al_2O_3 + Nb = O + (2/3)\ Al$	$1327.5 - 0.01735\ T$	Howe, 1993
$Ni + (1/2)O_2 + (1/3)\ Al_2O_3 = NiO \bullet (4/3)Al_2O_3$	$-60.09 + 0.0044\ T$	Lenev, 1965

A SEM micrograph of the titanium-coated Saphikon fiber surface morphology (consolidated for 4 hours at 1748 K under an applied stress of 5 MPa) is shown in Figure 38b and reveals a topography with relatively smooth regions surrounded by protrusions. Figure 38c is an SEM micrograph of a smooth region of the fiber surface which shows the presence of numerous submicron pits. Similar to the nickel-coating case, the consolidation temperature was above the melting point of titanium (~55 K). This suggests that the reaction product formation and roughening occurs during the early

st
co
th
ov
be
sp
pr
Al
su
of
po

co
fib
nic
Fi
pro
ob
lar
rer
po
ma
ma

fibe
nio
Gib

stages of composite consolidation and terminates quickly since the titanium coating is consumed. Table 11 lists three possible reaction paths between titanium and Al_2O_3. The third reaction ($8Ti + Al_2O_3 = 3Ti_{0.67}O_{0.33} + 2Ti_3Al$), showing the formation of titanium oxide and titanium aluminide intermetallic reaction products, is the most probable because it has the largest negative free energy change [Wang, 1993]. Though the EDX spectrum of the fiber surface shown in the inset of Figure 38b does not indicate the presence of titanium, the reaction products may have been dissolved by the etchant. Also, fibers from other processing conditions did show titanium present on the fiber surface. The other two reactions have slightly positive Gibbs free energy, but trace levels of impurities and higher temperatures, may make these reactions thermodynamically possible.

4.3.4 Niobium-Coated Fibers In contrast to the titanium-coated and nickel-coated fibers, a slightly different morphology develops for processed niobium-coated FP fibers. The SEM micrograph in Figure 39a illustrates a typical surface morphology of a niobium-coated FP fiber processed for 4 hours at 1723 with an applied stress of 5 MPa. Fiber surface impressions, or possibly chemical reaction sites, ~0.25 μm in diameter, are present in the grain interiors, and some grain boundary decohesion is also present. One observation seen in this system, but not seen in the nickel and titanium system was the large amount of residual niobium remaining on the fiber surface. This fiber coating remnant is a result of the etching not attacking the niobium vigorously. Since the melting point of niobium is 2750 K (1027 K greater than the processing temperature), the coating material did not liquefy, but should have been sufficiently soft for creep and flow of the material to occur.

Figure 39b shows the fiber surface morphology of a niobium-coated Saphikon fiber. The small undulations shown by the micrograph in Figure 39b indicates that the niobium coating caused significant chemical dissolution of the Al_2O_3 fibers. Though the Gibbs free energy of reaction in Table 11 is positive, experimental reports indicate that

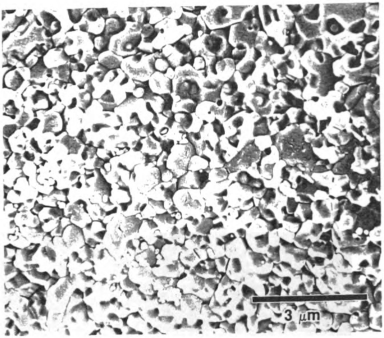

(a)

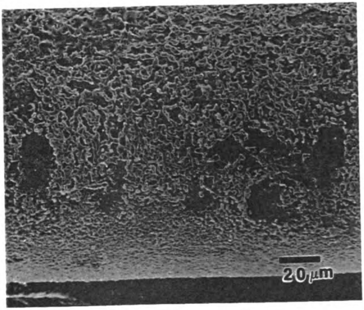

(b)

Figure 38 SEM micrographs of a titanium-coated (a) FP and (b), (c) Saphikon fibers.

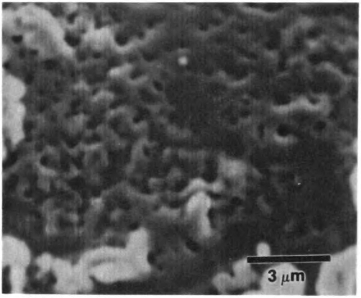

(c)

Figure 38 (cont'd).

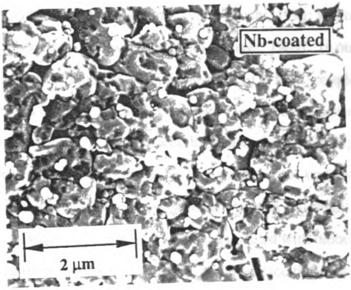

(a)

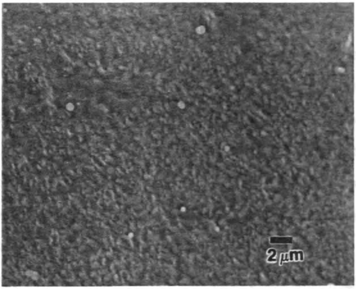

(b)

Figure 39 SEM micrographs of Nb-coated (a) FP, and (b) Saphikon fibers.

4

m

th

ro

re

pe

Fig

unc

con

The

In c

cons

niobium reacts with Al_2O_3 at high temperatures by dissolving the aluminum and oxygen atoms into solution with the niobium [Klomp, 1987; Ohuchi, 1991; Morozumi, 1981; Turwitt, 1985], and, hence, no reaction zone forms [Burger, 1989]. In our case, the intimate contact between the niobium coating and the Al_2O_3 fiber, coupled with the high vacuum of the diffusion bonding process, promotes a favorable condition for a redox dissolution reaction [Howe, 1993]. Fiber facetting is also observed in Figure 16c; however, at this time the mechanism(s) for this observation is not understood, but could be a consequence of the fiber manufacturing process. Another investigator studied the interfacial behavior of single-crystal Al_2O_3 fibers composited with niobium, at higher temperatures and pressures, but for shorter times, and fiber facetting was not observed [Petrich, 1993].

4.4 Surface Roughness Measurements on Extracted Fibers

Since energy dissipation associated with frictional sliding of the fiber against the matrix, is a major contributor to the toughness of composite, quantifying the roughness of the interface topography is important. AFM microscopy was used to quantify the surface roughness of the extracted Saphikon fiber fragments. A typical line profile of an as-received and cleaned Saphikon fiber is plotted in Figure 40. Only small, somewhat periodic undulations are observed. A typical line profile of the uncoated fiber shown in Figure 41a, measured away from the grain boundary ridges, indicates only small undulations. As shown in Figure 41b, the nickel coatings produced a roughness curve consisting of large amplitude, long wavelength deviations separated by smooth regions. The niobium-coated fiber line profile shown in Figure 41c has large, smooth, deviations. In contrast to these three profiles, the titanium-coated fiber profile shown in Figure 41d consists of a continuous spectrum of small amplitude, short wavelength, regions joined by a small number of large amplitude asperities. All of these observations are qualitatively consistent with the SEM results of Figures 36 through 39.

The linear and area surface roughness values are reported in Table 12. These data indicate that the diffusion bonding process decreased the surface roughness of uncoated Saphikon fibers from a mean roughness, R_a, value of 1.61nm to 0.33 nm. This comparison, combined with the surface morphologies shown in Figure 27 and Figure 36, suggests that fiber dissolution occurred during the consolidation process. Though thermodynamic calculations rule out NiAl-Al_2O_3 reactions below 1583 K [Misra, 1986], small amounts of interfacial impurities combined with a processing temperature of 1748 K may make such reactions favorable [Calow, 1972]. Table 12 also indicates that the mean roughness of the titanium-coated fiber is ~490 times greater than the extracted uncoated fiber, while the nickel- and niobium-coated fibers are ~150 times rougher. These results are consistent with the SEM results and, in particular, indicates that increasing the surface roughness increases the fiber coating-fiber chemical reactivity.

4.4.1 Discussion of the Correlations between Fiber Surface Roughness, Residual Thermal Stresses, and Interfacial Mechanical Properties The interfacial parameters contributing to composite mechanical response include fiber-matrix adhesion, residual clamping stresses, and frictional stresses. Interfacial friction stresses occur when, after debonding, fiber sliding causes interfacial irregularities to move against each other, while the residual thermal stresses arise from fiber-matrix CTE mismatch. These stresses affect the load carrying ability and pull-out behavior of the fibers and, hence, the composite toughness. For both types of stress, the frictional sliding forces produce an interfacial stress given by $\tau_{interfacial} = \mu\sigma_r$ (where μ is the coefficient of friction between the sliding surfaces and σ_r is the radial stress). For an undisplaced fiber, σ_r, is caused by residual clamping stresses only, while for a partially debonded fiber, contributions from both types of stresses occurs.

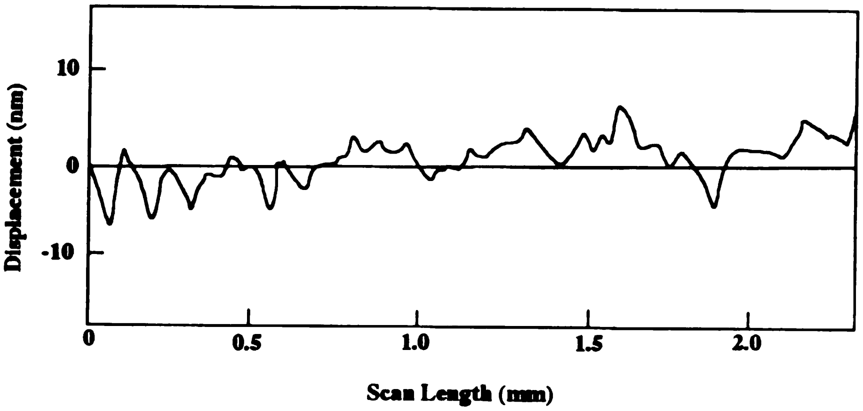

Figure 40 Typical AFM line scan illustrating the undulating surface of a Saphikon fiber.

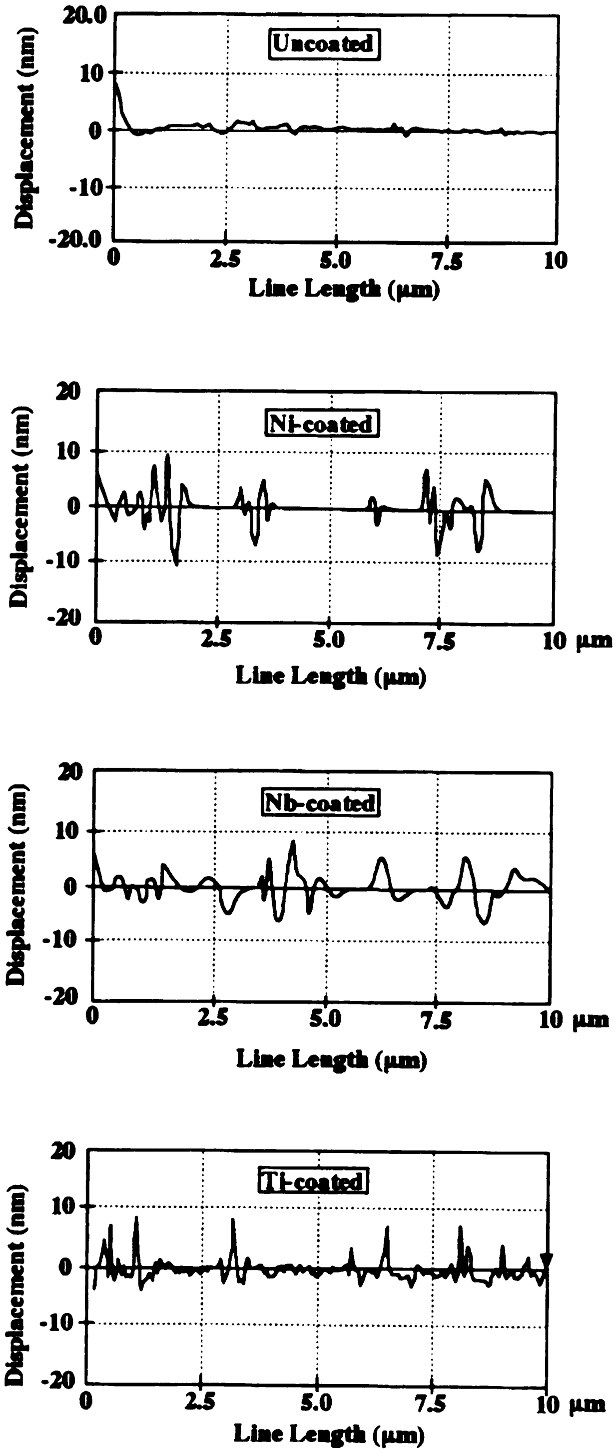

Figure 41 AFM scans of (a) uncoated, (b) Ni-, (c) Nb-, and (d) Ti-coated Saphikon fiber.

To assess the effects of the fiber surface roughness on the frictional stress, a model developed by Kerans and Parthasarathy will be used [Parthasarathy, 1994]. In this model, the radial frictional stress is related to the roughness according to:

$$\sigma_{\text{rough}} = \Lambda\left(\frac{A}{r}\right), \qquad 4\text{-}1$$

where

$$\Lambda = k\left(\frac{E_f}{V_f}\right), \qquad 4\text{-}2$$

and $$k = \frac{E_m V_f}{E_f(1+V_m)+E_m(1+V_f)}. \qquad 4\text{-}3$$

Here A is the effective roughness amplitude, r is the fiber radius, E_i the elastic modulus of either the fiber or matrix, and V_f and V_m the Poisson's ratio of either the fiber (f) or matrix (m). (Note that this expression rigorously applies only after complete debonding of the fiber when the relative fiber-matrix displacement is large compared to the half period of the roughness and . It would be expected, however, that the roughness would play a role even when the displacements are smaller than the half period of the roughness, although the relative importance should decrease.)

An exact analysis of the thermal stress problem in IMCs usually requires a rigorous numerical solution because the constituent phases, particularly the matrix, can behave as an elastic/plastic/creep body under thermal loading. However, in this section the main consideration will be an analysis based on an elastic body which provides an upper bound on the actual thermal stress in the composite. Following the derivation of the thermal residual stresses in a fiber embedded in an infinite matrix, the radial component of the residual stress can be written as [Taya, 1989]:

$$\sigma_r = \frac{(G_f + G_m)(2G_m + 3\lambda_m)}{G_f + G_m + \lambda_m}(\alpha_f - \alpha_m)\Delta T \qquad 4\text{-}3$$

where

$$\lambda_m = \frac{V_m E_m}{(1+V_m)(1-2V_m)} \qquad 4\text{-}4$$

and G_m is the shear modulus of the matrix. Following the analysis by Taya and Arsenault [1989], the axial residual stress given by is:

$$\sigma_m = \frac{V_f E_m E_f \Delta\alpha \Delta T}{E_c} \qquad 4\text{-}5$$

where

$$\Delta T > 0,\ \Delta\alpha = \alpha_m - \alpha_f,$$

and E_c is the rule of mixtures composite modulus.

Using equations 4-1, 4-3, and 4-5, and the material constants in Table 5 and Table 10, together with the average and maximum fiber surface roughnesses for each type of fiber in Table 12, the frictional, radial and axial stresses were calculated and tabulated in Table 13. The histogram in Figure 42a compares the frictional stresses calculated from the average surface roughness of the uncoated and coated fibers. The calculated frictional stress of 0.108 MPa for the uncoated fiber is too small to be apparent on this plot. In contrast, the nickel- and niobium-coated fibers produce frictional stresses of ~20 MPa, while the roughness of the titanium-coated fiber produces a frictional stress more than twice this value. Using the maximum roughness values, the frictional stresses were calculated and plotted in Figure 249b. A similar trend to Figure 249a is observed; however, the frictional stresses are now above 100 MPa (except for the uncoated fiber). Frictional stresses of this magnitude approach the NiAl tensile yield stress, which is temperature dependent and ranges from 75 - 600 MPa [Noebe, 1993].

Table 11 Calculated roughness values for uncoated and coated extracted fibers.

Fiber	Linear Roughness			Area Roughness		
	R_{rms} (nm)	R_a (nm)	R_{max} (nm)	R_{rms} (nm)	R_a (nm)	R_{max} (nm)
As-recieved	2.32 ±0.06	1.61 ±.001	11.30 ±.10	3.3 ±.07	2.6 ±0.06	25.9 ±0.04
Uncoated	0.57 ±0.04	0.33 ±0.06	3.0 ±0.3	1.1 ±0.08	0.52 ±0.04	20.8 ±0.07
Nickel-coated	106.6 ±15.7	81.1 ±12.2	383.2 ±18.3	96.9 ±9.4	79.35 ±13.9	686.1 ±52.4
Titanium-coated	223.3 ±104.5	148.1 ±21.4	850.2 ±354.2	304.6 ±32.4	253.1 ±28.5	1840 ±386
Niobium-coated	81.0 ±14.2	81.3 ±16.0	260.6 ±33.4	106.3 ±18.4	85.0 ±24.4	525.5 ±72.1

The analysis by Kerans and Parthasarathy indicates that the critical parameter influencing the frictional stress is the ratio of the roughness amplitude to the fiber diameter. This implies that the maximum frictional stress associated with displacing a 10 μm diameter FP fiber would be greater than the stress associated with displacing a 140 μm diameter Saphikon fiber with the same roughness amplitude. Though no roughness measurements were made on the FP fibers, the SEM micrographs indicate that grain growth and surface roughening produce roughness amplitudes greater than that measured for the Saphikon fibers. This suggests that the frictional stresses during fiber pull-out willbe greater for the smaller diameter FP fiber and, hence, may improve composite toughness.

The thermal stresses tabulated in Table 13 represent ideal values, since no allowances were made for an interphase region, such as a coating or reaction zone, and no plasticity terms were included. The limitations to this calculation are obvious since a value of 17.5 GPa for the thermal residual radial stress is 100 times greater than the room temperature yield stress of the matrix. On the other hand, a value 194 MPa for the axial residual stress is relatively close to the experimentally measured NiAl yield stress of 125 MPa [Noebe, 1993; Dutta, 1993]. A more accurate technique, based on the thermal expansion behavior of a composite, which takes into account the elastic/plastic/creep properties of the composite, will be presented in section 4-10.

4.5 Interfacial Chemical Analysis of As-Consolidated Composites

4.5.1 EDX Analysis of As-Composited Interfaces Figure 43a shows the aluminum, nickel, and titanium x-ray line scans across a titanium-coated FP fiber-matrix interface processed at 1673 K (the melting point of titanium is 1693 K) under an applied

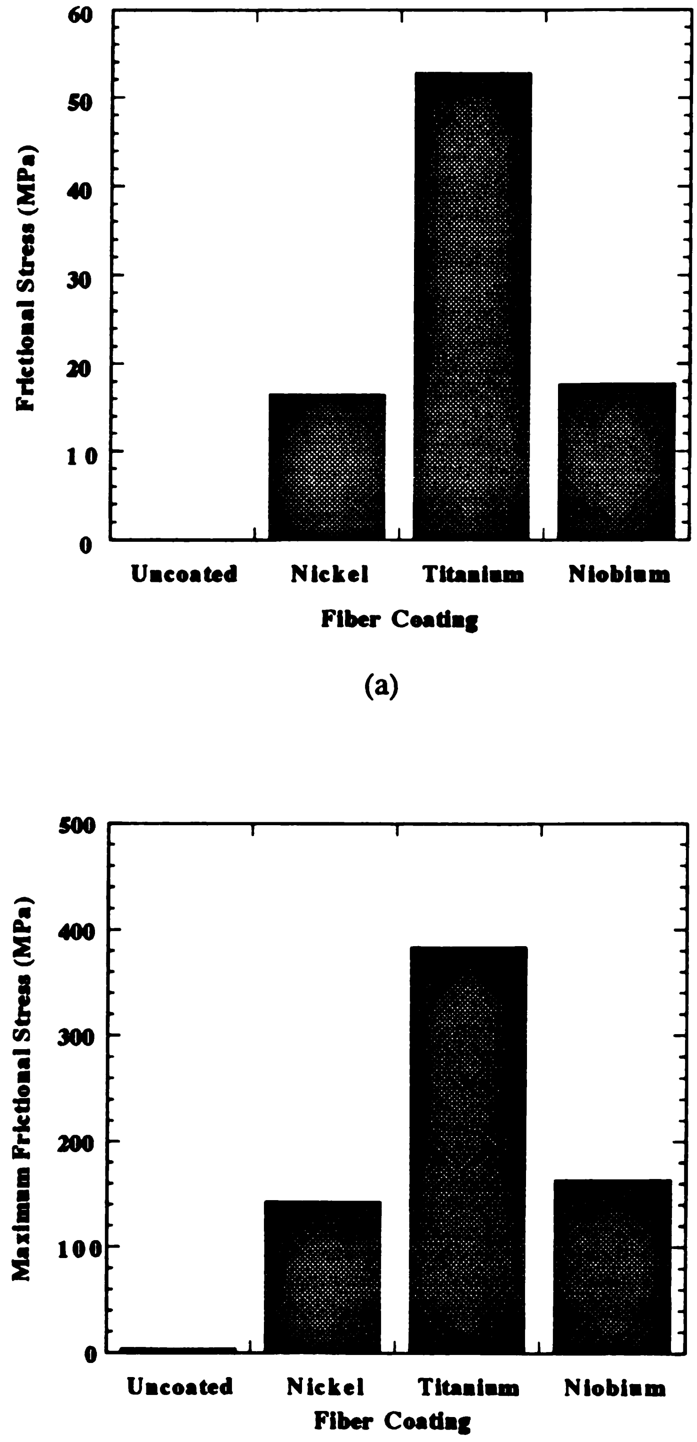

(a)

(b)

Figure 42 A histogram comparing the calculated frictional stresses.

stress of 15 MPa for a time of 4 hours. The full-width half-maximum of the titanium x-ray peak is ~0.75 μm, and the signal disappears ~1.5 μm from the fiber interface.

In Figure 250b, the energy dispersive x-ray spectrum, acquired with the beam placed on the matrix ~1 μm from the fiber-matrix interface indicates a strong nickel peak at 7.48 keV, an aluminum peak at 1.48 keV, and a titanium peak at 4.51 keV. The peak at 2.12 keV originates from the thin gold film sputtered onto the sample to minimize charging effects.

The spatial resolution of SEM x-ray analysis, 1 μm, makes an exact determination of the diffusion of titanium into either the matrix or the fiber difficult; however, Weber et al., performed a TEM investigation which indicated that limited titanium diffusion occurs in both polycrystalline alumina (~0.8 μm) and Saphikon fibers (~0.2 μm) [Weber, 1993] composited with Ti_3Al processed at 1373 K for 2 hours. In the present case, the diffusion bonding temperature was ~20 K less than the melting point of titanium. This higher processing temperature increases the diffusivity of titanium into the matrix and the reactivity of titanium with Al_2O_3. Since the original thickness of the titanium-coating was ~1 μm, the detection of titanium near the interface suggest the presence of reaction products with the fiber or matrix or both.

Table 12 Calculated fiber-matrix interfacial stresses.

Fiber Coating	Frictional Stress (MPa), (R_a)	Frictional Stress (MPa), (R_{max})	Axial Stress (MPa)	Radial Stress (GPa)
Uncoated	0.108	4.34	194	17.5
Nickel	16.55	143.1		
Titanium	52.79	383.8		
Niobium	17.73	164.2		

In contrast to composites processed at the lower temperatures, several attempts at characterizing the fiber-matrix interfaces in 7-vol.% NiAl-(Ti-Saphikon) composites consolidated at 1748 K resulted in a titanium signal localized at the interface with little, if any, signal originating from the matrix. Since the diffusion bonding temperature was ~50 K greater than the melting point of titanium, the fiber coating liquefied and reacted vigorously with the fiber. The liquid titanium phase, combined with the applied stress of the bonding process, can be expected to be extruded along the interface and to diffuse into the matrix material. This processing condition is anticipated to cause a transient condition that terminates during the composite consolidation procedure.

Figure 44 shows an SEM micrograph with nickel, aluminum, and niobium x-ray line scans of a Nb-coated Saphikon fiber, diffusion bonded for 4 hours at 1723 K (a homologous temperature of 0.63) with an applied stress of 10 MPa. Here the full width half maximum (FWHM) of the niobium peak is ~1μm. EDX analysis of Ni-coated fibers was impractical due to the large nickel content of the matrix.

4.5.2 Discussion of Possible Fiber-Coating and Coating-Matrix Reactions

Engineering the microstructure at the fiber-matrix interface is essential for controlling the mechanical behavior of the composite. When considering possible scenarios of the interfacial processes that can occur during the diffusion bonding process, reactions between the fiber and the coating, along with reactions between the matrix and coating, must be considered. Some consequences of the fiber-coating reactions, like fiber surface roughness and surface chemistry, have been previously described. These concepts will be discussed further, and the coating-matrix reactions elaborated on.

Metal-Al_2O_3 reaction products forming a reaction zone between the fiber and the matrix represent the severest case of metal-ceramic reactivity. The thickness of the reaction zone plays a crucial role in altering the strength of a continuous fiber metal matrix composite. For instance, if the reaction zone is thicker than a critical dimension,

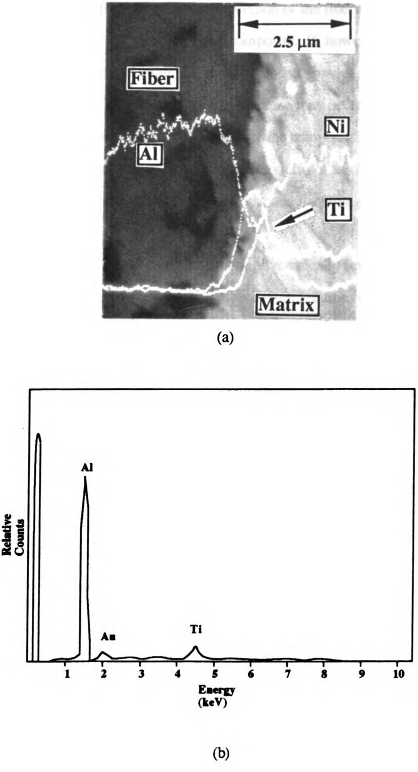

Figure 43 (a) X-ray line scans and (b) EDX spectrum of a Ti-coated FP fiber interface.

the cracks (radial or circumferential notches) formed in the reaction zone upon loading will effectively increase the intrinsic flaw population of the fiber and induce fracture. This behavior will reduce the strength of the composite. If, however, the reaction zone product is less than the critical value, the intrinsic defect population on the fiber dictates the strength of the fiber. The reaction zone in this case may act to increase the fiber matrix adhesion and, consequently, the strength of the composite. The critical thickness is a function of several parameters, including the modulus of the fiber, the stress distribution around the crack, the crack root radius, and the strength of the fiber [Metcalfe, 1972].

Though chemical reactions may be thermodynamically favorable, the kinetics of the reaction(s) must be investigated before proper interpretation of reaction zone effects can be made. Most studies of metal-ceramic reaction zone thickness support a parabolic growth rate model which can be expressed as,

$$x^2 = 4Dt \qquad 4\text{-}6$$

where x is the reaction zone thickness, D is the diffusion coefficient, and t is the time [Taya, 1989]. The temperature dependence of the reaction zone thickness is contained in the diffusion coefficient of Equation 4-6. Rewriting this equation, the explicit temperature dependence is contained in an exponential term as,

$$x = CD_o\sqrt{t}\exp\left\{\frac{-Q}{2kT}\right\}, \qquad 4\text{-}7$$

where C is constant , D_0 is the preexponential term, Q is the activation energy controlling the reaction zone growth, k is Boltzmann's constant, and T is the temperature. This analysis illustrates the importance of the kinetics, and helps predict the metallurgical stability of the interface. For the case of coated fibers, the thickness of the coating

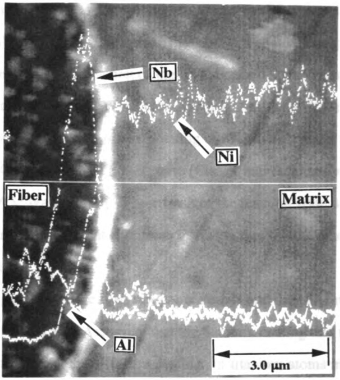

Figure 44 SEM micrograph of a NiAl-(Nb-coated Saphikon) interface.

determines the ultimate extent of the reaction zone. Once the coating is consumed by either the matrix or the fiber, the reaction terminates. Thus, a transient reactivity is established during the early stages of consolidation and does not persist into the lifetime of the composite. This approach provides a measure of interfacial metallurgical stability.

One of the most important classes of reaction at metal-ceramic interfaces is the reduction-oxidation (redox) reaction with an accompanying dissolution of one or both of the ceramic elements. The Ti-Al_2O_3 system serves as a model system with a strong interfacial chemical reaction (i.e., the kinetic rate constant and the change in Gibbs free energy is very large), where a reduction of the Al-O bonds occurs [Morozumi, 1981; Turwitt, 1985]. Tressler et al. and Wang et al., have determined that the titanium reduces Al_2O_3 to form a complex reaction zone consisting of two distinct zones; an inner zone adjacent to the Al_2O_3 consisting of a TiO phase (Class I interface) and an outer zone of Ti_3Al [Tressler, 1973; Wang, 1993]. The growth of the reaction zone was found to follow a parabolic rate law and that aluminum diffusion through the reaction zone was the rate determining step.

The alloying effects of the fiber coating materials and the NiAl matrix has been summarized in section 2.3.1.3. Assuming that the titanium coating and the NiAl matrix behave as a diffusion couple, the diffusion depth, x, of titanium atoms into the NiAl matrix can be estimated using Equation 4-6 with $D = 1 \times 10^{-10}$ cm^2/s and a time of one hour (this time is substantially less than the diffusion bonding time, but should be adequate for an order of magnitude calculation). Using these values a diffusion distance is found to be 12 μm. The titanium diffusion into the NiAl lattice gives rise to an additional degree of order in which the Al and Ti atoms occupy ordered sites on the aluminum sublattice [Stoloff, 1984]. The resulting Ni_2AlTi Heusler phase (β'), which has better creep resistant properties than NiAl, may form a two phase alloy of NiAl (β) and β' at the fiber matrix interface. This interphase region would be expected to exhibit an appreciably greater resistance to creep than NiAl since the interactions of dislocations with semicoherent interfaces and an intrinsically different glide behavior of the two phases will involve processes that severely reduce the overall dislocation mobility. Though the solubility of titanium in NiAl can be appreciable (~10 at.%) at high temperatures (>1100 K), the solubility is limited to ~1 at. % at ambient temperatures and precipitation is expected when the compositions exceed this value.

The nickel-Al_2O_3 combination has a lower thermodynamic driving force for reaction than the titanium-Al_2O_3 system, but still a significant reaction occurred as evidenced by the change in fiber surface morphology shown in Figure 37. The most probable reaction product is the nickel aluminate spinel ($NiAl_2O_4$) which forms a ternary oxide (Class II interface) at the interface between Ni and α-Al_2O_3 [Williams, 1993; Draper, 1994; Asthana, 1995]. Though the nickel-Al_2O_3 reaction is relatively well understood, the effect of the spinel interphase on the mechanical integrity of the Ni-Al_2O_3 interface is not [Wasynczuk, 1987]. Some investigators claim that spinel formation leads to strong interfaces [Klomp, 1985; Ohuchi, 1991], whereas others consider it to have a weakening effect [Williams, 1993; Draper, 1994]. The discrepancies between these studies indicates that different processing parameters and testing configurations lead to disparate results.

When compositing NiAl with nickel-coated fibers, the nickel atoms simply dissolve into the matrix and occupy aluminum lattice sites. The Ni-Al phase diagram indicates a wide β phase field which can accommodate up to 60 at.% nickel. The relatively small composition change at the interface is not expected to alter the mechanical properties of the matrix since the dependence of the yield stress and hardening rate for compositions near stoichiometry are weak [Noebe, 1993].

In most ceramic-metal systems only a few metals can bond to ceramics without forming extended reaction layers at the interface. The Nb-Al_2O_3 system is one of the few that serve as a model system [Howe, 1993; Petrich, 1993]. In this case, the reduction-oxidation reaction results in the dissolution of both the O (interstitially) and Al (subtitutionally) into the niobium, forming a solid solution of niobium with oxygen and aluminum, but no reaction products [Ohuchi and Kohyama, 1991]. This Class IV interface, thus produces a very narrow (one to two monolayers thick) fiber-niobium interface. The dissolution of the oxygen into the niobium serves as a potent solid solution strengthener. At high temperatures the solubility of niobium in NiAl approaches 10-at.%, but at room temperatures the solubility is generally less than 2-at.%. Dissolution of the niobium into NiAl produces a Laves phase (NiAlNb) with stress exponents in the 2-4 range.

4.6 Oxidation Behavior and Interfacial Characterization of NiAl-Saphikon Composites

4.6.1 Results of NiAl-Saphikon Composites Thermally Cycled Between 373 K and 1173 K

Figure 253 shows the fracture surface of a NiAl composite with (a) exposed and (b) embedded fibers cycled to 1173 K for 1000 cycles. The NiAl-Saphikon composites did not exhibit any fiber-matrix interface oxidation, but did exhibit extensive growth of oxide needles on the grain boundaries. The oxide needle protrusions are more clearly seen in Figure 45 to extend outward from the grains. This oxide scale morphology is frequently observed in NiAl and is attributed to either θ- or δ-Al_2O_3 metastable oxides [Doychak, 1989]. No dense oxide morphologies characteristic of α-Al_2O_3 were observed. (Note that no electroetched specimens were investigated in this temperature regime.) Because no interfacial oxidation occurred or mature oxide phases in this temperature regime, the maximum thermal cycling temperature was increased to 1423 K.

4.6.2 NiAl-Saphikon Composites Thermally Cycled 75, 150, and 300 Times Between 373 and 1423 K

4.6.2.1 Composites with Exposed Fiber Ends

Figure 46 shows a SEM micrograph of an uncoated exposed fiber thermally cycled 75 times. Continuous, thick (>1 μm), and adherent oxide scales have formed (A) at the matrix-fiber triple points, while other regions have scales partially wrapped around the fiber circumference and then extending down the length of the fiber (**B**). The micrograph also shows that the fiber surface has some large gouges or pitted regions scattered on the surface. The origin of the gouges is unknown, but may be generated either during the initial stages of the consolidation process or by the oxide scale generating surface stresses which cause chipping of the fiber surface. Furthermore, this micrograph indicates that the etchant does not attack the fiber surface since etch pits were not observed. As shown by the SEM micrograph in Figure 48, similar oxide scale formations were seen in the nickel-coated fiber surface (**A**), and the fiber surface morphology is uniformly rough when compared to the surface of the uncoated fiber shown in Figure 47.

Figure 49a shows an SEM micrograph of an exposed titanium-coated fiber thermally cycled 75 times. Similar to the uncoated fiber, the titanium-coated fiber shows localized oxide formation along the matrix-fiber triple points (**A**) and scale growth along the circumference of the fiber (**B**). Figure 49b is a higher magnification SEM micrograph that shows a rough fiber surface morphology decorated with submicron pits and a general tendency of the roughness features oriented along the c-axis of the fiber. A rough surface morphology is expected because of the high-temperature titanium-Al_2O_3 chemical reaction described in Table 11; however, some features, may be an artifact of the etchant attacking the Ti-Al_2O_3 reaction products. The increased fiber surface roughness combined with Ti-Al_2O_3 and Ti-NiAl chemical reactions should promote fiber-matrix adhesion.

Increasing the number of thermal cycles to 150 produces oxide scale development on the circumference of the fiber end (**A**) as shown by the SEM micrograph of a titanium-coated fiber in Figure 50a. In addition, a band of oxide scale (**B**) bridging the scales formed along the matrix-fiber triple points. The EDX spectrum plotted in Figure 50b obtained from the fiber surface indicates a strong titanium signal at 4.5 keV along with the aluminum and oxygen signals at 1.49 keV and 0.52 keV, respectively.

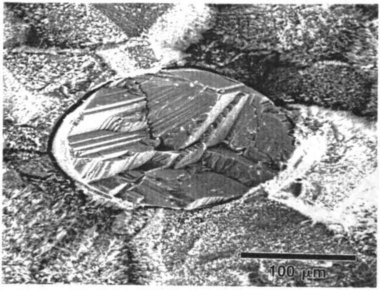

Figure 45 SEM micrograph of a thermally-cycled NiAl-Saphikon fractured composite.

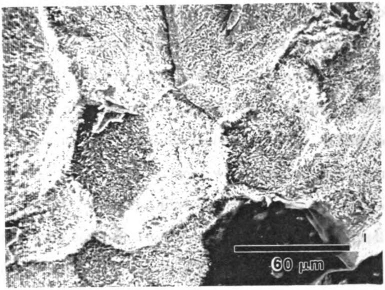

(a)

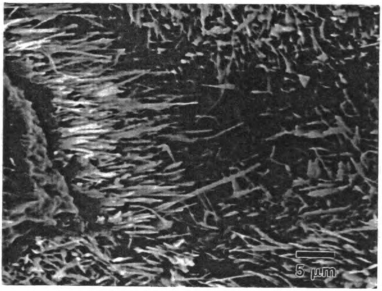

(b)

Figure 46 SEM micrographs of an uncoated NiAl-Saphikon fracture surface.

This indicates that some of the titanium remains localized at the fiber-matrix interface after 150 cycles. Qualitatively similar oxide scale development was also observed for the uncoated and nickel-coated fibers as illustrated by the SEM micrograph of the nickel-coated fiber in Figure 51. Due to the extensive amount of interfacial oxidation for the exposed fiber end composites, thermal cycling was terminated after reaching 150 cycles.

4.6.2.2 Composites with Completely Embedded Fibers Embedded fiber composites, thermally cycled 75 and 150 times, were examined and, in general, no interfacial oxide scale was found. The SEM micrograph in Figure 52 shows a small amount of oxide scale formation on a nickel-coated fiber. Since this was the only oxide seen on any of the fibers tested, it is assumed that it resulted because of incomplete consolidation. An SEM micrograph of an embedded titanium-coated fiber surface thermally cycled 150 times is shown in Figure 53 and, though no oxide scales were present, titanium-rich areas exist at the triple point region (A). Examination of composites thermally cycled 300 times did not reveal any oxide scale formation. These results indicate that embedded fibers are sufficiently protected from oxidation processes.

Another aspect of the thermally cycled composites investigated was the fiber surface morphology after undergoing 300 cycles. The surface morphology of an uncoated fiber is shown by the micrographs in Figure 54. These micrographs indicate surface undulations, some gouging (left side of the fiber) and, in general, a rougher appearance than the surface morphology of the exposed fiber end shown in Figure 47. The SEM micrographs shown in Figure 55 illustrate the rough surface morphology of a titanium-coated fiber thermally cycled 300 times. Comparing this with the surface morphology of the exposed titanium-coated fiber end shown in Figure 50a several differences are seen.

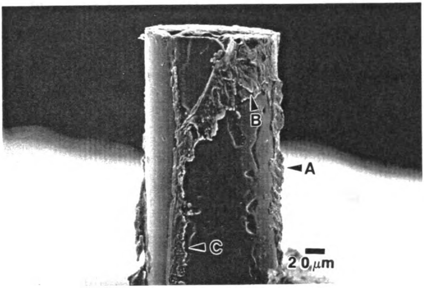

Figure 47 A SEM micrograph of an exposed uncoated fiber thermally cycled 75 times.

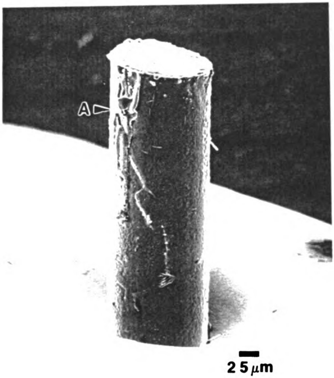

Figure 48 A SEM micrograph of an exposed Ni-coated fiber thermally cycled 75 times.

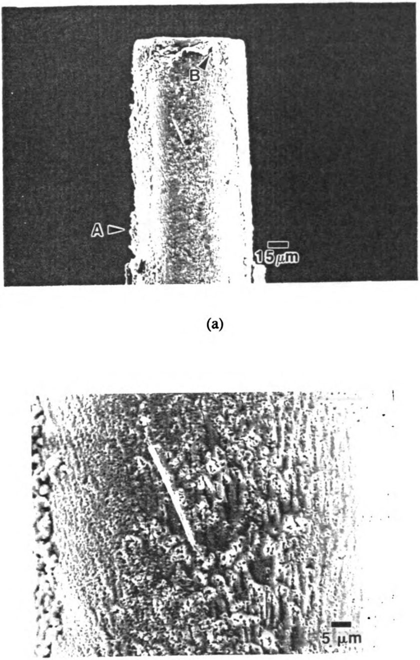

(a)

(b)

Figure 49 SEM micrograph of exposed Ti-coated fiber thermally cycled 75 times.

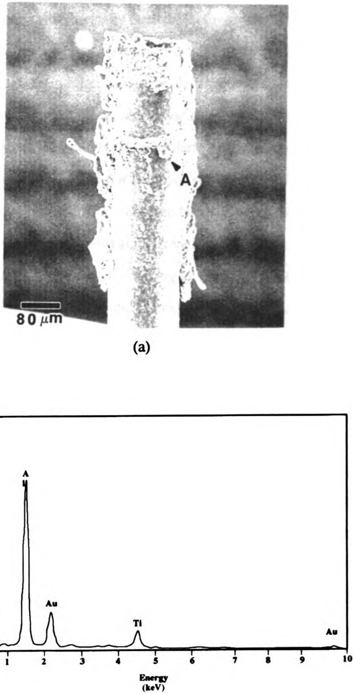

Figure 50 (a) A SEM micrograph and (b) a EDX spectrum of a Ti-coated fiber.

To assist in determining the possible oxygen routes to the fiber-matrix interface of embedded fibers, a composite thermally cycled 300 times was fractured and examined. Figure 56 is a SEM fractograph of the interface and grain boundary regions of an uncoated fiber. Though no interfacial oxide scale is present, extensive grain boundary oxidation (identified by the whisker formation) indicates that oxygen diffusional paths are present at the grain boundaries during thermal cycling.

4.6.3 Discussion of the Oxidation Behavior of Thermally Cycled NiAl-Saphikon Composites The above results indicate that the two thermal cycling temperature regimes produced different oxide scales at different locations in the exposed fiber composites. For instance, after thermally cycling to 1173 K for 250 hours, the NiAl-Saphikon exposed-end fiber specimens did not exhibit any fiber-matrix interfaceoxidation. Only metastable δ-Al_2O_3 and θ-Al_2O_3 oxide scales lining the grain boundaries were observed in this temperature regime. The 1173 K thermal cycling experiments indicate that exposing NiAl-Saphikon composites to these temperatures for 250 hours is not sufficient to cause α-Al_2O_3 formation either at the grain boundaries or the interface. Also, the presence of metastable intergranular oxide scales suggest that oxygen diffusion along the grain boundaries is relatively rapid. These results are consistent with other observations reporting that metastable oxide scales transform to α-Al_2O_3 after an incubation period that is dependent on time, temperature, and other oxidation variables (percent of oxygen in the atmosphere). As an example, Doychak et al. observed only α-Al_2O_3 when oxidizing NiAl single crystals at 1373 K for 1 hour, but θ-Al_2O_3 for 0.5 h at 1373 K [Doychak, 1989].

Increasing the maximum cycling temperature by 250 K to 1423 K, while decreasing the total soak time, produced dramatic differences in the interfacial oxidation behavior. In particular, mature α-Al_2O_3 interfacial oxidation forms in composites with exposed fiber ends. Grain boundary oxide scales seem to be absent or at least show no maturation. To provide some physical insight into the interfacial oxidation process, the

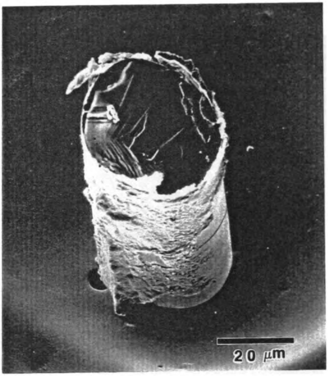

Figure 51 A SEM micrograph of an exposed Ni-coated fiber thermally cycled 150 times.

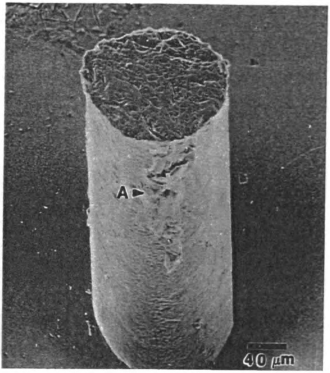

Figure 52 A SEM micrograph of a Ni-coated fiber thermally cycled 150 times.

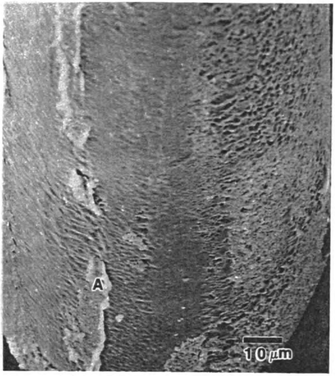

Figure 53 A SEM micrograph of a Ti-coated fiber thermally cycled 150 times.

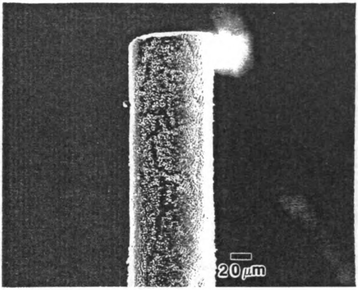

(a)

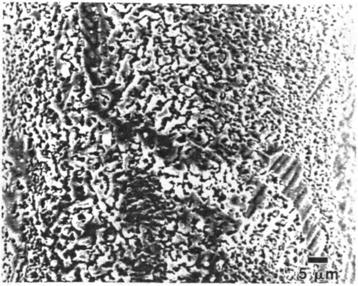

(b)

Figure 54 SEM micrographs of an uncoated fiber thermally cycled 300 times.

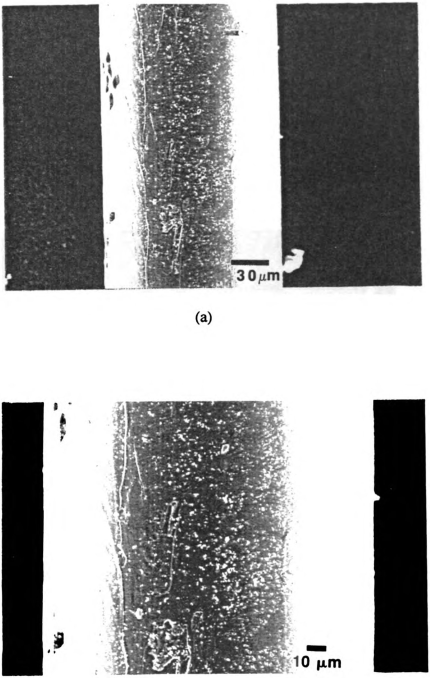

(a)

(b)

Figure 55 SEM micrographs of a Ti-coated fiber thermally cycled 300 times.

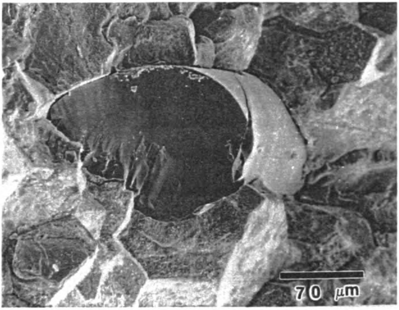

Figure 56 A SEM fractograph of a uncoated embedded fiber thermally cycled 300 times.

schematic shown in Figure 58 shows a likely sequence of events that occurred during one thermal cycle [Doychak, 1992].

Due to the CTE mismatch between NiAl and Al_2O_3, the matrix expands during specimen heating to a greater extent (~6.5%) than the fibers. The fiber-matrix adhesion is incapable of sufficiently constraining matrix expansion, therefore a cylinder of matrix is exposed to the oxidizing environment, and an oxide scale is formed. During cooldown, the matrix wants to contract back to its original position, but the cylinder of newly-formed oxide impedes the replacement. Providing the oxidized matrix can slide back around the fiber, the oxide acts as a wedge, putting the matrix in tension and causing crack propagation along the interface.

Though only a small number of thermal cycles were performed, it is clear that composites with uncoated or coated fibers exposed directly to the environment quickly form interfacial oxide scales. Thus, though the fiber coatings may enhance fiber-matrix adhesion, the increase is not sufficient enough to overcome the oxidation processes associated with the differential strains and the interfacial imperfections (e.g., grain boundaries, voids, etc.). Examination of the fiber surface morphology after thermal cycling seems to suggest that wear occurs during the thermal excursions.

4.7 Assessment of Consolidation Induced Fiber Damage for Uncoated and Coated Saphikon Fibers

4.7.1 SEM Fractographic Study of Extracted-Fiber Fragments The SEM fractograph of an uncoated fiber fragment shown in Figure 59a indicates that the fracture initiated at the fiber surface (denoted by the arrow). Extensive examination of fiber fragments failed to reveal preferential crack initiation at the grain boundary ridges or the pores. In all cases, the rhombohedral planes, $\{\bar{1}012\}$, were the primary cleavage plane and rarely was basal plane, {0001} cleavage observed.

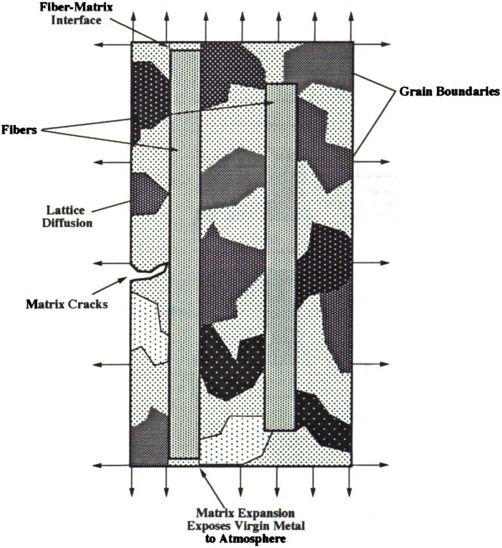

Figure 57 A schematic illustrating the possible oxygen diffusion paths in composites.

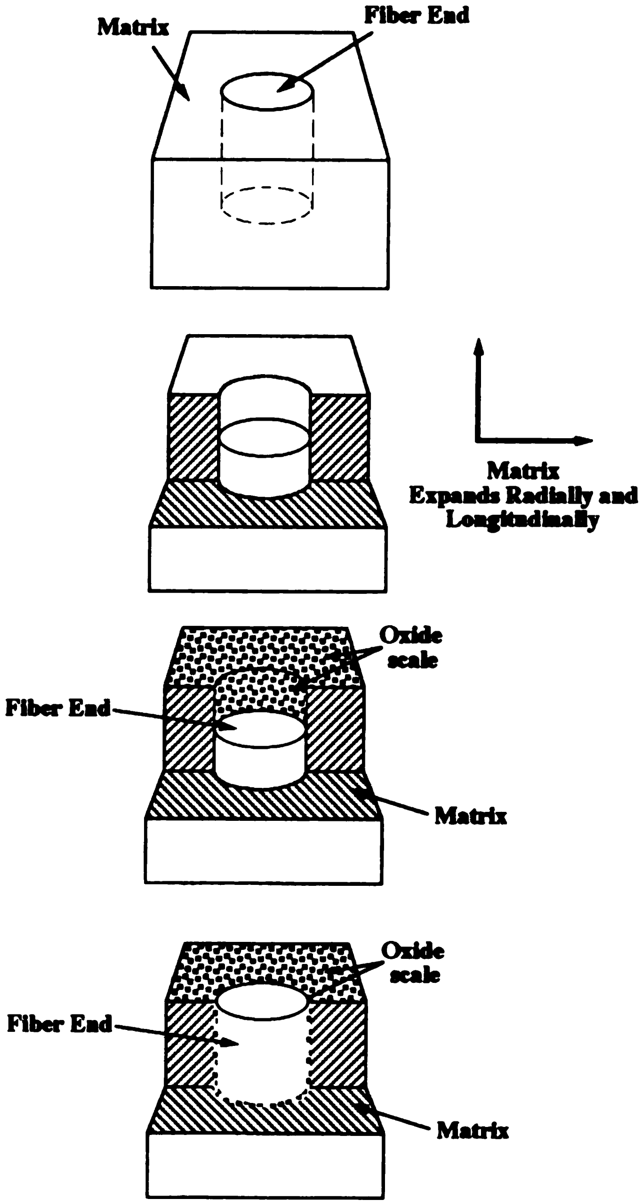

Figure 58 A schematic of oxide scale formation in composites with fiber ends exposed.

Figure 59b and c show SEM fractographs of niobium-coated fibers. In general, as shown in Figure 59b, the fracture cleavage originated at the fiber surface and propagated along rhombohedral planes in a manner similar to that observed for the uncoated fibers. Occasionally, a combination of basal and rhombohedral cleavage fracture occurred as shown by the SEM fractograph in Figure 59c. Though fiber facetting resulted in acute edges along the fiber length, these areas did not appear to be preferred crack initiation sites.

Figure 59d and e are SEM fractographs of extracted nickel- and titanium-coated fibers, respectively. Similar to the uncoated and niobium-coated fibers, the fracture initiation sites occur on the fiber surface. Furthermore, longitudinal cracks along the c-axis were occasionally seen.

The propensity for rhombohedral cleavage, combined with identification of the basal plane as the easy-cleavage plane above 973 K [Iwasa, 1984], suggests that fracture propagation occurs during a low temperature segment of the consolidation process. Two possible causes of low temperature fracture propagation are the presence of large residual radial and hoop compressive stresses (~100 MPa), and large tensile axial stresses (~100 MPa), arising during the cool down segment [Bowman, 1994]. Another factor, which may produce bending stresses at low and high temperatures and, hence, promote fiber fracture, is the nonuniform loading of the composite because of platen misalignment or matrix plate machining inaccuracies. The importance of these effects in producing fiber breakage is difficult to estimate, but the bending stress contributions were minimized by following careful experimental procedures.

4.7.2 Extracted-Fiber Fragment Distributions A histogram of the extracted-fiber fragment length distribution is plotted in Figure 60, while a summary of the distribution is presented in Table 14. These data indicate that no full-length fibers survived the consolidation process and that the average extracted-fiber fragment lengths were substantially less than the original 25 mm. Furthermore, ~70% of the fiber lengths

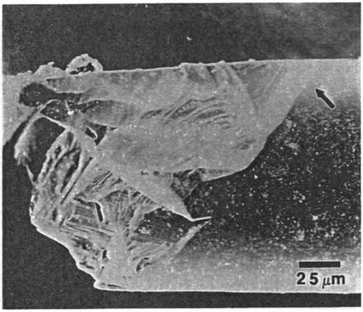

(a)

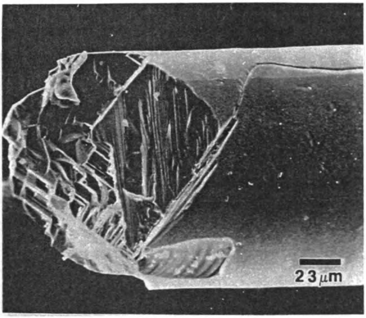

(b)

Figure 59 Fractographs of (a) uncoated, (b) and (c) Nb-, (d) Ni-, and (e) Ti-coated fibers.

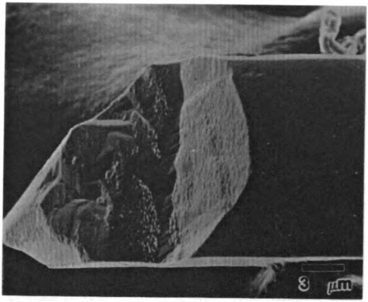

(c)

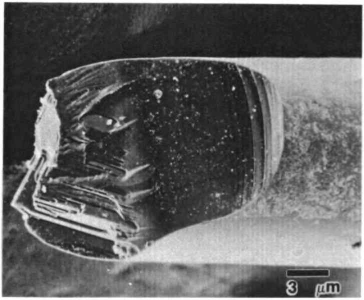

(d)

Figure 59 (cond't).

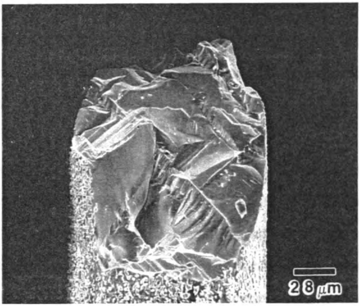

(e)

Figure 59 (con't.).

for the nickel- and titanium-coated fibers were in the 0-5 mm range, compared to ~35% -40% for the uncoated and niobium coated fibers, respectively. Also, only 5% of the nickel- and titanium-coated fibers were longer than 10 mm, while ~ 30% of the uncoated and niobium-coated fibers fragments were found in this range. Examination of Table 14 identifies two fiber fragment distributions. The first distribution consists of uncoated and niobium-coated fibers having approximately equal numbers of short, intermediate, and long fragments. This distribution is represented by weak interfacial chemical reactions and no reaction product formation. The second distribution represents the more reactive nickel and titanium fiber coatings which tends to produce a gradual increase in the number of fiber fragments with decreasing lengths as the fiber fragment length decreases.

Clear correlations between fiber surface parameters and composite strength, modulus, or toughness are difficult to obtain, but fiber-matrix chemical reactions generally affect the composite mechanical response in two ways. First, increasing the surface flaw population of inherently brittle material such as Al_2O_3 decreases the fiber statistical strength [Curtin, 1991]. Secondly, fiber damage during the consolidation process reduces the fiber aspect ratio, l/d (fragment length / fiber diameter) which decreases the effectiveness of the fiber-matrix load transfer.

One approach of assessing the effect of fiber surface damage on the tensile strength of the fiber is provided by using

$$\sigma_f^* = \left(\frac{1}{1.12}\right)\left(\frac{E_f G_c^*}{\pi c}\right)^{\frac{1}{2}}, \qquad 4\text{-}8$$

where E_f is the fiber modulus, G_c^* is the strain energy release rate of the fiber, given by $(K_{IC})^2/E_f$, and c is the flaw size [Ochiai, 1981; Ochiai, 1988]. Using the average extracted-fiber strengths of 1.2 and 1.6 GPa reported by Draper and Locci and a critical stress intensity factor, K_{IC}, for the rhombohedral fracture of 2.38 MPa-m$^{0.5}$, the critical

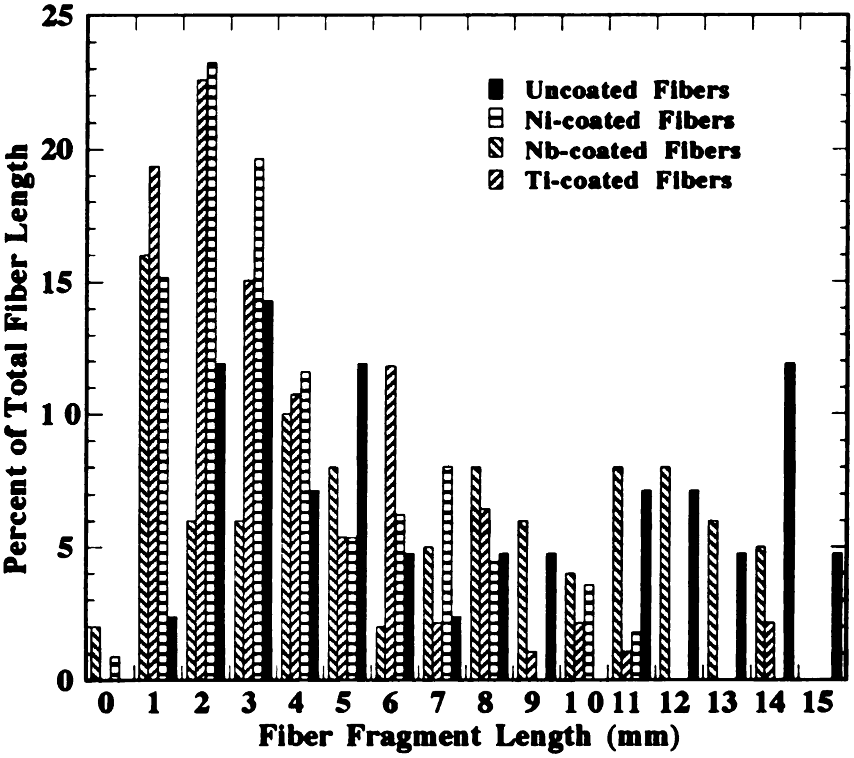

Figure 60 Histogram of the extracted-fiber length distribution.

flaw size for fiber failure at the measured strength is found to range from 0.9 μm to 0.4 μm [Draper, 1994; Iwasa, 1984]. The analysis of the fiber surface morphologies indicates that the majority of the coated fiber surface flaws are on the order of or less than these values. This observation suggests that the coated fibers have an in situ strength less than 1.2 GPa which is ~50% decrease from the reported as-received fiber strength of 2.4 GPa [Draper, 1994].

4.7.3 Correlation Between the Fiber Fragment Distributions and the Composite Strengthening Ability The next concern is to determine how effective the fragmented (both coated and uncoated) fibers are in transferring load when compared to the original continuous state. To evaluate this, a critical fiber length, l_c, was calculated using [Broutmann, 1967]

$$\frac{l_c}{d_f} = \frac{\sigma_f}{2\tau} \qquad 4\text{-}9$$

where d_f is the fiber diameter (~130 μm), σ_f is the fiber fracture stress, and τ is the matrix shear stress (τ_{ys}) or interfacial bond strength (whichever is lower). The value used for τ is crucial because interfacial debonding occurs if the interfacial shear stress reaches the debond stress before either matrix yielding or fiber fracture occurs. If it is assumed that τ_{ys} equals half the tensile yield stress, then τ_{ys} for the NiAl matrix is ~60 MPa at room temperature and will be even lower at higher temperatures. Using an extracted fiber strength of 1.5 GPa (~ 50% room temperature fiber strength), results in a predicted fiber critical length of 1.6 mm. From Figure 256, ~82 % of the fiber fragments are greater than 2 mm, suggesting, that for all coatings, many fibers can effectively contribute to the composite strength.

Table 13 Summary of extracted-fiber fragment distributions.

Fiber Fragment Length (mm)	Percent of Total Fiber Fragments			
	Uncoated	Nickel-coated	Titanium-coated	Niobium-coated
0 - 5	35.5	70.0	62.0	40.0
6 - 10	28.0	23.0	26.0	32.0
10-15	35.0	5.0	5.0	28.0
Avg. Fiber Fragment Length (mm)	8.01 ± 4.5	4.38 ± 2.54	3.63 ± 2.86	6.79 ± 5.83

The effects of the fiber lengths on the composite strength is given by (assuming perfect fiber-matrix bonding) [Chawla, 1987]

$$\sigma_c = \left(1 - \frac{l_c}{2l}\right)\sigma_f V_f + \sigma_m (1 - V_f). \qquad 4\text{-}10$$

Using the average fiber lengths listed in Table 14, a fiber critical length of 2 mm, a 7% volume fraction, a NiAl flow stress of 160 MPa, and a 347 MPa for a continuously reinforced composite, the percent strengthening capabilities of composites with consolidation induced fiber breakage are listed in Table 15. These values indicate that the uncoated, nickel-coated, and niobium-coated fiber composites will have 90% or more of the strengthening capability of the continuos fiber composite, while the titanium-coated fiber with an average fragment length of 3.6 mm was 87%. Decreasing the average fiber length 50% and then 100% shows a significant degradation in the strengthening ability of the nickel- and titanium-coated composites.

Table 14 Calculated percent strengthening capability for fragmented fiber lengths.

(Avg. Fragment Length) / f	Uncoated	Nickel-Coated	Titanium-Coated	Niobium-Coated
f = 1	95	90	87	94
f = 2	88	76	70	86
f = 4	73	48	36	68

Alterations in the composite mechanical properties due to consolidation induced fiber aspect ratio changes can be also analyzed using the frequency of fiber fragments vs. the fiber aspect ratio shown in Figure 61 and summarized in Table 16. The generally accepted guideline for achieving rule of mixture predictions requires the fibers to have an aspect ratio of at least 25 [Clyne, 1993]. Table 15 shows that approximately 75% of the uncoated fiber fragments and 65 % of the niobium-coated fiber fragments have an aspect ratio greater than 25, while the nickel- and titanium-coated fibers show only 50% of the fragments having an aspect ratio greater than 25. Assuming perfect fiber-matrix bonding, this result suggests that composites fabricated with uncoated and niobium coated fibers should show slight deviations from ROM predictions, while almost one-half of the nickel- and titanium-coated fiber fragments may not be fully loaded and, consequently, may not strengthen the matrix as effectively as niobium coated fibers.

4.8 Fracture Behavior of NiAl-Saphikon Composites

4.8.1 Room-Temperature Composite Fracture Behavior Room temperature fracture specimens of NiAl-FP and NiAl-Saphikon composites were investigated using scanning electron microscopy. Figure 62a and 4-62b shows the brittle fracture surface of NiAl-(uncoated-FP) and NiAl-(Ni-FP) composite, respectively. The fiber-matrix interfaces surrounding both types of fibers appear cohesive and no distinctions between coated and uncoated fibers are apparent.

The SEM fractograph in Figure 63 shows the room temperature fracture surface of a 7 vol.% NiAl-(uncoated-Saphikon) composite dilatometry specimen thermally cycled 3 times from room temperature to 1460 K. In general, the brittle fracture surface showing transgranular cleavage corresponds to that for a typical bcc metal. Also, the fiber-matrix interfaces appear cohesive, and no interfacial gapping is present. Further investigation of the fracture surface is shown in Figure 64a and illustrates an interface along a longitudinal section of the fiber. The fiber surface appears relatively smooth.

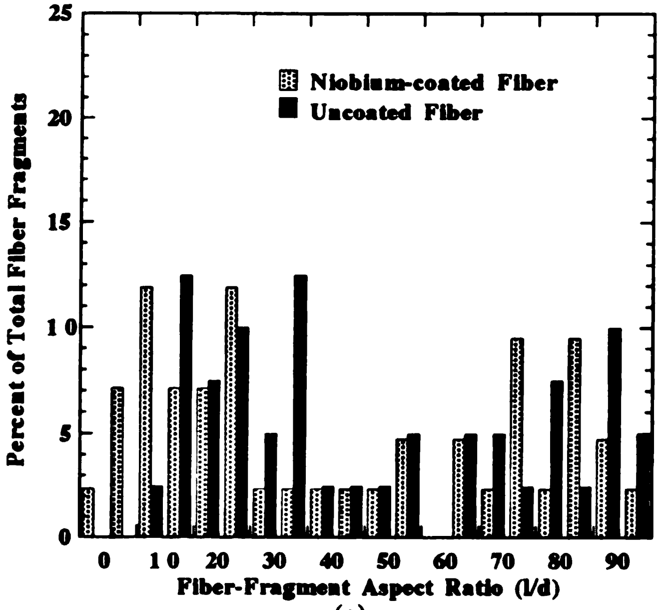

(a)

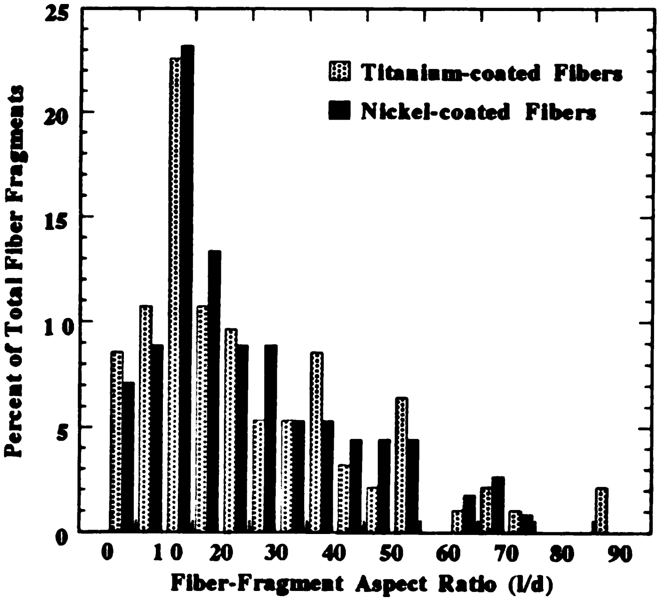

(b)

Figure 61 Percentage of the number of fiber fragments vs. the fiber fragment aspect ratio.

Table 15 Summary of extracted fiber fragment aspect ratios.

Fiber Fragment Aspect Ratio (l/d)	Percent of Total Fiber Fragments			
	Uncoated	Nickel-coated	Titanium-coated	Niobium-coated
0 - 24	22.5	52.7	52.4	35.7
25 - 49	32.5	33.1	32.3	21.4
50 - 74	17.5	13.3	11.8	14.4
75 - 100	27.5	0.9	3.5	28.5
Avg. Aspect Ratio	53.4 ± 30	29.2 ± 19	29.8 ± 22	45.3 ± 25

The high magnification fractograph of a fiber-matrix interface in Figure 64b shows a small interfacial void (**A**), but otherwise, intimate contact between the fiber and matrix is apparent. The angular step morphology indicates that brittle cleavage fracture occurred near the interface, though a small amount of quasi-cleavage, with tear ridges, is seen at **B**. Occasionally, grain boundary oxidation, identified by a continuous rough surface morphology, was seen on grains located near the edge of the composite.

The fracture surface of a 7-vol.% dilatometry specimen composited with niobium-coated Saphikon fibers and thermally cycled 4 times from room temperature to 1450 K is shown in the SEM micrograph of Figure 65. Transgranular brittle cleavage fracture is clearly evident (**A**). The absence of matrix plate interfaces indicates that complete consolidation of the matrix plates occurred. Also shown in this micrograph is grain boundary oxidation (**B**). Figure 66a shows a rough fiber-channel surface morphology oriented parallel to the fiber axis. A closer inspection of the fiber-matrix interface is shown in Figure 66b and illustrates intimate contact between the fiber and the matrix. In addition, the matrix material next to the fiber is devoid of cleavage steps and appears to consist of slip lines oriented at approximately 45° to each other (**A**). EDX analysis of the interfacial region gave a strong niobium signal, verifying the presence of the coating material after four thermal cycles.

Figure 67 is a SEM micrograph of a fiber-matrix interfacial region from a 7-vol.% NiAl-(Ni-Saphikon) composite, thermally cycled from room temperature to approximately 1423 K for four cycles and then fractured. The micrograph shows intimate fiber-matrix contact and slight evidence of radial cracking (**A**). There is also a small amount of oxide scale present near the interface (**B**). Figure 68a and b are SEM micrographs of the interface along a longitudinal section of a fiber. The left-hand side of the micrograph shows matrix material (**A**) and a small ridge of matrix material (**B**) adhering to the fiber surface. The right-hand side of the micrograph shows the formation of a mature oxide scale (appears to be a dense alumina and not a metastable oxide) on a

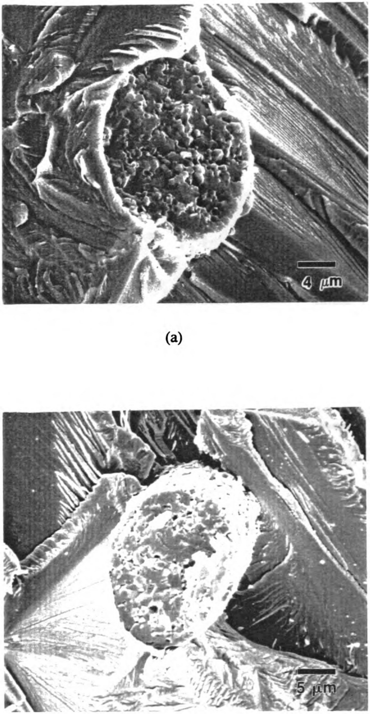

(a)

(b)

Figure 62 SEM micrographs of (a) uncoated and (b) Ni-coated NiAl-FP composites.

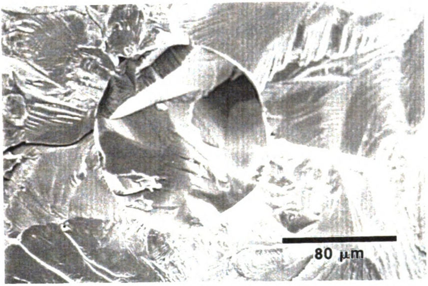

Figure 63 SEM fractograph of a 7-vol.% uncoated Saphikon composite.

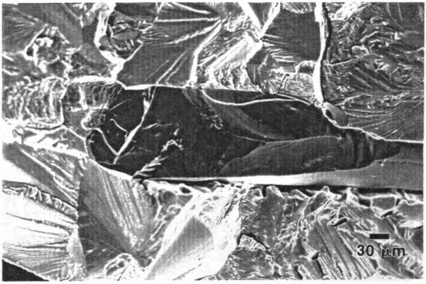

(a)

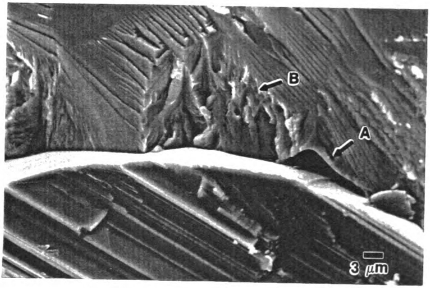

(b)

Figure 64 SEM fractographs of a 7 vol.% NiAl-(uncoated-Saphikon) composite.

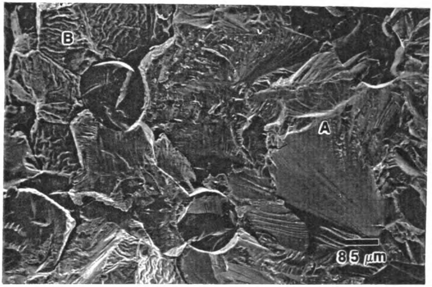

Figure 65 A SEM fractograph of a 7-vol.% NiAl-(Nb-Saphikon) composite.

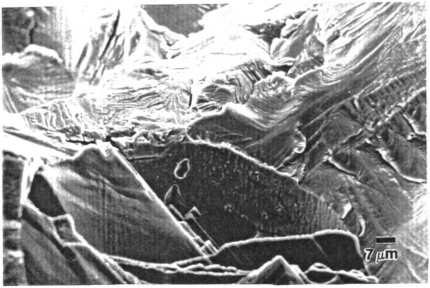

(a)

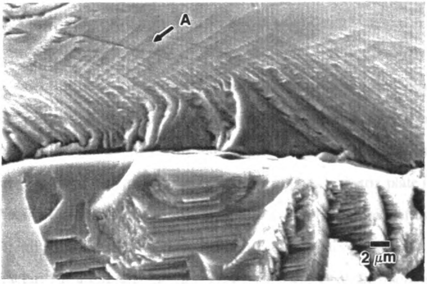

(b)

Figure 66 SEM fractographs of a Nb-coated Saphikon fiber composite.

grain boundary (C). A high magnification view of the fiber surface is shown in Figure 68b. The dimpled surface morphology was not present in the previous investigations of fiber surface morphology, but presumably are the result of fiber-nickel coating reactions that occur during the consolidation of the composite.

Qualitative information about the interfacial mechanical behavior information is shown in Figure 69, where a room-temperature fracture surface of a titanium-coated Saphikon fiber composite reveals a brittle interphase, as evidenced by the numerous small cracks, labeled '**A**'. Furthermore, the intimate fiber-matrix contact suggests a strong interfacial bond. The interphase region shown was ~5 µm thick, well beyond the distance of the x-ray signal, before cleavage fracture occurred (**B**). Figure 69 illustrates the roughness of the fiber trough for a fractured titanium-coated Saphikon fiber dilatometry composite thermally cycled two times. In this specimen no grain boundary oxidation was observed on the fracture surface.

4.8.2 High-Temperature Composite Fracture Behavior Figure 70a shows an SEM fractograph of a NiAl-(uncoated Saphikon) dilatometry specimen thermally cycled 4 times and fractured at ~750 K. In general, the matrix exhibited transgranular brittle cleavage fracture with most fiber-matrix interfaces appearing cohesive, though occasionally voided regions (**A**), presumably originating, from incomplete consolidation, are seen. These voided regions act as stress raisers upon thermal loading and may accelerate fiber-matrix decohesion. Furthermore, interfiber matrix cracking with a path along the mating region of the middle matrix plate and an outside matrix plate is evident (**B**). Figure 70b is a SEM fractograph or the fiber-matrix interfacial region illustrating a large circumferential crack and gapping around the fiber. Contrary to the room temperature fracture surface results shown in Figure 64, a survey of the fracture surfaces did no reveal any grain boundary oxidation.

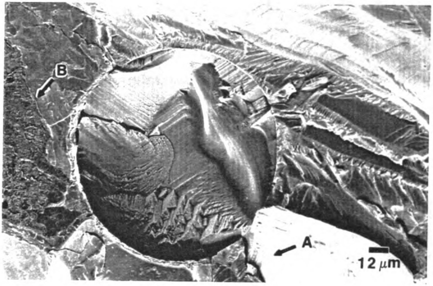

Figure 67 A SEM fractograph of a 7-vol.% NiAl-(Ni-Saphikon) composite.

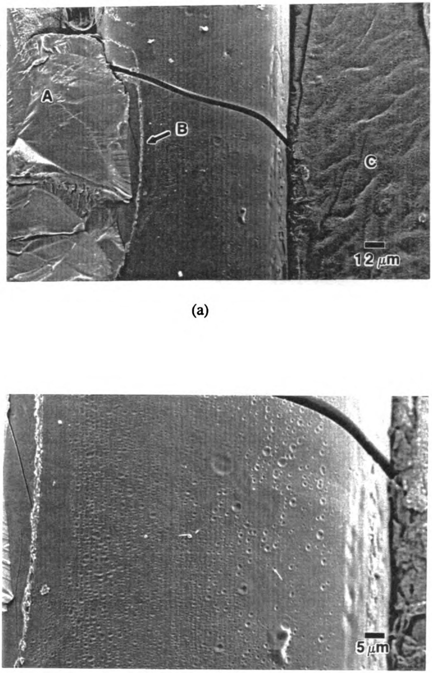

(a)

(b)

Figure 68 SEM micrographs of a 7 vol.% NiAl-(Ni-Saphikon) composite.

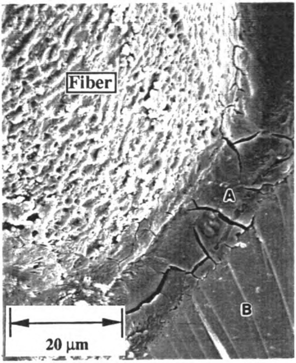

Figure 69 SEM micrograph of a Ti-coated Saphikon fiber composite.

Figure 71 shows both high and low magnification SEM fractograph of a 7-vol.% NiAl-(Nb-Saphikon) dilatometry specimen thermally cycled 8 times. Most of the micrograph (**A**) indicates transgranular fracture similar to that seen in the previous micrographs, while the left-center part (**B**) indicates intergranular brittle fracture. The intergranular fracture is a result of oxidation embrittling the grain boundaries, providing easy crack propagation through the composite. Though grain boundary oxidation was seen, oxidation through the thickness of the composite was never observed. The micrograph of a fiber in the region without oxidation shows a small amount of fiber-matrix interfacial decohesion, but other fibers seem to be bonded well enough to fail when the matrix failed. In general, the composite displays a well bonded fiber-matrix interface, with a transgranular fracture surface. In the high magnification micrograph shown in Figure 71b the fiber-matrix interface shows good fiber-matrix adhesion, though one small void is present at the point marked '**A**'.

The fracture surface of a 7 vol.% NiAl-(Ni-Saphikon) dilatometry composite thermally cycled 3 times to ~1473 K is shown by the SEM micrographs in Figure 72. The fiber ends, which were flush with the fracture surface, indicate a large amount of fiber-matrix adhesion existed and resulted in little fiber pull-out (though fiber ends extending beyond the matrix may shatter during composite fracture). Figure 72b shows an isolated fiber surrounded by unoxidized (**A**) and oxidized (**B**) regions, with a crack through a nearby oxidized grain to the fiber-matrix interface. A closer examination of the fiber surface and trough is shown in the micrograph of Figure 72c. This micrograph shows a rough fiber surface and dimple imprints in the fiber trough. The top region of the fiber shows some interfacial gapping (**A**), while Figure 72d shows an unidentified interfacial phase (**A**) and its relation to the fiber surface contours. Numerous attempts at determining the type of phase using EDX analysis failed due to the height of the regions surrounding the interface.

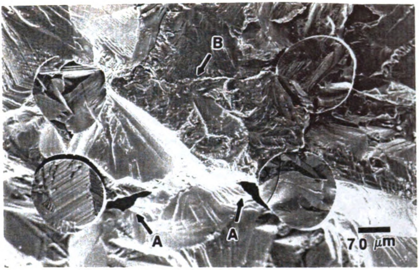

(a)

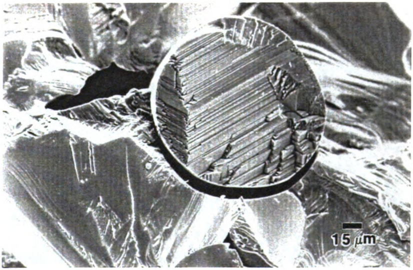

(b)

Figure 70 SEM fractographs of a uncoated Saphikon-NiAl composite.

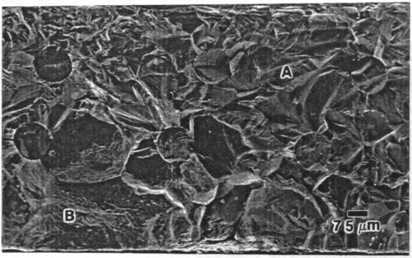

(a)

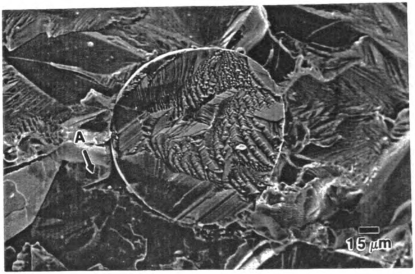

(b)

Figure 71 SEM micrographs of a NiAl-(Nb-Saphikon) composite.

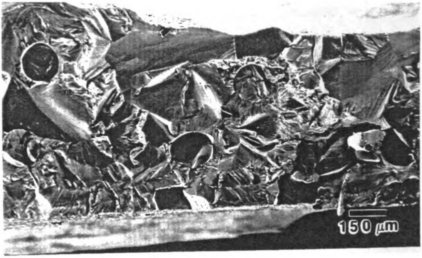

(a)

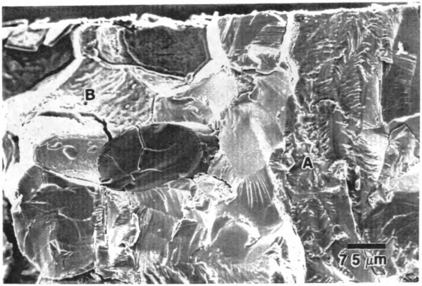

(b)

Figure 72 SEM fractographs of a Ni-coated Saphikon-NiAl composite.

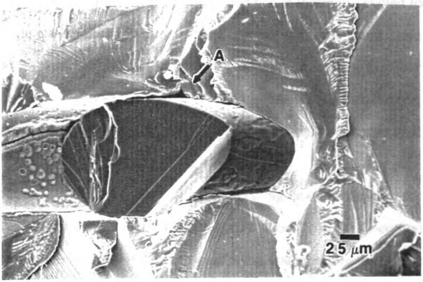

(c)

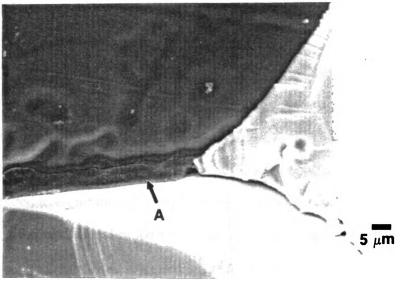

(d)

Figure 72 (con't).

Similar fracture surface behavior is seen in the SEM micrographs shown in Figure 73, of a 5 vol.% NiAl-(Ti-Saphikon) dilatometry composite thermally cycled four times. A typical brittle transgranular fracture surface is seen, with fiber-matrix interfaces showing intimate adhesion. Figure 73c shows a random roughness of the fiber channel surface morphology. A close examination of the fiber channel surface did not reveal a preferred direction of roughness, suggesting that the roughening did not result from a thermal cycling wear process.

To further understand the effects of thermal cycling on a dilatometric composite, the exterior surface of a 7 vol.% NiAl-(Ni-Saphikon) composite in the as-composited state and thermally cycled 4 times were examined using optically microscopy. No macroscopic cracks are present in the as-consolidated composite shown in Figure 74. After 4 thermal cycles (to maximum temperatures of 1423 K) the grain boundary structure becomes delineated by a, presumed, oxide phase, as shown in Figure 75a (**A**). Furthermore cracks transverse to the fiber direction are also observed in Figure 75b (**A**). These cracks did not appear to penetrate the composite thickness or cause delamination. No cracks parallel to the fiber direction were seen.

4.8.3 Discussion of the Fracture Behavior of Thermally Cycled Dilatometry CompositesAlteration of the interfacial mechanical properties via application of fiber coatings potentially modifies composite fracture toughness in either a positive or negative manner. The fracture surfaces of the thermally cycled composites provides a number of observations related to either the different diffusion bonding process or the effects of the fiber coatings on the mechanical properties of the interface. Consistently observed among the fracture surfaces (both low- and high-temperature) were low energy transgranular cleavage fracture modes. This behavior is common among bcc (or variants of bcc) metals, with the cleavage planes of the {100} type, but sometimes along {110} [Reed-Hill, 1973].

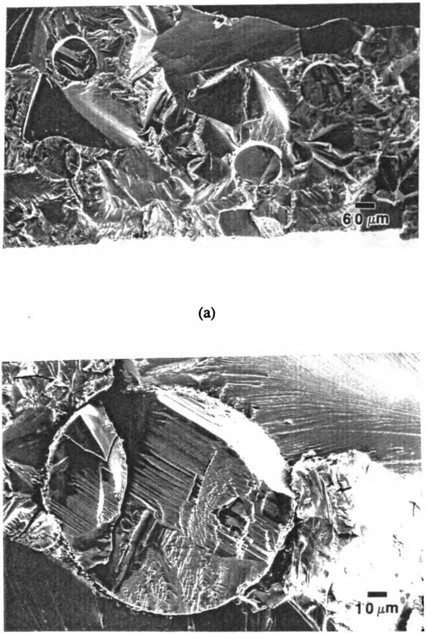

(a)

(b)

Figure 73 SEM fractographs of an 7-vol.% NiAl-(Ti-Saphikon) composite.

(c)

Figure 73 (con't).

Figure 74 Optical micrograph of a 7 vol.% NiAl-(Ni-Saphikon) composite.

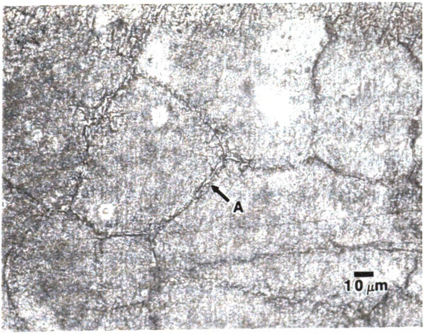

(a)

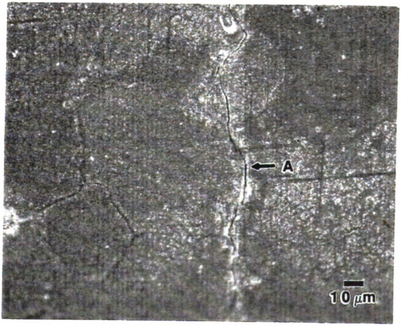

(b)

Figure 75 Optical micrograph of a 7-vol.% NiAl-(Ni-Saphikon) composite after cycling.

The relatively large NiAl grain size, which resulted from the high consolidation temperature and long consolidation time, exacerbates this brittle behavior, since the DBTT increases with grain size [Schulson, 1983]. Since little evidence of ductile fracture was observed, it appears that both temperature regimes were below the DBTT.

Comparing the uncoated and nickel-coated fiber composites showed essentially the same interfacial fracture behavior. Dramatic differences in the fiber roughness were observed, though no indication of surface wear was apparent. In contrast to these results, evidence for changes in the interfacial mechanical properties was observed by investigating the fracture surfaces of titanium-coated fiber composites. As shown in Figure 69, the interfacial region fractures in a distinctively different mode than the NiAl matrix. This observation provides evidence that the titanium coated fiber produces an interphase region with the matrix that possesses different mechanical properties than the matrix. In particular, the numerous cracks in the interphase indicates enhanced brittleness and, perhaps, increased modulus. Since NiAl is brittle at room temperature, the niobium-coated fiber composites is the provided the most promising behavior of the three coating materials, because of the interfacial ductility was increased found

Observations of intergranular oxidation formation was unexpected, since NiAl is generally considered to be highly oxidation resistant. Two factors responsible for this oxidation behavior are the internal matrix stresses, caused by the presence of the fibers, and the strain incompatibilities between adjacent grains. These two effects are coupled, since the thermal stresses generated by the fibers during cooling cause high tensile stresses in the grains and at the grain boundaries. These tensile stresses are difficult to be accommodate, since only three independent slip systems operate, causing microcrack formation. Microcracks formed near the surface of the composite provide fast oxygen diffusion paths, and lead to intergranular oxide formation. As intergranular oxides are nucleated and grow they cause additional stresses at the grain boundaries. Such stresses facilitate nucleation and continuous development of oxides at the grain boundaries.

4.9 Thermal Expansion Behavior of Low-Volume Fraction Composites

4.9.1 Thermal Expansion Behavior of Monolithic NiAl, NiAl-(Saphikon), and NiAl-(Ni-Saphikon) Composites The heating and cooling half-cycle of axial strain versus temperature for monolithic NiAl, plotted in Figure 76, displays the expected behavior of a bulk elastic material. The plot is characterized by the lack of a hysteresis between the heating and cooling curves, and no net residual strain at the end of the complete cycle. A small nonlinear deviation, observed at temperatures above 1450 K, suggests that the small spring force exerted by the actuator caused yielding of the specimen. Though the heating curve is smooth, noise from the frictional resistance between the sample and the quartz tube is apparent in the cooling curve. Figure 77 is a plot of the experimental and theoretical instantaneous CTE versus temperature of the NiAl heating curve. Good agreement between the two is evident.

The plot in Figure 78 is the thermal response of a 7 vol.% NiAl-(Al_2O_3) fiber composite following post-fabrication cooling. The features differentiating this curve from the monolithic case, shown in Figure 76, include a knee (**A**) at ~1178 K in the heating half-cycle, a hysteresis strain between the heating and cooling half-cycles and a knee (**B**) at ~954 K on the cooling half-cycle. These features illustrate the fundamental differences in thermal response between composited and monolithic NiAl.

To facilitate clarity in describing and understanding the above, and the following, thermal strain versus temperature curves, the schematic shown in Figure 79 defines several terms that will be referred to in the remainder of the thesis. From this diagram the heating and cooling half-cycle knees are defined, while two strain values, the hysteresis strain and the residual compressive strain, $\Delta\varepsilon_p$, are identified.

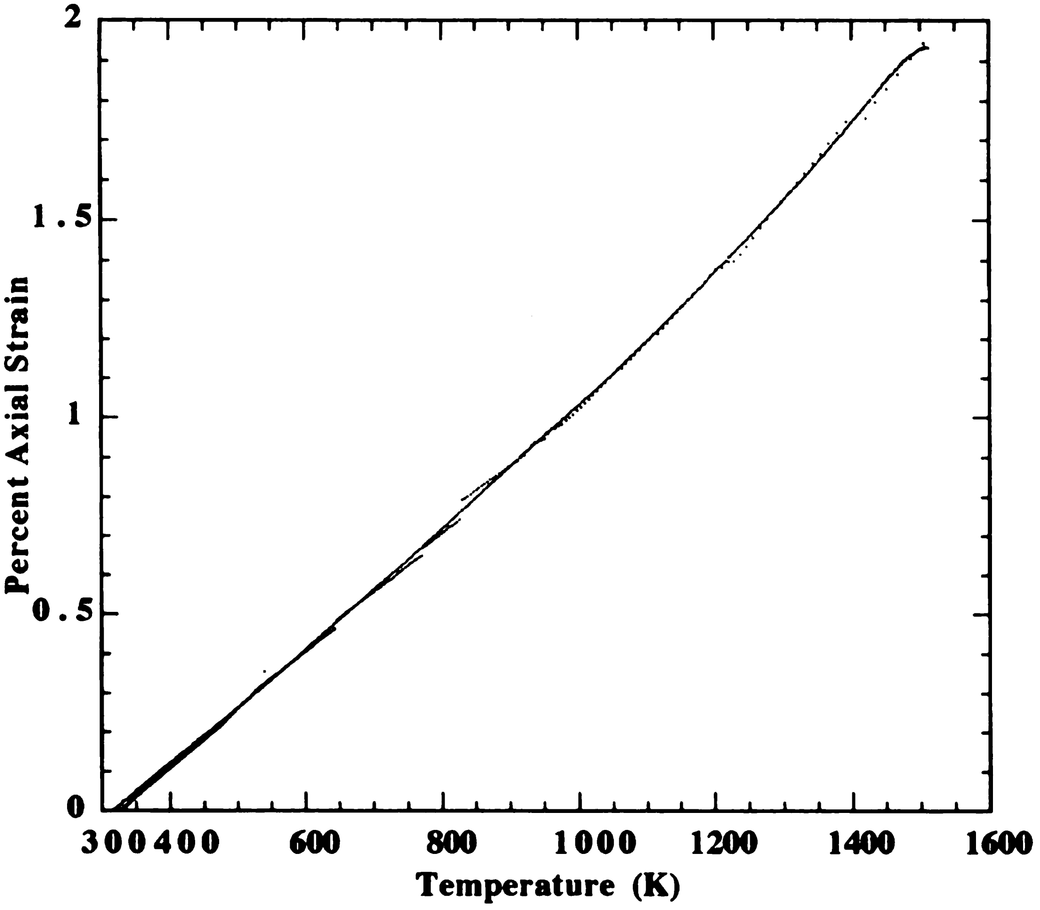

Figure 76 Axial strain vs. temperature curve for monolithic NiAl.

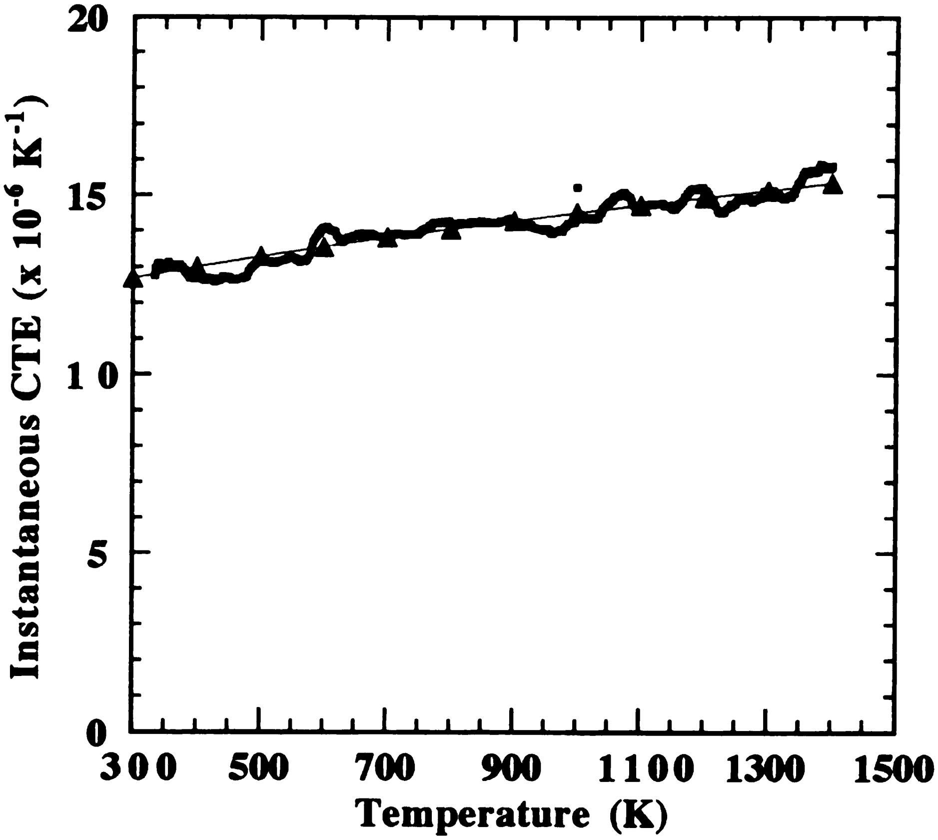

Figure 77 A plot of the instantaneous and theoretical CTE for monolithic NiAl.

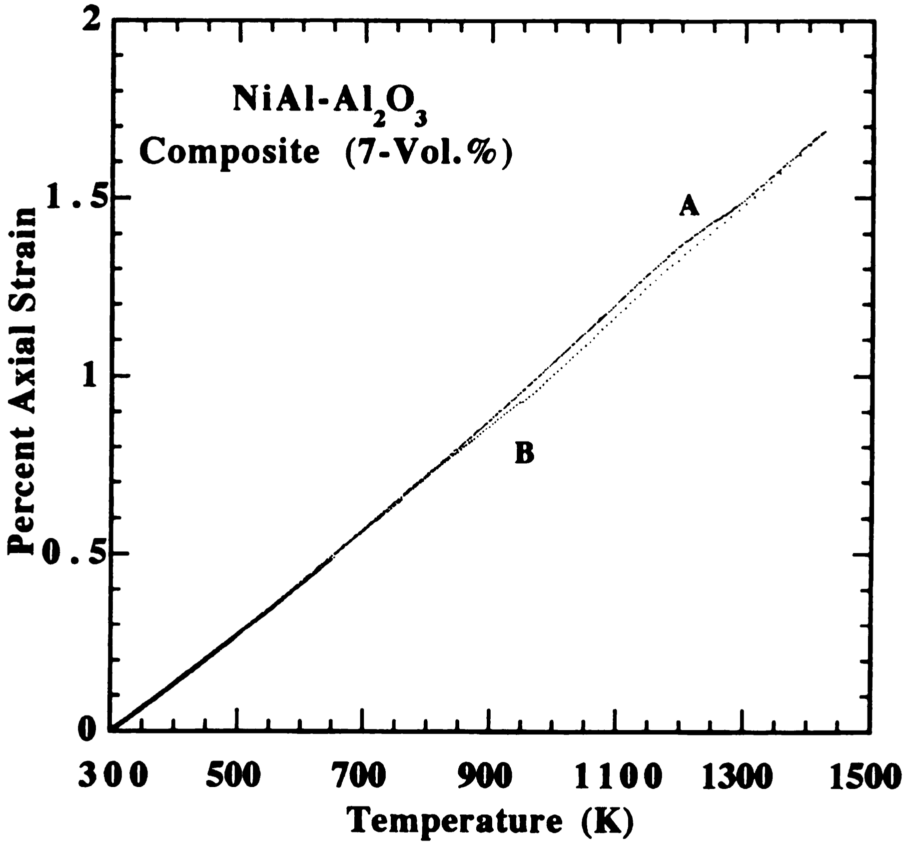

Figure 78 The axial strain vs. temperature plot for a 7 vol.% NiAl-Saphikon composite.

To further illustrate the effects of fiber reinforcement on the thermal expansion behavior of the composite, the instantaneous heating and cooling CTE for both the monolithic and the 7 vol.% NiAl-(Al_2O_3) composite, along with the instantaneous CTE for the Saphikon fiber, are shown in Figure 80a and 80b, respectively. As the plots illustrate, the instantaneous CTE of the 7 vol.% NiAl-(Al_2O_3) composite agrees well with the rule-of-mixtures (ROM) prediction at low temperatures, but deviates at ~600 K and begins to approach the monolithic value. At ~1100 K the instantaneous CTE decreases dramatically and approaches the fiber CTE at ~1300 K, after which it increases toward the ROM value. The behavior of the cooling half-cycle instantaneous CTE shown in Figure 288b, and indicates a distinctively different behavior from the heating curve CTE. Comparing the CTE of the heating and cooling half-cycle indicates a discontinuous jump at ~1450 K. As the composite cools the average value approaches the ROM prediction.

Figure 81 shows the axial strain versus temperature of a 5-vol.% NiAl-(Ni-Al_2O_3) composite. Qualitatively, this curve is similar to the uncoated fiber composite curve shown in Figure 78. The heating and cooling knee temperatures occur at, **A** at ~1255 K and **B** at ~998 K, respectively. Though similar in form, several aspects differentiate the thermal response of the two types of composites. First, measuring the change in strain between the heating and cooling half-cycles, at a temperature midway between T_{Bknee} and T_{Aknee}, the uncoated fiber composite has a hysteresis strain of -0.038 and the nickel-coated fiber has a differential strain of -0.062, indicating a 60% increase in hysteresis strain occurs for the nickel-coated fiber composite. Furthermore, the average CTEs (calculated from a linear fit), above the knee temperature for the uncoated and nickel coated fibers, are $14.0 \times 10^{-6} K^{-1}$ and $13.4 \times 10^{-6} K^{-1}$, respectively.

The instantaneous CTE for the 5-vol.% NiAl-(Ni-Al_2O_3) strain data are shown in Figure 82. On average, the ROM prediction is followed at temperatures below 1100 K. On nearing, and subsequently passing through the knee temperature, an increase in the CTE is observed, followed by a large decrease, with a minimum at ~1300 K. Beyond the

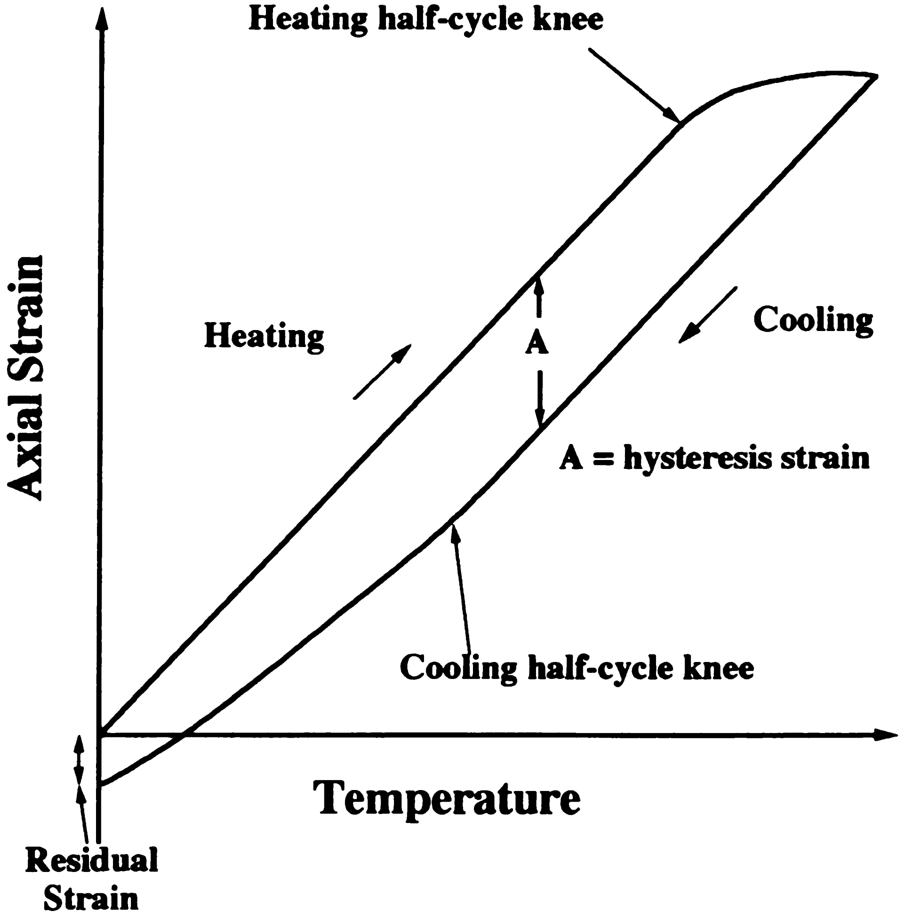

Figure 79 A schematic of the thermal strain vs.temperature plot.

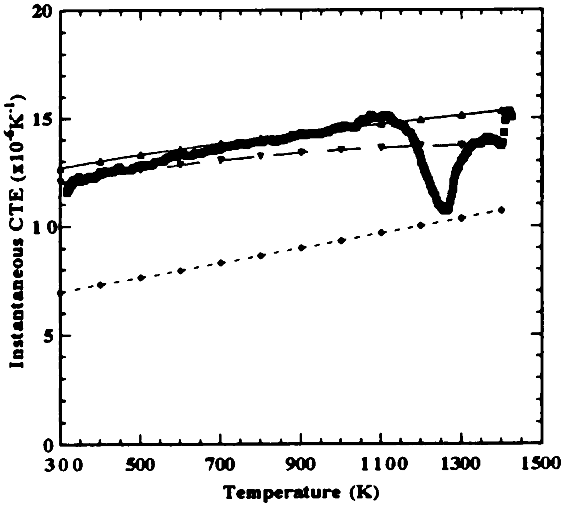

(a)

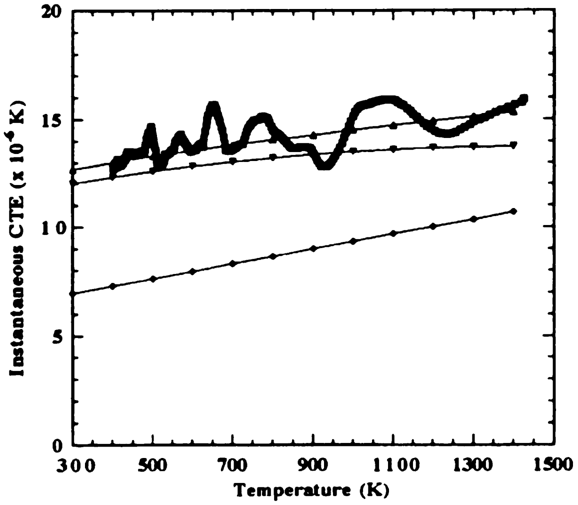

(b)

Figure 80 (a) heating and (b) cooling CTE plots of a 7-vol.% Saphikon-NiAl composite.

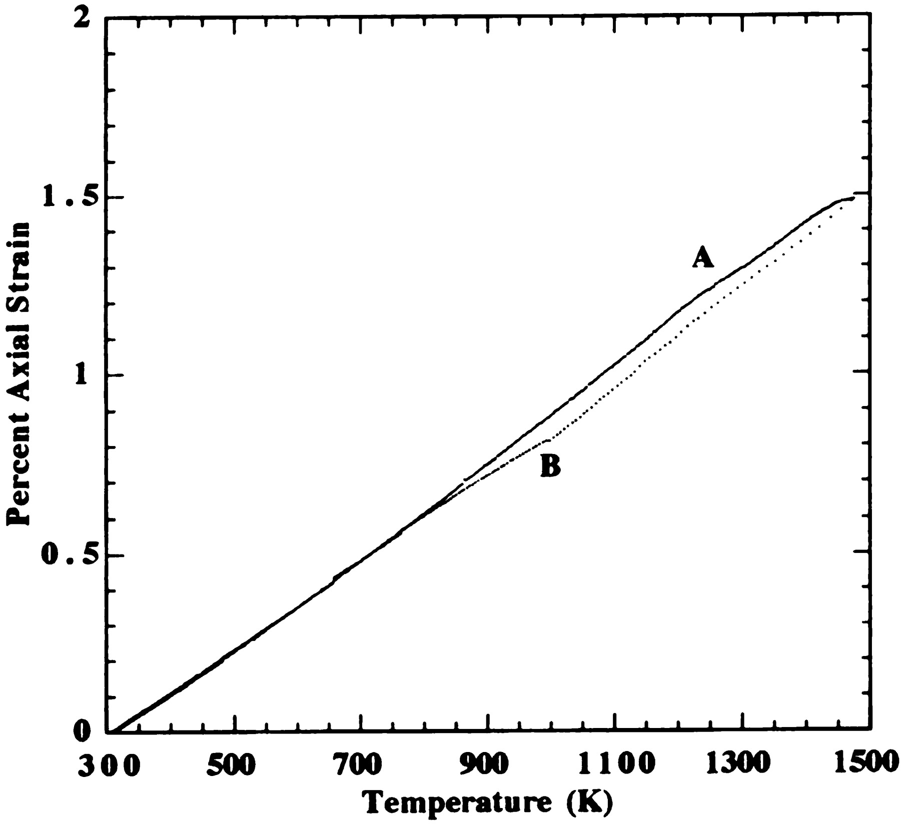

Figure 81 The axial strain vs. temperature for a 5-vol.% NiAl-(Ni-Al_2O_3) composite.

minimum, the CTE increases toward the ROM value again, and then finally decreases. (Note that the CTEs at low temperatures are equal for the heating and cooling half-cycles.)

4.9.2 Thermal Expansion Response of NiAl-(Uncoated- and Coated-Saphikon) Composites as a Function of the Number of Cycles

4.9.2.1 7-Vol.% NiAl-Saphikon Composites Three thermal cycles of a 7-vol.% NiAl-Saphikon composite, plotted in Figure 83 illustrate several effects. (Note that the first cycle corresponds to the data presented in Figure 78.) In contrast to cycle #1, cycles #2 and #3 show a less distinct knee in the heating half-cycle. For the three cycles, no net residual strain accumulation, $\Delta\varepsilon_p$, was measured. The heating-cooling half-cycle hysteresis strain indicates that plastic yielding occurred during the heating half-cycle and was due to the presence of the fibers. Furthermore, the knee and small slope change of the heating half-cycle suggest that fiber-matrix adhesion was poor. The thermal expansion parameters for these plots (and other composites) are tabulated in Table 17. The data from Table 17 indicates that the knee temperature of the heating half-cycle increases after the first cycle and then decreases. On the other hand, the knee temperature during the cooling cycle appears to be constant for the first two cycles and then increases for the third cycle.

Figure 84 shows the instantaneous CTE plots for each heating half-cycle. Each cycle has the same qualitative shape, exhibiting a close match to the ROM predictions, followed by a gradual increase until the knee temperature is reached, where after a decrease in the CTE occurs. The instantaneous CTE plot shown in Figure 84a illustrates that the CTE of the first cycle reaches a value smaller than the CTE of the fiber. The instantaneous CTEs for the cooling half-cycles are shown in Figure 85. The general shape of the curve corresponds to a CTE value that is approximately equal to that for monolithic NiAl, followed by an increase above this value, and then a decrease to a value

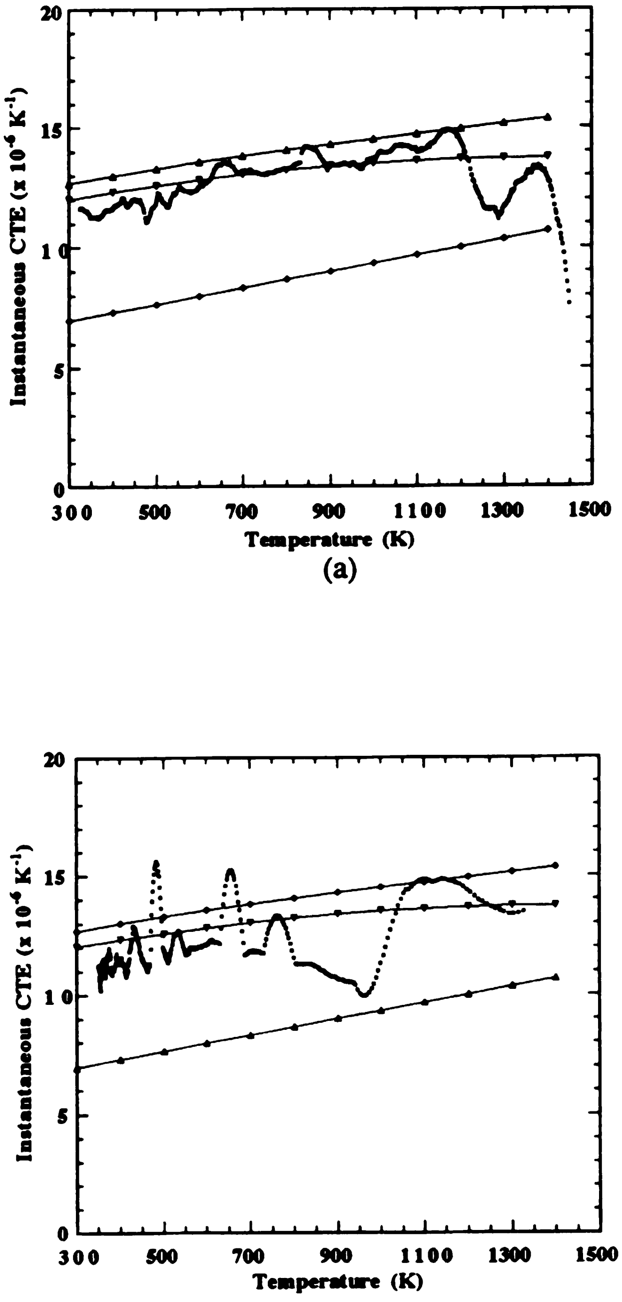

(a)

(b)

Figure 82 (a) heating and (b) cooling CTEs of a 5-vol.% NiAl-(Ni-Al_2O_3) composite.

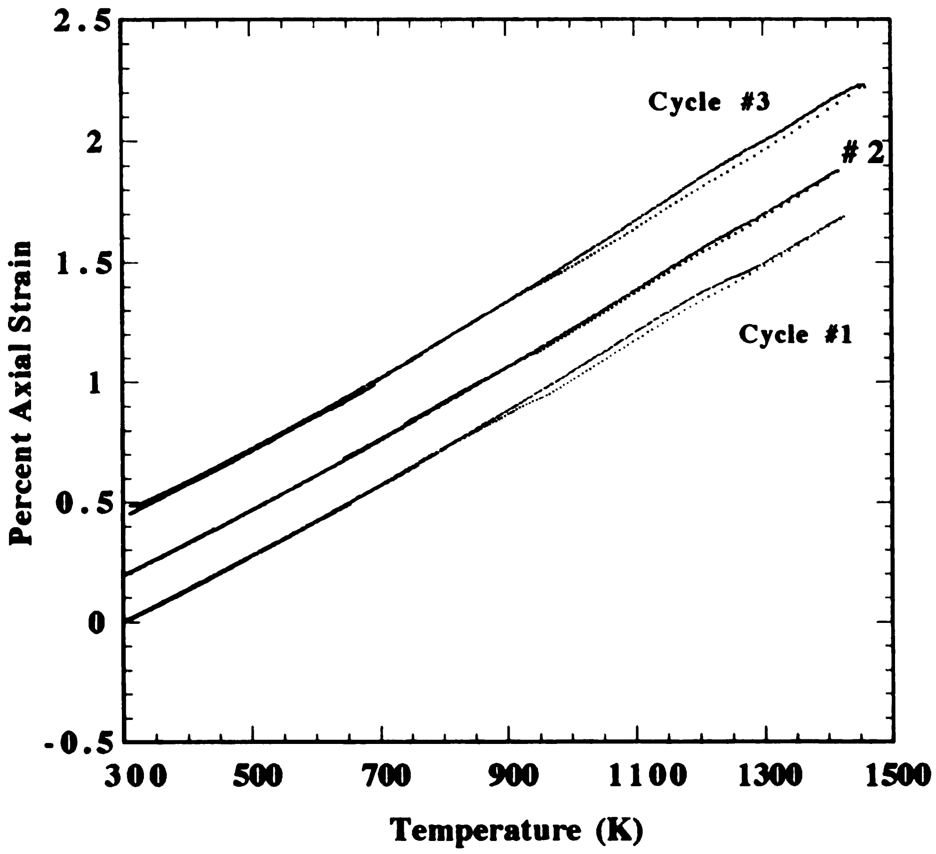

Figure 83 A plot of thermal strain vs. temperature for a 7-vol.% NiAl-Al_2O_3 composite.

Table 16 Thermal expansion parameters for composites as a function of cycle.

7-vol.% NiAl-Al_2O_3 Composite

Cycle #	Knee Temperature Heating (K)	Knee Temperature Cooling (K)	Hysteresis Strain	$\Delta\varepsilon_p$	Avg.CTE ($x10^{-6}$) Below T_{knee}	Avg.CTE ($x10^{-6}$) Above T_{knee}
1	1148 ± 5	954 ± 10	-0.0375	~0	14.8	15.2
2	1158 ± 5	945 ± 10	~0	~0	14.6	15.0
3	1174 ± 5	1014 ± 10	-0.0375	~0	15.1	15.8

7-vol.% NiAl-(Ni-Al_2O_3) Composite

Cycle #	Knee Temperature Heating (K)	Knee Temperature Cooling (K)	Hysteresis Strain	$\Delta\varepsilon_p$	Avg.CTE ($x10^{-6}$) Below T_{knee}	Avg.CTE ($x10^{-6}$) Above T_{knee}
1	1125 ± 5	-	-0.0875	-0.0521	12.8	12.2
2	1175 ± 5	-	-0.1375	-0.0729	13.2	8.5
3	1228 ± 5	-	-0.2120	-0.1978	12.1	7.1

7-vol.% NiAl-(Nb-Al_2O_3) Composite

Cycle #	Knee Temperature Heating (K)	Knee Temperature Cooling (K)	Hysteresis Strain	$\Delta\varepsilon_p$	Avg.CTE ($x10^{-6}$) Below T_{knee}	Avg.CTE ($x10^{-6}$) Above T_{knee}
1	1115 ± 5	942 ± 10	-0.0729	-0.0417	12.6	10.2
2	1125 ± 5	996 ± 15	-0.1146	-0.0729	12.8	8.9
3	1228 ± 5	969 ± 30	-0.0625	-0.0521	12.5	8.8

7-vol.% NiAl-(Ti-Al_2O_3) Composite

Cycle #	Knee Temperature Heating (K)	Knee Temperature Cooling (K)	Hysteresis Strain	$\Delta\varepsilon_p$	Avg.CTE ($x10^{-6}$) Below T_{knee}	Avg.CTE ($x10^{-6}$) Above T_{knee}
1	-	975 ± 20	-0.1163	-0.0697	13.4	-
2	-	-	-0.0581	-0.0233	13.4	-
3	-	1044 ± 10	-0.0466	~0	13.1	-
4	-	1101 ± 8	-0.0349	~0	13.6	-

Table 16 (cont'd).

5-vol.% NiAl-(Ti-Al_2O_3) Composite						
Cycle #	Knee Temperature Heating (K)	Knee Temperature Cooling (K)	Hysteresis Strain	$\Delta\varepsilon_p$	Avg.CTE ($x10^{-6}$) Below T_{knee}	Avg.CTE ($x10^{-6}$) Above T_{knee}
1	-	-	-0.0614	-0.0538	12.4	
2	-	1008 ± 10	-0.0511	-0.0338	13.3	
3	-	-	-0.0409	-0.1125	13.5	
4	-	954 ± 10	-0.0511	-0.0112	13.5	

approaching the ROM prediction. At temperatures below ~900 K, the curve becomes extremely erratic due to the noisy data in the low-temperature cooling half-cycle. A distinctive difference between the CTE of the heating half-cycle and the cooling half-cycle is the discontinuity in CTE occurring at the maximum temperature. This discontinuity is a consequence of the composite response changing from a plastic deformation mode to an elastic deformation mode as the reversal in temperature occurs.

4.9.2.2 7-Vol.% NiAl-(Ni-Saphikon) Composite The thermal cycle plots of a 7-vol.% Ni-coated Saphikon fiber composite shown in Figure 86 differ from the previously described uncoated fiber composite. The thermal strain in the nickel-coated fiber composites exhibit distinct heating half-cycle knees, followed by a large change in CTE (given by the slope of the strain vs. temperature curve). Upon cooling, a wide hysteresis and a net compressive residual strain develops. Furthermore, the knee in the cooling half-cycle was absent for all cycles. The behavior of the 7-vol.% Ni-coated fiber composite also contrasts with the thermal expansion response of the 5 vol.% nickel-coated fiber composite, as shown in Figure 81, where both a heating and cooling half-cycle knee occurred. These results suggest that the thermal response of a composite is a function of the volume fraction.

The heating half-cycle instantaneous CTE plots for each thermal cycle are shown in Figure 87. These plots are similar to the instantaneous CTE of the 5 vol.% NiAl-(Ni-Saphikon) composite shown in Figure 82, and similar to the behavior of uncoated fiber composite shown in Figure 80. At the lower temperatures the CTEs follow ROM predictions and deviate toward the NiAl CTE for temperatures approaching the knee temperature. At the knee temperature, a dramatic decrease in the instantaneous CTE is seen, followed by an increase toward the ROM prediction and then a decrease. Furthermore, the CTE of the second heating half-cycle dips below the fiber CTE value.

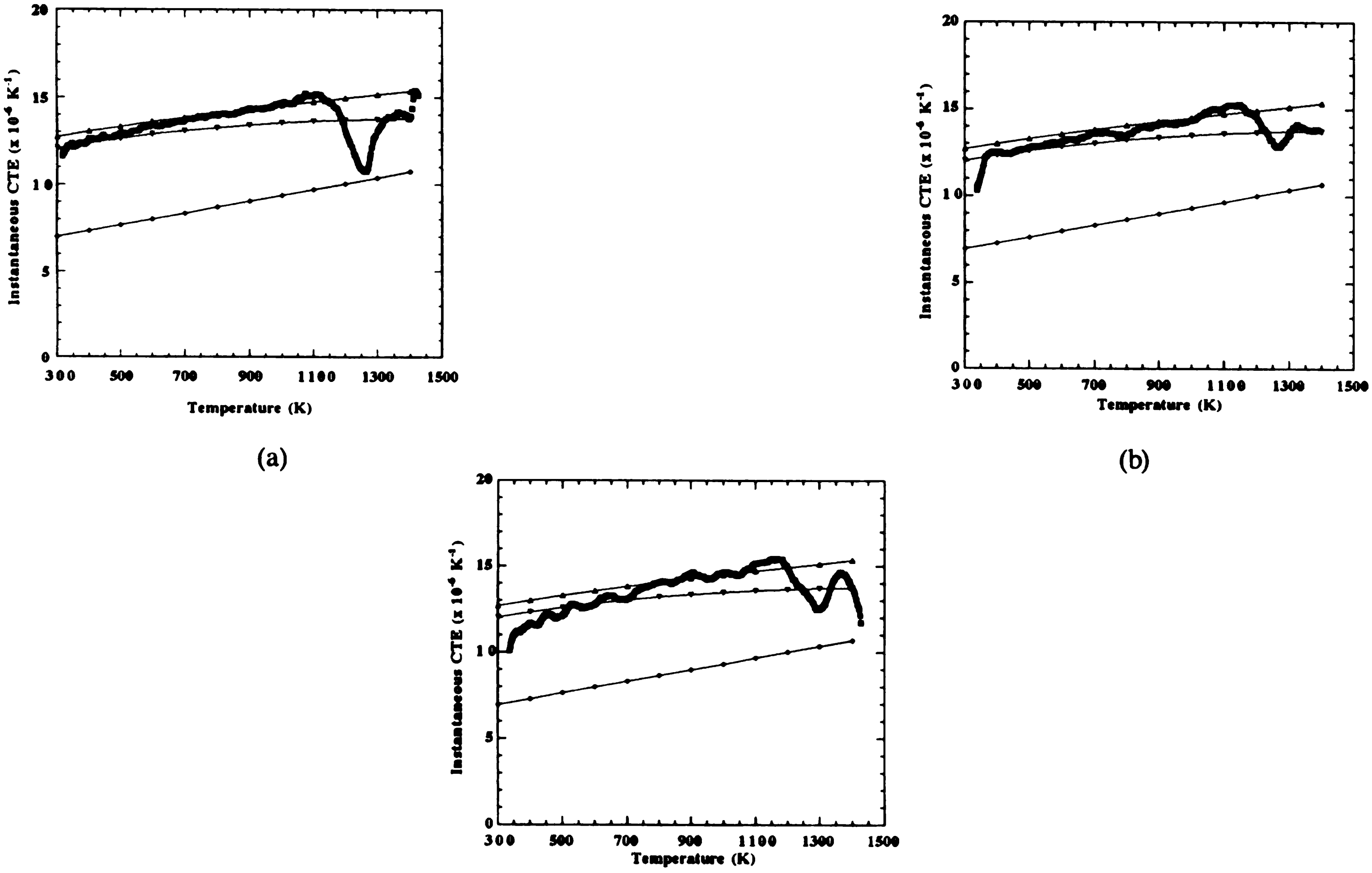

(a)

(b)

(c)

Figure 84 Plots of the CTE for a 7-vol.% NiAl-Saphikon composite.

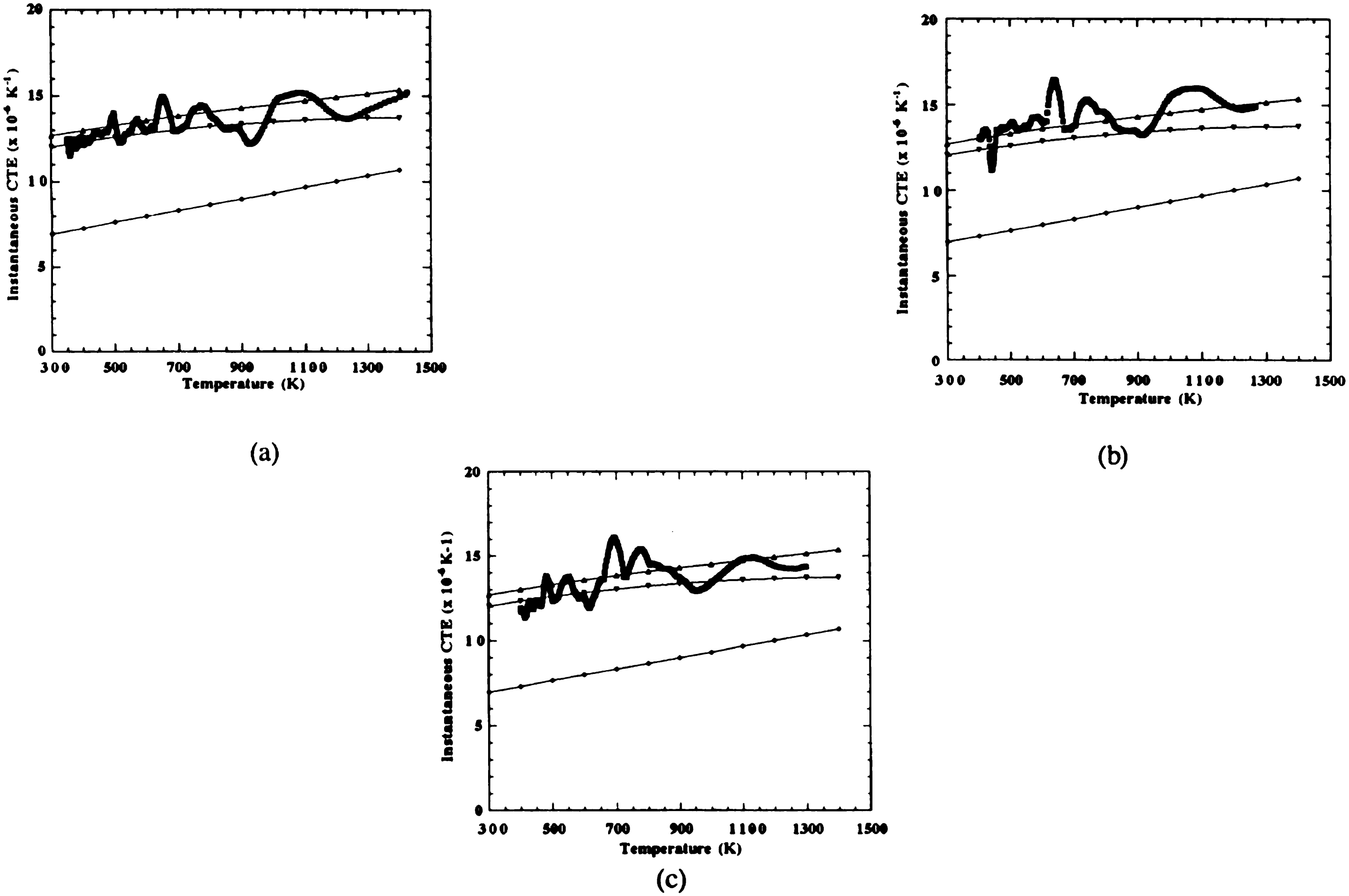

(a)

(b)

(c)

Figure 85 Plots of the CTE for a 7-vol.% NiAl-Saphikon composite.

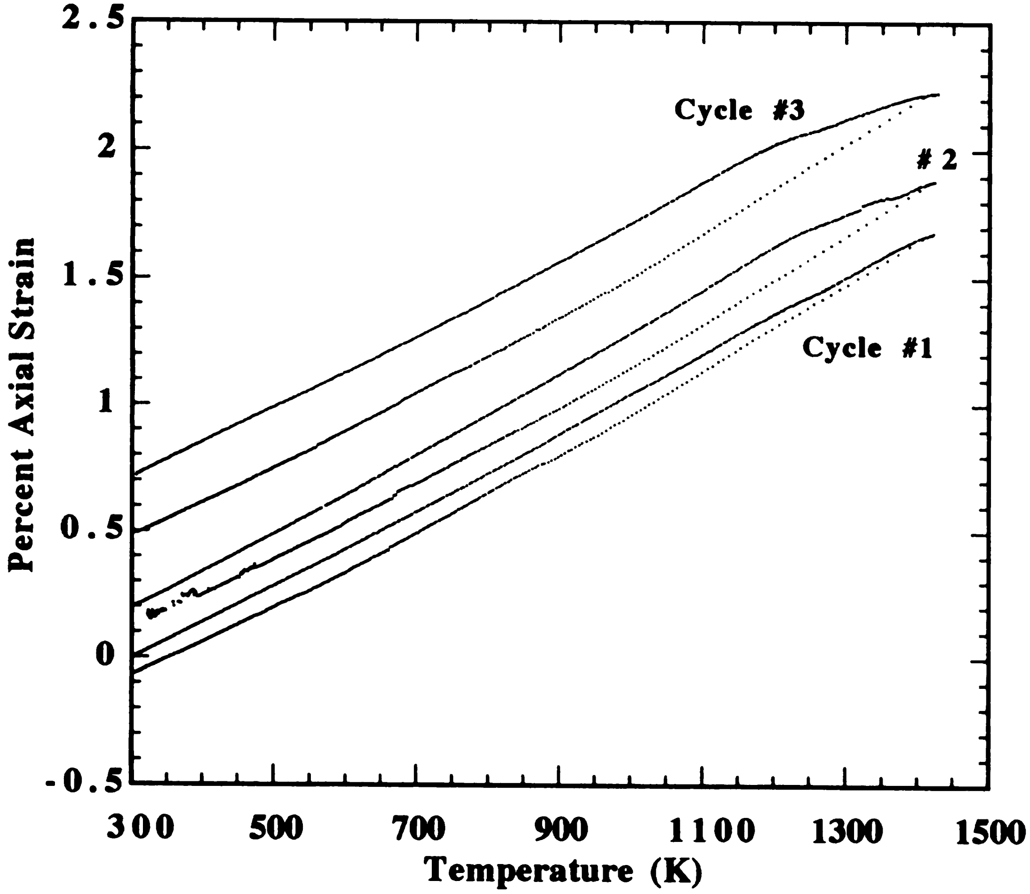

Figure 86 The thermal strain vs. temperature for a 7-vol.% NiAl-(Ni-Al_2O_3) composite.

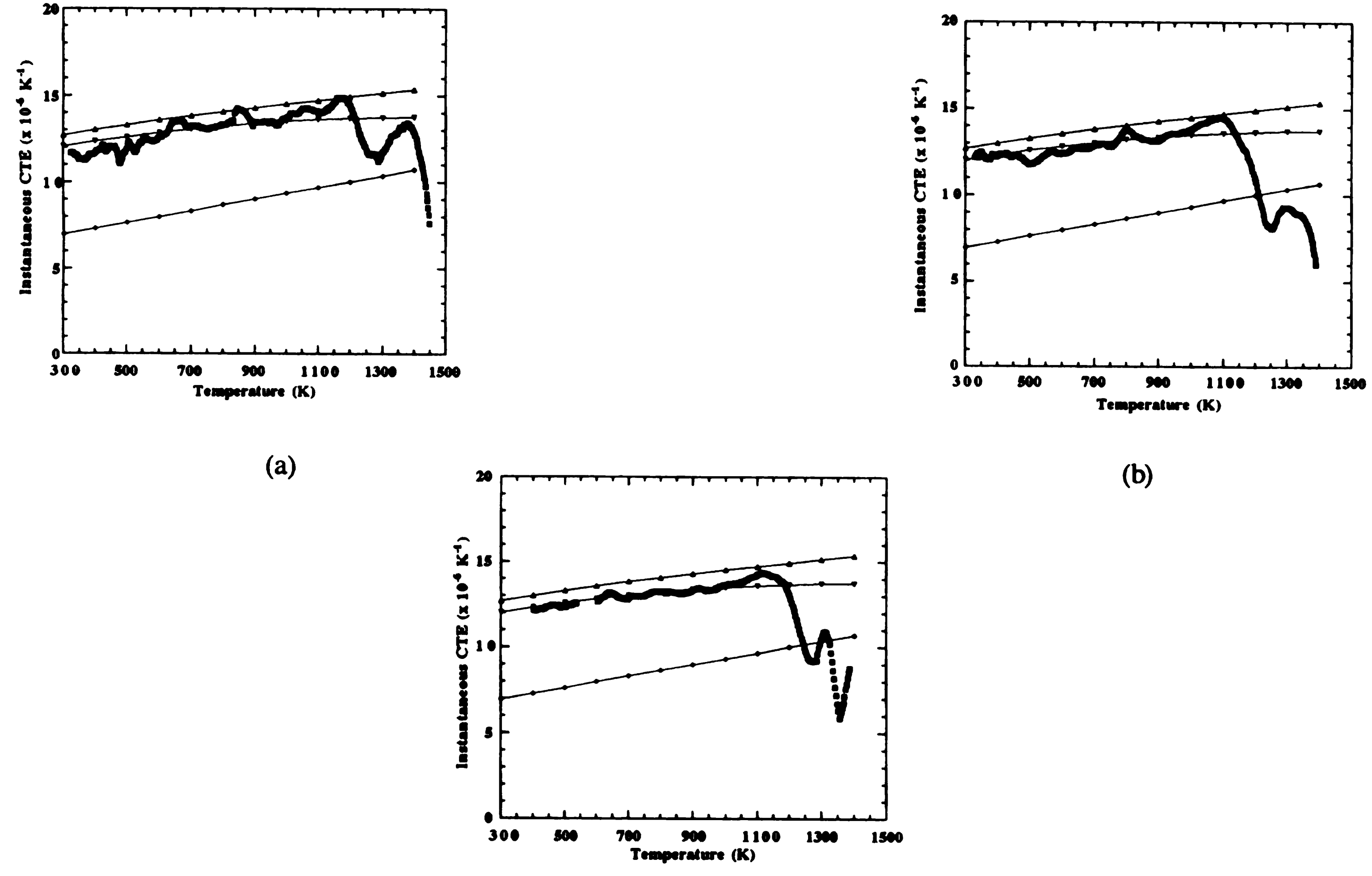

(a)

(b)

(c)

Figure 87 Plots of the CTE for a 7 vol.% NiAl-(Ni-Al_2O_3) composite.

4.9.2.3 7-Vol.% NiAl-(Nb-Saphikon) Composite The thermal expansion response for three complete cycles of a 7-vol.% NiAl-(Nb-Saphikon) composite is plotted in Figure 88. These curves indicate thermal responses similar to the nickel-coated fiber composite curves shown in Figure 83. In particular, as shown by the data in Table 17, the average CTE below the knee temperature in the heating half-cycles were found to be approximately the same after the first cycle. In addition, for all three cycles, the average CTE of the niobium-coated fiber composite above the knee was less than below the knee and decreased to an approximate constant value of 8.9 x 10^{-6} K^{-1} after the first cycle. From Table 17, the knee temperature value increases from 1115 K to 1178 K as the number of complete cycles increases. For all three cycles the cooling half-cycle data was noisy, but in general, a net residual strain occurred.

Figure 89 show plots of the instantaneous CTE for each heating half-cycle of the 7-vol.% NiAl-(Nb-Saphikon) composite. Below the knee temperatures, the thermal response of the composite approximately follows the ROM prediction. In contrast to the thermal expansion behavior of the uncoated and nickel-coated fiber composite, when approaching the knee temperature no rise in the CTE is occurs. Above the knee temperature the CTE steeply decreased to values below the CTE of the fiber, followed by an increase to a values less than the ROM predictions.

4.9.2.4 7-Vol.% NiAl-(Ti-Saphikon) Composites The thermal strain plot for four complete cycles of a 7-vol.% and 5-vol.% NiAl-(Ti-Saphikon) composite are plotted in Figure 90a and b, respectively. These composites behave differently than the ones previously discussed. The absence of knees in the heating half-cycle is the most notable difference. Also, as the number of cycles increases, the net residual strain and the hysteresis strain decrease, while a knee in the cooling half-cycle begins to appear.

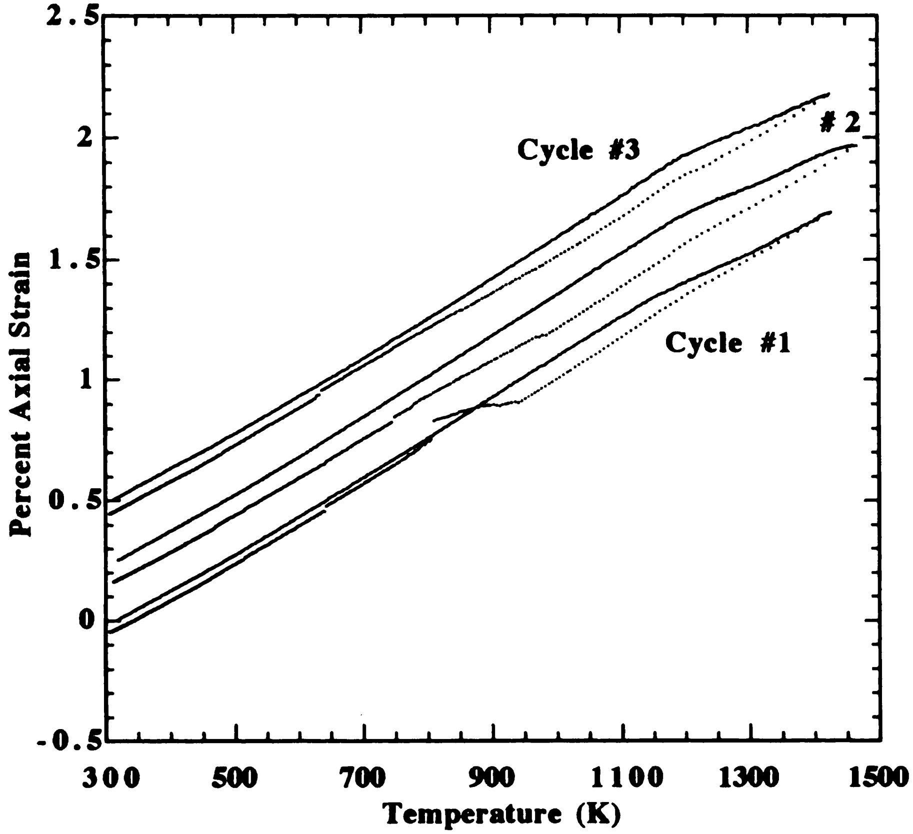

Figure 88 The thermal strain vs. temperature for a 7-vol.% NiAl-(Nb-Al_2O_3) composite.

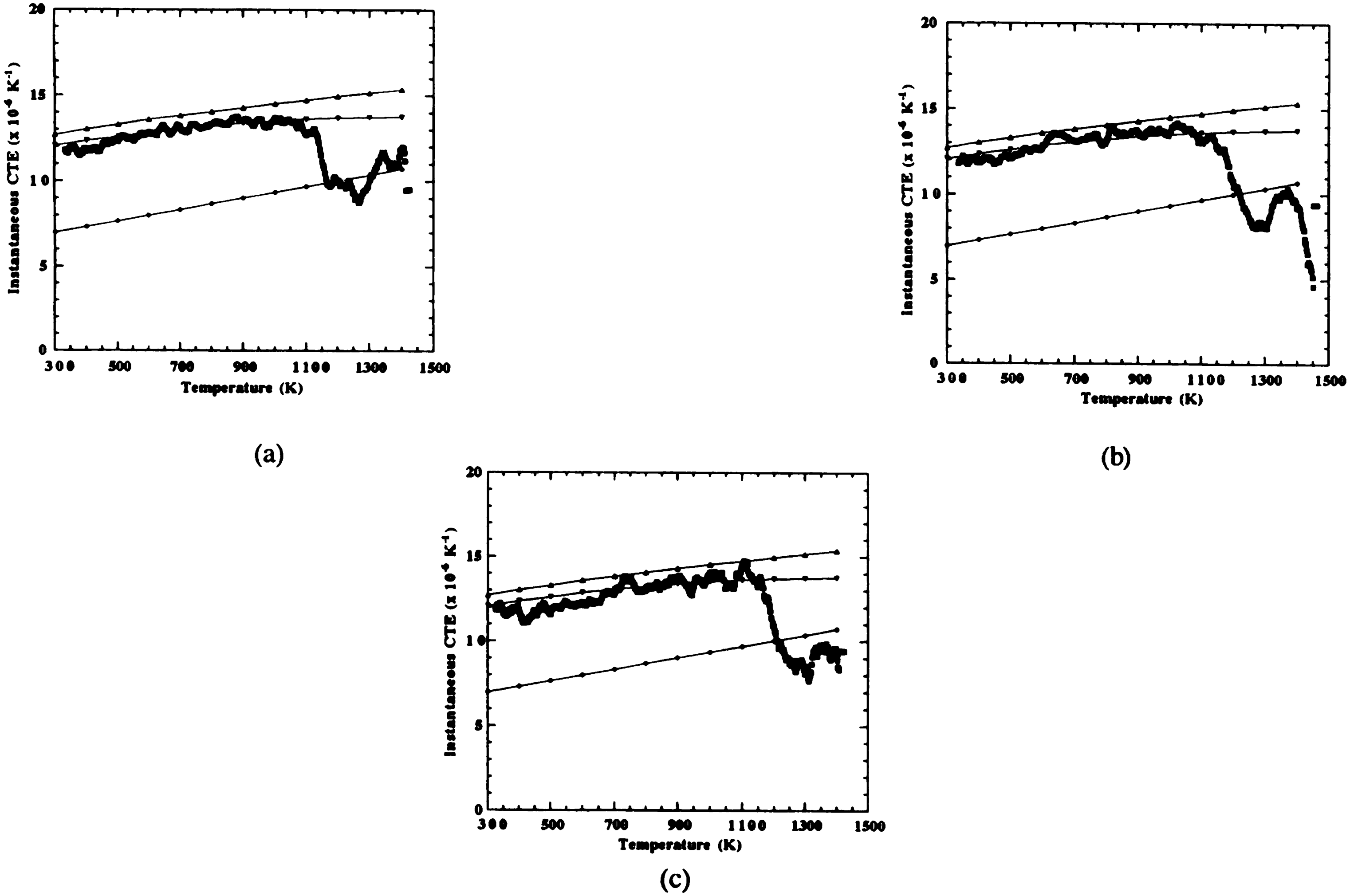

(a) (b) (c)

Figure 89 Plots of the CTE for a 7 vol.% NiAl-(Nb-Al_2O_3) composite.

Table 17 indicates that the average CTE of the heating half-cycle for either the 7-vol.% or the 5-vol.% composites is approximately constant at 13.5 x 10^{-6} K^{-1}, which is larger than either the nickel- or niobium-coated fiber composites, but less than the uncoated fiber composite. Data from Table 17 also indicates that the knee temperature for the cooling half cycle of the 5-vol.% composite increases as the number of cycles increases; however, the trend for the 7-vol.% composite is not clear.

The instantaneous CTE plots, for each heating half-cycle of the 7-vol.% and 5-vol.% NiAl-(Ti-Al_2O_3) composite, are shown in Figure 91 and 92, respectively. Except for the first cycle, of the 5-vol.% composite where a decrease in CTE is seen after ~1200 K, the CTE, on average, tends to be slightly higher than the ROM predictions. A similar behavior is seen for the 7-vol.% composite, though no decrease in CTE is seen during the first cycle (this, however, may be a consequence of the relatively low maximum temperature (~1000K)).

4.9.3 Discussion of the Thermal Strain Curves and the Corresponding Instantaneous CTE Curves

4.9.3.1 General Discussion of Composite Thermal Expansion Behavior The coefficient of thermal expansion of monolithic materials is a simple function of temperature, not related to any internal mechanical deformation or external variable such as heating or cooling rate (assuming that uniform temperature is maintained). The fibers influence the axial thermal strain and matrix stress as schematically depicted in Figure 93. The assumptions used to predict this ideal behavior include: (a) that the fiber remains completely elastic throughout the entire temperature range, (b) perfect fiber-matrix bonding, and (c) the effects of transverse stresses are small (for metal matrix composites this is generally the case since the Poisson ratio of ceramic fibers is low (~0.2)). Furthermore, the composite is assumed to be metallurgically stable and the fibers are well separated.

The material parameters and physical processes determine the longitudinal strain response of a unidirectionally reinforced composite can be described using the model of

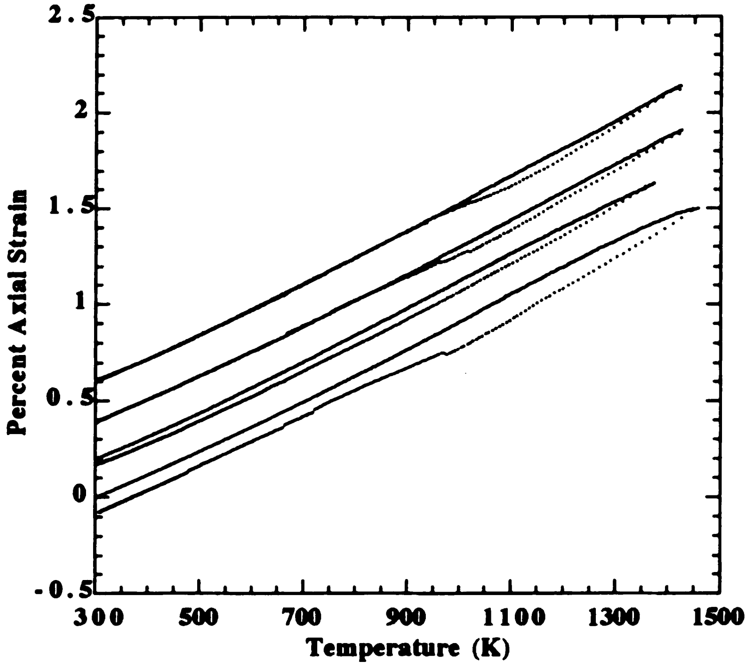

(a)

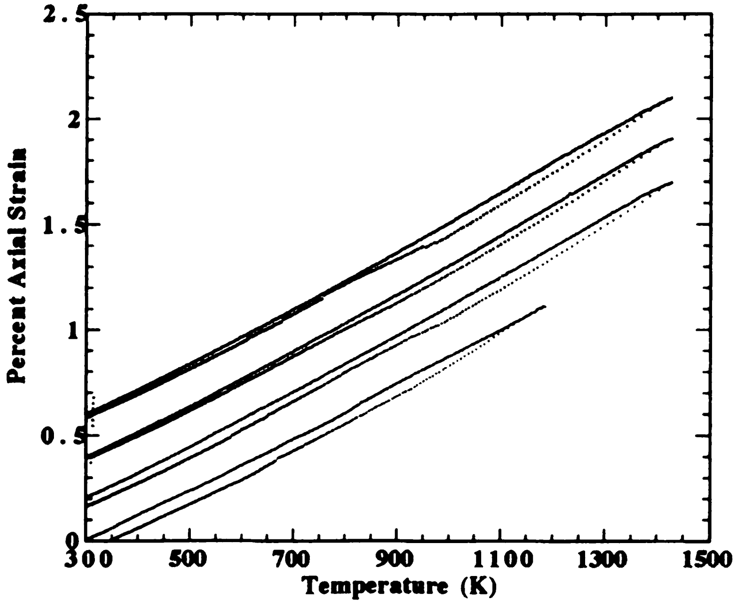

(b)

Figure 90 The thermal strain for a 7- and 5-vol.% NiAl-(Ti-Al_2O_3) composite.

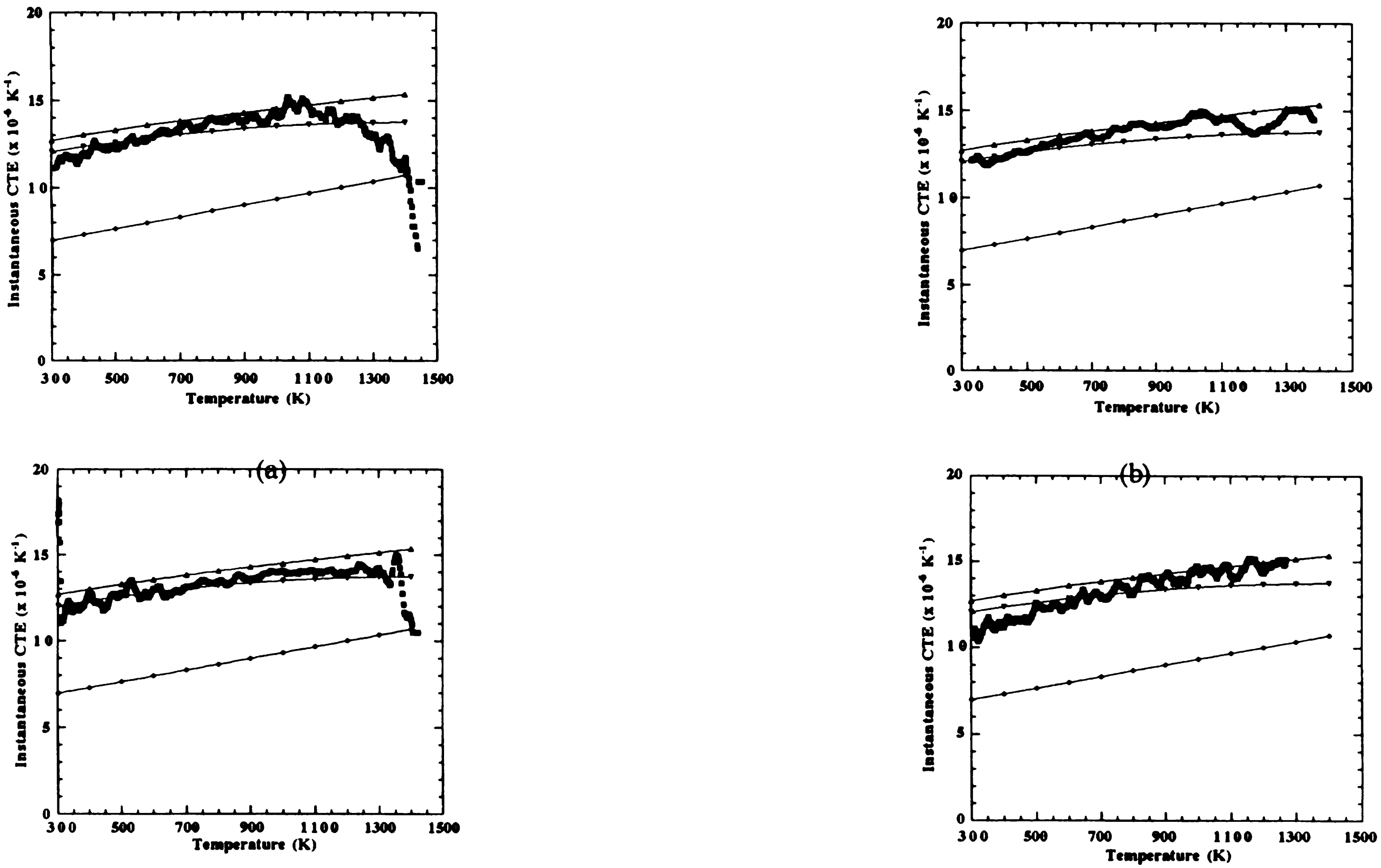

(a)

(b)

(c)

(d)

Figure 91 Plots of the CTE for a 7 vol.% NiAl-(Ti-Al_2O_3) composite.

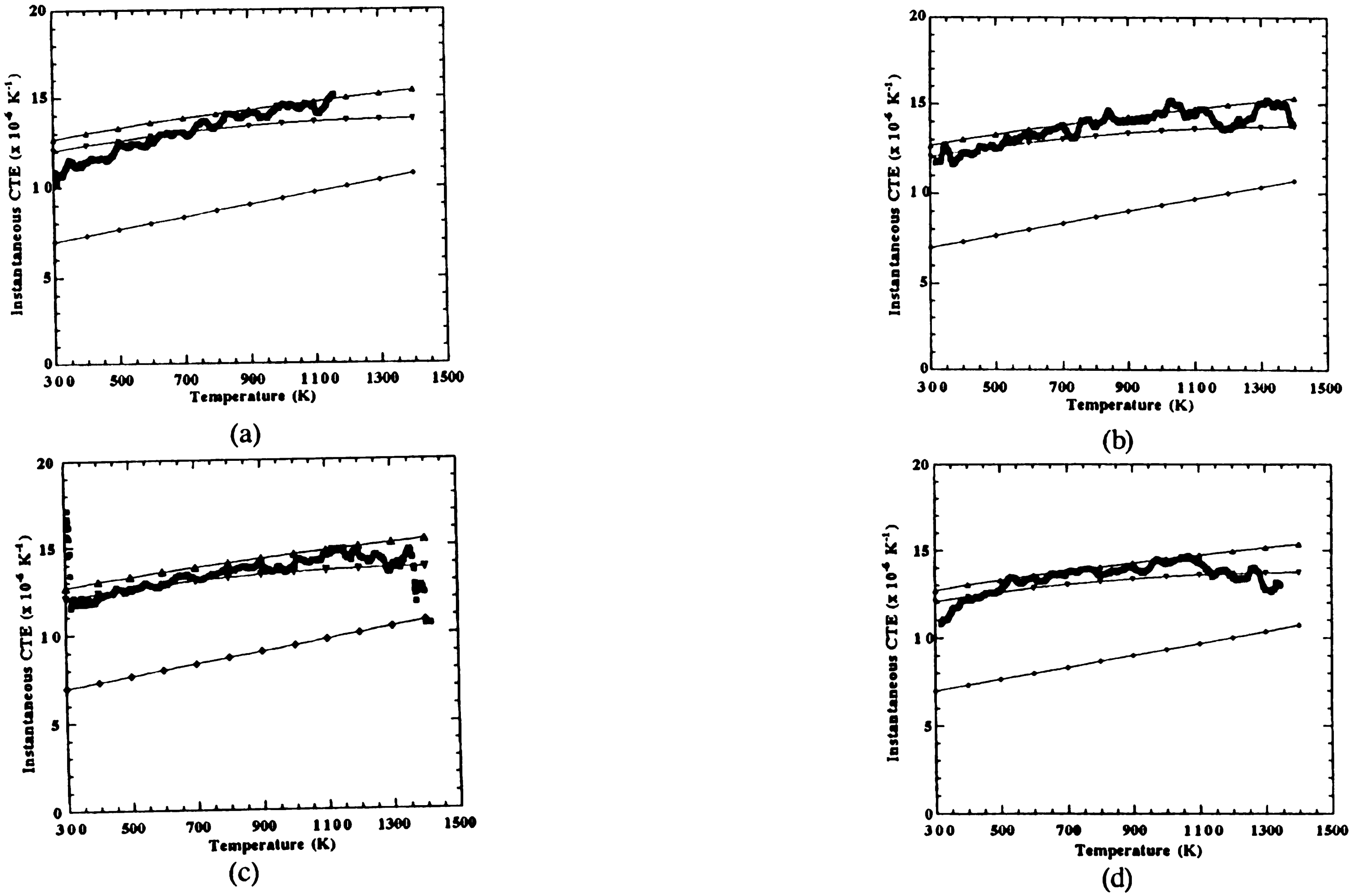

(a) (b) (c) (d)

Figure 92 Plots of the CTE for a 5 vol.% NiAl-(Ti-Al_2O_3) composite.

Garmong [Garmong, 1974]. In this description, with the absence of an externally applied stress, stress equilibrium requires that,

$$\sigma_f V_f + \sigma_m V_m = 0\,, \qquad \text{4-11}$$

and strain continuity across the fiber-matrix interface requires that,

$$\varepsilon_f = \varepsilon_m\,, \qquad \text{4-12}$$

where σ_i represents stress, ε_i represents total strain, V_i represents the volume fraction, and i equals either f or m and refer to the fiber and the matrix, respectively. The total composite strain, ε_c, is the sum of independently acting strains and is given by

$$\varepsilon_c = \varepsilon_{thermal} + \varepsilon_{mechanical}\,, \qquad \text{4-13}$$

where

$$\varepsilon_{mechanical} = \varepsilon_{elastic} + \varepsilon_{plastic} + \varepsilon_{creep}\,. \qquad \text{4-14}$$

Theses strains are defined mathematically by

$$\varepsilon^{i}_{thermal} = \int_{T_1}^{T_2} \alpha_i dT\,, \qquad \text{4-15}$$

and the elastic strain is given by

$$\varepsilon^{i}_{elastic} = \frac{\sigma_i}{E_i}\,, \qquad \text{4-16}$$

where i represents either the fiber or matrix.

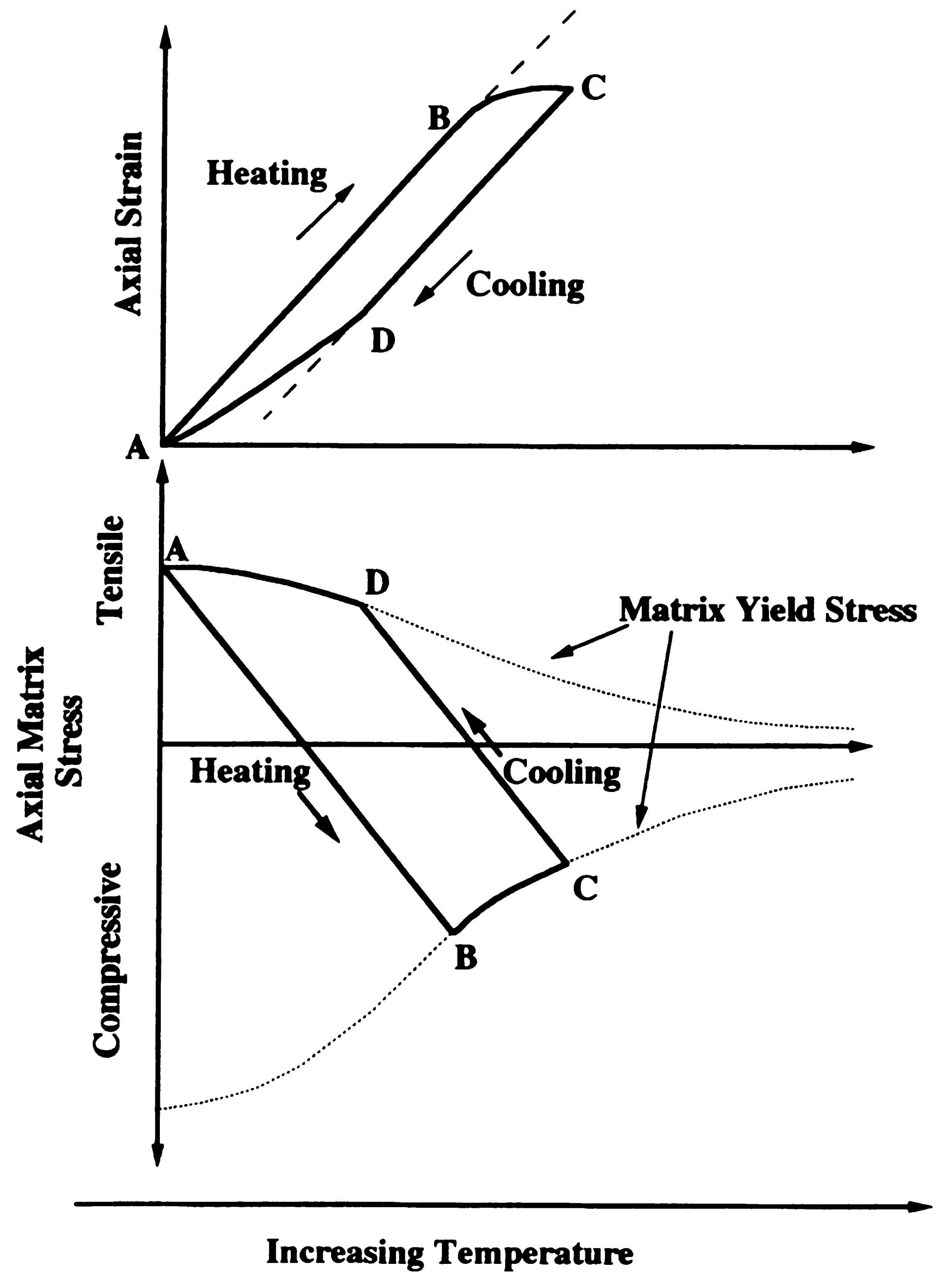

Figure 93 Changes in (a) specimen strain and (b) matrix stress during thermal cycling.

The plastic strain experienced by the matrix can be described by the Ludwik relation [Ludwik, 1909],

$$\varepsilon^{m}_{plastic} = \left[\frac{\sigma_m - \sigma_{ys}}{K}\right]^{\frac{1}{n}}, \qquad 4\text{-}17$$

where σ_{ys} is the instantaneous yield strength of the matrix, and K and n are constants. Since no straightforward formulation for creep under varying stress and temperature conditions is available, the Dorn formulation describing steady state creep can be used to predict the creep strain of the matrix,

$$\varepsilon^{m}_{creep} = \int_{T_1}^{T_2} A\left(\frac{\sigma_m}{G}\right)^{s}\left(\frac{Gb}{kT}\right)D_o e^{-\frac{Q}{kT}}\left(\frac{dt}{dT}\right)dT, \qquad 4\text{-}18$$

where A is a constant and s is the stress exponent, G is the matrix shear modulus, b is the Burgers vector, D_o is the frequency factor, Q is the activation energy for diffusion, k is the Boltzmann's constant, $\frac{dt}{dT}$ is the inverse heating rate, and R is the gas constant. From this description, the fiber strain induced by the load transfer from the matrix is called the mechanical strain.

Equations 4-15 through 4-18 indicate the material parameters and strains affecting the high-temperature thermal expansion of composites. Experimentally, the composite strain, ε_c, during a change in temperature, and in the absence of external loading can be measured and is given by

$$\varepsilon_c = \left(\frac{\Delta l}{l}\right)_c = \int_{T_1}^{T_2} \alpha_f dT + \varepsilon_{mechanical} \qquad 4\text{-}19$$

where α_f is the thermal expansion of the fiber. (An equivalent expression is valid for the matrix if one assumes perfect fiber-matrix bonding.) The experimentally measured composite CTE is defined as

$$\alpha_c = \frac{\partial}{\partial T}\left(\frac{\Delta l}{l}\right)_c \qquad 4\text{-}20$$

and, hence,

$$\alpha_c = \frac{\partial}{\partial T}\left[\int_{T_1}^{T_2} \alpha_f dT + \varepsilon_{mechanical}\right] \qquad 4\text{-}21$$

where the term in brackets represents the total composite strain (thermal plus mechanical) that the fiber experiences during a temperature change. Though the CTE is staightforwardly measured, the contributions from the individual strain terms cannot be readily separated.

The ideal thermal strain versus temperature of a composite experiencing one complete thermal cycle can now be qualitatively described by considering Figure 93a. (This discussion of the axial strain and stress versus temperature schematic compliments the discussion of the origin of longitudinal residual stresses in section 2.4.3.) Starting from point **A** the composite expands elastically (linear region of the plot) as the sample is heated to "**B**". At **B**, the matrix begins to deform plastically, causing a knee to develop, by either time dependent (creep) and/or time independent (yielding) deformation. Also, the knee represents the region where a change in the strain-temperature slope occurs. When cooling begins (**C**), the composite unloads elastically until "**D**" when the matrix yields causes a knee in the cooling half-cycle. After arriving back at the starting temperature no net dimensional change has occurred.

From the strain versus temperature schematic shown in Figure 93a, the ideal matrix stress state can be qualitatively illustrated as shown in Figure 93b. This figure illustrates that after post-fabrication cooldown, a longitudinal residual tensile stress (**A**), equal to the matrix yield stress, is present in the matrix. On heating, the matrix stress decreases linearly. The stress then passes through zero as the residual stresses relax and goes through a region of elastic compression as the fiber inhibits matrix expansion. Upon increasing temperature, the matrix stress increases to a value large enough to cause compressive yielding (plastic deformation) at **B**. A period of progressive plastic flow then follows with the matrix stress decreasing as the matrix relaxes. On cooling (from **C**), the composite unloads elastically and the matrix stress continues to decrease and passes through zero. With decreasing temperature the matrix contracts faster than the fiber and tensile stresses accumulate in the matrix. At **D** the matrix yields in tension as the residual stresses approach the matrix yield stress, before returning to "**A**".

This description of the thermal strain versus temperature behavior allows the thermal expansion quantities can be more completely defined:

Heating half-cycle knee: indicates the residual tensile matrix stress has been relieved and compressive stresses are sufficiently large to exceed the temperature dependent yield stress and cause the onset of compressive plastic deformation via creep or flow processes.

Cooling half-cycle knee: indicates the accumulation of matrix tensile stresses exceeds the matrix yield stress and causes plastic flow. (Generally this occurs at temperatures where creep processes are not active.)

Hysteresis strain: is the relative measure of the differential strain between heating and cooling half-cycles, generated by interfacial matrix flow processes occurring above the heating half-cycle knee.

Residual strain, $\Delta\varepsilon_p$: the compressive residual strain indicates that compressive creep processes caused compressive creep strains to occur above the heating half-cycle knee and is not fully recovered by the tensile stresses generated during cooldown.

Since the matrix has the important function of transferring the applied load to the stronger and stiffer fiber, understanding matrix-fiber load transfer is central to understanding the thermomechanical behavior of a composite. Matrix-fiber load transfer occurs when interfacial shear strains, resulting from elastic moduli differences between the fiber and the matrix, generate interfacial stresses. The magnitude and distribution of these interfacial shear stresses then determines the strengthening capabilities of a composite system. Following the approach by Myers and Chawla [Myers, 1984], assuming a single fiber in an infinite matrix, the distribution of the fiber stress and the interfacial shear stress is given by

$$\overline{\sigma}_f = E_f \varepsilon_c \left[1 - \frac{\tanh\left(\frac{\beta l}{2}\right)}{\frac{\beta l}{2}} \right], \qquad 4\text{-}22$$

and

$$\tau - \frac{E_f r_f \varepsilon_c \beta}{2} \, \frac{\sinh \beta \left[\left(\frac{l}{2}\right) - x \right]}{\cosh \beta \left(\frac{l}{2}\right)}, \qquad 4\text{-}23$$

respectively. The variation of $\overline{\sigma}_f$ and τ with x (the distance along the fiber) is shown in Figure 94. In equations 4-22 and 4-23 E_f is the fiber modulus, r_f the fiber radius, and ε_c the composite strain. In addition, the load transfer parameter is defined by

$$\beta = \left[\frac{2\pi G_m}{E_f A_f \ln\left(\frac{R}{r_f}\right)} \right]^{\frac{1}{2}}, \qquad 4\text{-}24$$

where A_f is the fiber cross-sectional area, R is defined in Figure 94, and G_m is the matrix

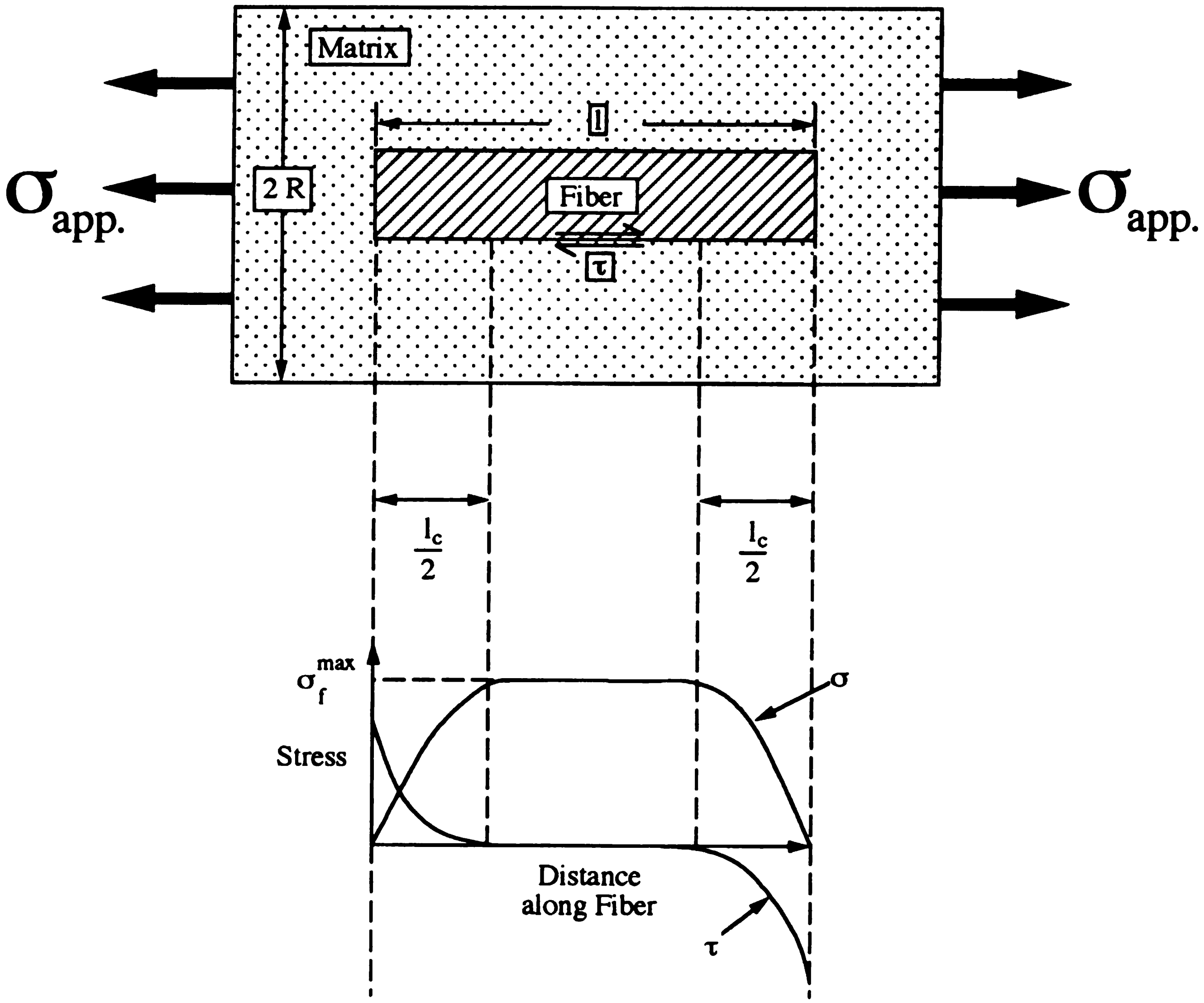

Figure 94 The fiber tensile stress, σ, and shear stress, τ, along the fiber-matrix interface.

shear modulus. Though this expression is approximate, in all analyses β is proportional to $\sqrt{\frac{G_m}{E_f}}$.

The shear stress given by equation 4-23 will be the smaller of the strength of the fiber-matrix interface in shear, or the shear yield stress of the matrix. These two stresses, along with relaxation mechanisms discussed in section 2.4.3, control the matrix-fiber load transfer.

4.9.3.2 Discussion of the Thermal Cycling Strain Response of Uncoated- and Coated-Al_2O_3 Fiber Composites Comparing the thermal strain versus temperature schematic in Figure 93a with the experimental thermal expansion plots of the 7-vol.% NiAl-(Saphikon) and the 5-vol.% NiAl-(Ni-Al_2O_3) composites shown in Figures 78 and 81, indicates close agreement. Similarly, the 7-vol.% nickel- and niobium-coated fiber composites, shown in Figures 86 and 88, display the expected behavior during the heating half-cycle, but the cooling half-cycles deviate from ideal predictions.

Quantitative and qualitative comparisons between the strain responses of the uncoated, niobium- and nickel-coated fiber composites consist in analyzing the shift in the heating half-cycle knee temperature, the change in slope (and concavity) above the knee temperature, the hysteresis strain, the cooling half-cycle knee temperature, and the net residual strain. The data in Table 17 summarizes these quantities and the following discussion considers each in order.

Heating Half-cycle Knee Temperature: The histogram in Figure 95 illustrates a trend of increasing heating half-cycle knee temperature with increasing number of cycles for the uncoated and the nickel-coated fiber composites. Increases in the knee temperatures indicates that stress relief, coupled with plastic flow, occurs at higher temperatures for each complete cycle. This trend suggests that after one complete cycle the interfacial region has work hardened allowing larger residual tensile stresses in the matrix after cooldown. Thus higher temperatures are required to relieve the

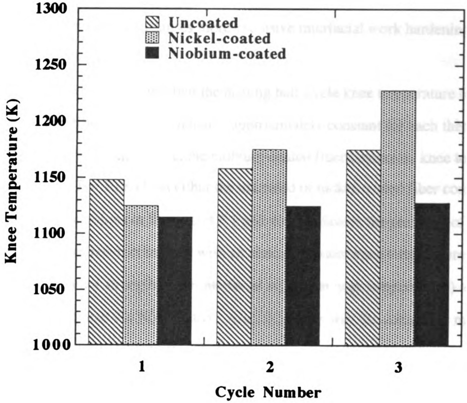

Figure 95 The heating half-cycle knee temperature versus the number of thermal cycles.

additional residual stresses and to cause the matrix to flow in compression. In addition, the relative knee temperature changes for the uncoated and nickel-coated composite is different. For instance, after the first thermal cycle, the nickel-coated fiber composite knee temperature changes ~50 K per cycle, while the uncoated fiber composite shows differences of only 10 K and 15 K. The larger knee temperature increases exhibited by the nickel-coated fiber composite suggests that the interface microstructure (dislocation density or organization), was different than the uncoated fiber composite after the first thermal cycle. This probably results when the nickel coating increases the fiber-matrix adhesion (load transfer) and causes more extensive interfacial work hardening than in the uncoated fiber composite.

Figure 95 also indicates that the heating half-cycle knee temperature for the niobium-coated fiber composite remains approximately constant for each thermal cycle. Also, after the first thermal cycle, the niobium-coated fiber composite knee temperature is slightly lower ($\Delta T = 30$ K) than either the uncoated or nickel-coated fiber composites. The previous discussions in Sections 4.5.1 and 4.8.1 indicates the presence of niobium at the interface. This result combined with an almost constant knee temperature suggests the niobium does not strengthen the interfacial region (at high temperatures) and has a lower yield stress than the NiAl matrix. Also, it appears that the composite matrix shear yield stress. Unfortunately, no information concerning the locus of failure can be gleaned from dilatometry measurements.

In contrast to the uncoated, nickel-, and niobium-coated fiber composite results, the thermal response of the titanium-coated fiber composites did not show a knee in the heating half-cycle. Several possible reasons responsible for this behavior include a poor fiber-matrix bonding (once the mechanical clamping stresses have been relieved), a high interfacial yield strength, or the occurrence of interfacial damage. The increased surface roughness and the expected Ti-Al_2O_3 and Ti-NiAl reactions, along with the visual observations that the composites showed severe transverse cracking and brittleness after thermal cycling, provide indirect evidence of good the fiber-matrix adhesion. Additionally, an average CTE of approximately 13 x 10^{-6} K^{-1}, comparable to the average ROM value (approximately 13.5 x 10^{-6} K^{-1}), suggests that significant matrix-fiber load transfer is occurring throughout the temperature regime. This result is in slight disagreement with the calculated instantaneous CTEs shown in Figures 91 and 92 which indicate, on average, agreement with ROM values at low temperatures, but show deviations toward the monolithic NiAl values at temperatures as low as 700 K. The reasons for the missing are unclear at this time.

Change in Slope: Another important quantity calculated from the heating half-cycles is the average CTE (the slope) above the knee temperature. This CTE provides a method for qualitatively assessing differences in fiber-matrix adhesion. The uncoated fiber composite shows only a small reduction in slope (ΔCTE = 0.5 x 10^{-6} K^{-1}) above the knee temperature. Though the CTE is slightly reduced, it is still above the predicted average ROM value of ~13.5 x 10^{-6} K^{-1}. This implies that matrix-fiber load transfer takes place, but not in an amount sufficient enough to cause a large amount of matrix yielding (indicated by a larger change in slope). This implication of a small amount of fiber-matrix bonding is consistent with a mechanical bond (it may be possible that hoop stresses may not be exhausted) and/or a weak chemical bond.

The histogram in Figure 96 illustrates that the average CTE of the nickel- and niobium-coated fiber composites decreases as the cycle number increases. The fiduciary line representing the average CTE of Al_2O_3 the values are close to the average CTE of the fibers (8.8 x 10^{-6} K^{-1}) and substantially lower than the values reported in Table 17 for the uncoated fiber composite. These results indicate effective matrix-fiber load transfer in the coated fiber composites, suggesting a high level of fiber-matrix adhesion. This increased adhesion causes deformation processes which work harden the interface region. Progressive increases in the interfacial stresses continue until the stored energy, combined with the applied temperature, activate stress relaxation processes (listed in Table 7) which reduce the load transfer effectiveness. These relaxation processes also caused a mild concavity in the nickel- and niobium-coated fiber composites, not observed in the uncoated fiber composites. This concavity (which has a negative slope) is an indication of activated creep.

Hysteresis Strain: From the data in Table 17 the nickel-coated fiber composite has the largest hysteresis strain, while the niobium- and titanium-coated fiber composites have intermediate values and the uncoated fiber composite the smallest. The hysteresis strain is large for composites showing large changes in slope above the heating cycle knee temperature. The titanium-coated fiber is the exception to this statement since no heating half-cycle knee temperature was observed, but for all cycles showed a hysteresis strain. This suggests that, though no knee was seen, a significant amount of deformation (i.e., if no deformation occurs, the composite behaves like a monolithic material) occurred during the heating half-cycle. From the amount of hysteresis strain, it appears that the titanium-coated fiber composite has a high level of fiber-matrix adhesion.

Cooling Half-cycle Knee Temperature: Similar to the heating half-cycle, a complex thermal response occurs during the cooling half-cycle. In the case of uncoated, titanium- and niobium-coated fiber composites following an initially linear response (elastic unloading) a knee appears. As described in section 4.9.3.1, this knee represents the temperature where the matrix tensile stresses accumulate and rise above the yield stress of the matrix. The knee temperatures shown in Table 17 do not indicate a consistent trend, but all of the knee temperatures are in the temperature range of 940 to 1050 K except for the fourth cycle of the 5-vol.% NiAl-Al_2O_3 composite (1101 K). The absence of a trend may partially be the result of noisy data, and missing or diffuse knees. These observations suggest that the fiber coatings do not alter the interfacial yield stress of the composites.

In contrast to the cooling half-cycle of the niobium- and titanium-coated fiber composites, the thermal response of the nickel-coated fiber composite remains linear with

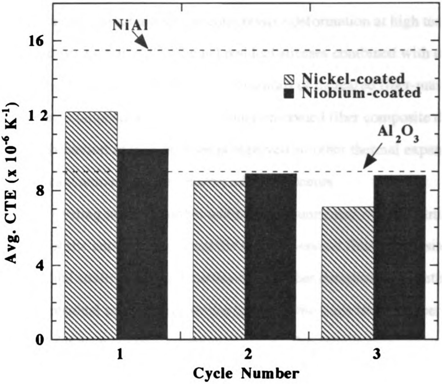

Figure 96 The average CTE as a function of thermal cycle.

no knee being observed. The absence of the knee indicates that the interfacial stresses accumulated above the knee are not fully recovered.

Net Residual Compressive Strain, $\Delta\varepsilon_p$: Residual compressive strains result when the high-temperature compressive stresses generate compressive strains which are only partially recovered when the composite is cooled. The dimensional change of the composites is referred to as strain ratchetting. All of the coated fiber composites exhibited a net residual plastic strain after the first thermal cycle, while the uncoated fiber composite showed no length changes. This result indicates that the coated fiber composites generated a larger amount of compressive deformation at high temperatures than the uncoated fiber composite. The net residual stresses combined with the change in slope above the heating half-cycle knee are indications of increased fiber-matrix adhesion for the coated fiber composites. Again, the titanium-coated fiber composite does not follow the same behavior: though no knee is observed all other thermal expansion data indicate a significant amount of fiber-matrix adhesion occurs.

Repeated cycling results in either additional accumulated residual strain (nickel-coated fiber composite and to some extent the niobium-coated fiber composite) or in a diminishing residual strain (as in the titanium-coated fiber composite). Continued accumulation of residual compressive strains indicates the same level of fiber-matrix adhesion persists for each complete thermal cycle and that plastic shakedown is not occurring. On the other hand, the titanium-coated fiber composites shows a consistent decrease in residual stress as the number of cycles increases. The accumulation and subsequent reduction in net residual stress is probably related to damage mechanisms occurring at the interface and indicates that plastic shakedown is occurring.

From the above discussion of thermal expansion parameters it is apparent that the nickel, niobium, and titanium coatings increase the matrix-fiber load transfer at high temperatures when compared to the uncoated fibers. (Mechanical clamping stresses appear to dominate the load transfer at the low temperatures.) Furthermore, it appears that the nickel and niobium coatings cause a significant amount deformation to occur above the knee resulting in a strain ratchetting behavior. In contrast to this behavior, the uncoated fiber composite showed a knee, which implies fiber-matrix adhesion causing interfacial yielding, but not to the extent observed in the nickel- and niobium-coated fiber composites. The behavior of the titanium-coated fiber composite is distinctive, though it appears but it appears that adequate fiber-matrix adhesion is present (as evidenced by the CTE obeying the ROM predictions), to produce residual strain accumulation. This may be a result of the accumulation of interfacial damage during thermal cycling.

4.9.3.3 Discussion of the Effects of the Fiber Coatings on the Instantaneous CTE

The instantaneous CTE of unidirectional composites is governed by the fiber volume fraction, along with the mechanical properties, and the thermal properties of the composite constituents. Below the knee temperature elastic expansion occurs and the instantaneous composite CTE should be bounded by the CTEs of the fiber and matrix in this temperature regime. Above the knee temperature, where plastic deformations occurs, these bounds may be violated. Violations of this type were observed in the instantaneous CTE plots of the nickel- and niobium-coated fiber composites shown in Figures 87 and 89. To demonstrate some of the key material variables responsible for this effect, a simple micromechanical model based on an inelastic rule-of-mixtures formulation is now described [Urquhart, 1993]. (More sophisticated numerical methods have also been used to determine the instantaneous thermal response; however, the same qualitative results are obtained [Paley, 1992; Pindera, 1993].)

The analyses by Urquhart et al. assumes that the matrix phase behaves in an elastoplastic (with linear work hardening) manner with the moduli of both constituents invariant with temperature [Urquhart, 1993]. The expression for the instantaneous CTE of the composite can be determined by starting from total the composite strain, which is a sum of the fiber thermal, ε_t, and mechanical strains, $\varepsilon_{\mathrm{mechanical}}$, where

$$\varepsilon_t = \alpha_f \Delta T, \qquad 4\text{-}25$$

and

$$\varepsilon_{\text{mechanical}} = \frac{\sigma_1}{E_f}, \qquad 4\text{-}26$$

and σ_1 is the longitudinal fiber stress (equivalent to the axial composite stress) and E_f is the fiber modulus. The instantaneous CTE can then be written as

$$\alpha^{\text{inst.}}(T,\sigma_1) = \alpha_f + \frac{\partial}{\partial T}\left(\frac{1}{E_f}\right)\sigma_1 + \frac{1}{E_f}\left(\frac{d\sigma_1}{dT}\right), \qquad 4\text{-}27$$

where

$$\frac{d\sigma_1}{dT} = \frac{(\alpha_m - \alpha_f) + \frac{\partial \overline{\sigma_m}}{\partial T}\left(\frac{E_m - E_m^*}{E_m E_m^*}\right) - \sigma_1 \frac{\partial}{\partial T}\left(\frac{1}{E_f} + \frac{1}{E_m}\frac{V_f}{V_m}\right)}{\frac{1}{E_f} + \frac{1}{E_m^*}\frac{V_f}{V_m}} \qquad 4\text{-}28$$

and σ_1 is the longitudinal fiber stress, α_m is the CTE of the matrix, α_f is the CTE of the fiber, E_m is the modulus of the matrix, and E_m^* is the hardening slope (modulus of the matrix above the yield point). Furthermore, $\overline{\sigma_m}$ is the current matrix yield stress, which is a function temperature and matrix plastic strain. Now assuming that the elastic moduli of the fiber and matrix are independent of temperature (which is not too bad of an assumption for Al_2O_3 or NiAl) and letting

$$\frac{\partial}{\partial T}\left(\frac{1}{E_f}\right) \text{ and } \frac{\partial}{\partial T}\left(\frac{1}{E_m}\right) \rightarrow 0$$

the longitudinal composite CTE is

$$\alpha^{\text{inst.}} = \alpha_f + \left(\frac{1}{E_f}\right)\left(\frac{V_f}{V_m}\right)\frac{\partial \overline{\sigma_m}}{\partial T}. \qquad 4\text{-}29$$

This expression indicates that α^{inst} can be less than the CTE of the fiber since $\frac{\partial \overline{\sigma_m}}{\partial T} < 0$.

From this analysis it is clear that there are several material factors influencing composite instantaneous CTE. Clearly the effect of the matrix yield stress and the rate of change of yield stress with temperature plays a major role in the high-temperature thermal response of a composite. For example, if the interfacial stress reaches the matrix yield stress at a temperature corresponding to a large gradient in yield stress distribution (intermediate to high temperatures for NiAl), there will be a drastic change in the thermal response. If, however, the interfacial stress reaches the matrix yield stress at a temperature corresponding to a smaller gradient, the change in thermal response will be more subtle. From Figure 4 the NiAl yield stress at temperatures near the reported knee temperature (1000 -1200 K) is less than 100 MPa, with small gradients.

By comparing the instantaneous CTE for the composites with that of the matrix, fiber, and ROM calculations, one can differentiate changes in composite behavior due to mechanical effects, such as matrix inelasticity and fiber debonding. Some of the similarities and differences among the uncoated and coated-fiber composites's heating half-cycle instantaneous CTE behaviors are summarized in Table 18. The information contained in Table 18 shows that all of the composites obeyed —at least on average— the ROM predictions at low temperatures where the yield strength and modulus of the matrix are high. In addition, the ΔCTE mismatch induced clamping stresses are large in this temperature regime.

Comparing the plots of the uncoated and nickel-coated fiber composite instantaneous CTEs shown in Figures 84 and 87, respectively, indicate subtle but distinct differences. For instance, both composites show a deviation toward the monolithic NiAl CTE. This deviation indicates a release of the ΔCTE mismatch induced clamping stresses below the knee temperature. This behavior implies poor fiber-matrix bonding, since mechanical bond controls the load transfer process. Closer inspections of Figures

84 and 87 indicate the approach of the deviations is quite different in the two composite systems. In the uncoated fiber composite system, the instantaneous CTE gradually deviates —starting at temperatures as low as 600 K— from ROM values. In contrast, the nickel-coated fiber composite closely mimics the ROM predictions until ~ 1000 K, when sharp deviations toward the NiAl CTE are observed. The differences in the deviations, suggest that the nickel-coated fiber bonds more strongly with the matrix than the uncoated fiber composite.

In addition to these comments, the maximum instantaneous CTEs are different. For instance, the uncoated fiber composite has an instantaneous CTE slightly greater than the NiAl CTE, while the nickel-coated fiber composite has an instantaneous CTE equal to or just below the NiAl CTE. This discrepancy may be caused by a slight error in calibration, or may be real and be caused by differing degrees of fiber-matrix adhesion. If the latter is the case, this data indicates that the nickel coating provides a better fiber-matrix bond than the uncoated fiber.

In contrast, the niobium-coated fiber composite shows no deviation toward NiAl CTEs and, hence, indicates the presence of strong fiber-matrix bonding. The titanium-coated fiber composites showed no sharp deviations indicating of the release of clamping stresses, but did, in some cases, show a gradual CTE rise toward the NiAl values. (Note that most numerical or analytical studies do not predict a deviation toward the matrix CTE since perfect fiber-matrix bonding is assumed.)

The knee in the strain versus temperature curve represents a transition from ROM to fiber dominated behavior. This transition corresponds to a temperature regime where the matrix yield strength and modulus are low. These changes in matrix mechanical properties, combined with the ΔCTE induced stresses, produce instantaneous CTEs that can violate the constituent material bonds. As the information in Table 18 indicates, all of the composites except for the titanium-coated fiber composites dropped below the ROM values after passing through the knee temperature.

Table 17 Summary of heating half-cycle instantaneous CTE observations.

Fiber Coating	ROM Values at Low Temperatures	Deviation Toward NiAl CTE before Knee Temperature	Violation of ROM and Al_2O_3 Fiber Bounds		Average Slope after the Knee Temperature * (x 10^{-6} K^{-1})
			ROM	Al_2O_3 Fiber	
Uncoated	yes	yes, sharp	yes	no	-0.025
Nickel	yes	yes, sharp	yes	yes	-0.059
Niobium	yes	no	yes	yes	-0.062
Titanium	yes	inconsistent, gradual	no	no	—

*indicates average of the second and third cycles.

In addition, the nickel- and niobium-coated fiber composite instantaneous CTE dropped below the Al_2O_3 CTE. The violation of these bounds indicates persistent fiber-matrix adhesion above the knee temperature, and that the interfacial yield stress has been exceeded (recall section 4.7.3). (Note that these results suggest that the locus of failure occurs in the matrix and not at the fiber-matrix interface. Since dilatometry measures average properties, some of the local properties may be smoothed out and a definitive determination of the locus of failure may be impossible to locate.)

Though not explicitly expressed in the instantaneous CTE formalism shown above, the effect of matrix work hardening on the composite thermal response also affects the shape of the instantaneous CTE curve. For instance, a low work hardening rate material flows easily upon yielding (assuming perfect fiber-matrix bonding). The easy flow properties cause the instantaneous CTE to decrease more rapidly. Using the second and third cycle instantaneous CTEs, the average slopes of the linear region immediately following the knee temperature are recorded in Table 18. The reason that the first cycle was not included in the average was that the first cycle slopes for the uncoated, nickel-, and niobium-coated composites were approximately the same, $-0.05 \times 10^{-6} K^{-1}$.

In the case of the uncoated fiber composite, the steepness of the slope decreased significantly after the first cycle. The change in slope after the first cycle suggests that, assuming perfect fiber-matrix bonding, the interface was strain hardened during the first cycle, such that the work hardening rate increased for the second and third cycles. Since the uncoated fiber composite probably has poor fiber-matrix bonding, the change in slope probably corresponds to inadequate loading of the fiber by the matrix. In this case, the slope would no longer be an indication of the interfacial work hardening rate. The exact cause of the change in slope is impossible to determine, but in all likelihood is a combination of several factors including, fiber-matrix decohesion, matrix work hardening, and interfacial damage accumulation.

The instantaneous CTE slopes of the nickel- and niobium-coated fiber composites showed a consistent value of -0.06 x 10^{-6} K^{-1}. These results suggest that the interfacial mechanical properties are relatively insensitive to the number of thermal cycle (at least for the number tested) and that the interfacial bond strength persists. Furthermore, since the fiber-matrix adhesion in these composites appears good, the steepness of the slope implies that the interfacial work hardening rate is low. The low work hardening rate is consistent with the high temperature behavior of NiAl and other bcc materials [Bowman, 1992]. The addition of nickel and niobium to the fibers, therefore, does not appear to alter the work hardening rate of the matrix near the interface. Since the attainment of perfect fiber-matrix bonding in the uncoated fiber composite is doubtful, a direct comparison among the slopes of the coated and uncoated composites is unrealizable.

As a final note on the instantaneous CTE curves, the "double dip" behavior seen in most of the instantaneous CTEs is believed to be real and not an experimental artifact since it was reproducible in the same and different types of composites. This type of behavior could represent the dynamic behavior occuring between the work hardening and relaxation processes (such as strain hardening followed by dynamic recrystallization).

4.9.4 Thermal Expansion Behavior of NiAl-(Uncoated- and Coated-Saphikon) Composites at Temperatures Near the Knee Temperature The previous composite thermal strain versus temperature plots exhibited a hysteresis strain between the heating and cooling half-cycle curves and, except for the titanium-coated fiber composite results, a knee in the heating half-cycle plots. If the knee temperature corresponds to the exhaustion of residual stresses and the onset of compressive plastic matrix deformation, then heating the composite to a maximum knee near (or below) the knee temperature and cooling should not produce a hysteresis strain (or net residual strain) between the heating and cooling half-cycles.

To test this assertion, the composite thermal expansion behaviors were investigated to maximum temperatures near the previously observed knee temperatures.

Since the Ti-coated fibers showed no heating half-cycle knee, a value of ~850 K, which appeared to correspond to an elastic thermal response, was chosen as the maximum temperature. Figure 97 shows plots of the axial strain versus temperature for 7-vol.% uncoated and coated fiber NiAl composites. In all cases, a small amount of residual strain was observed, but the amount of hysteresis strain was negligible. These results imply that the application of nickel, niobium, or titanium coatings to the fibers do not significantly alter the elastic expansion/compression behavior of the composites. These results also provide additional evidence that mechanical clamping stresses dominate the low-temperature load transfer process.

4.9.5 Discussion of The Effects of the Heating Rate on the Thermal Expansion Behavior of Uncoated, Niobium- and Nickel-Coated Saphikon Composites

Another important experimental parameter that potentially alters the composite strain response is the heating or cooling rate. Though the general form of the plots should be independent of the heating rate, the heating rate represents a kinetic component to the strain response and affects the temperature at which the knee occurs [Garmong, 1974]. The plots in Figure 98 show the influence of the heating rate (2.54 K-min.$^{-1}$, 3.75 K-min.$^{-1}$, and 4.54 K-min.$^{-1}$) on the composite strain response of uncoated- and coated-fiber composites, while Table 17 summarizes the thermal expansion data. (The cooling data was acquired when the furnace was turned off. This experimental arrangement resulted in an average cooling rate of 3.35 K-min.$^{-1}$. Also, the heating rate determines the maximum attainable temperature since the furnace is power limited.)

Comparisons among theoretical predictions indicate disagreement of the effect(s) of heating rate on the knee temperature [Garmong, 1974; Dutta, 1993]. For instance, Garmong predicts (and measures) that the position of the knee in the heating half-cycle shifts to higher temperatures with slower heating rates, while Dutta et al. predict (and measure) a shift to lower temperatures. This disagreement illustrates that the model and the composite system determine the results of the study, and that the shift in knee

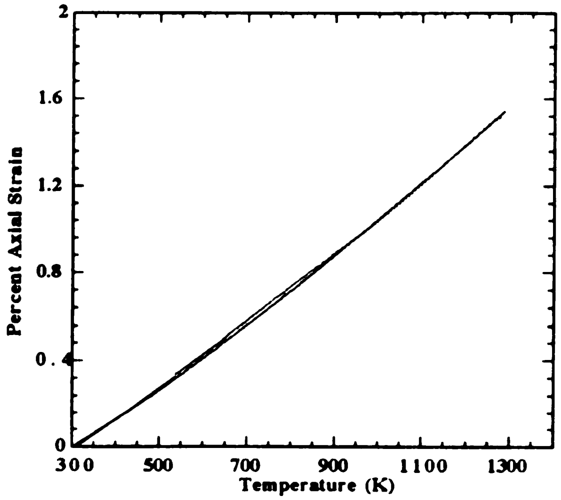

(a)

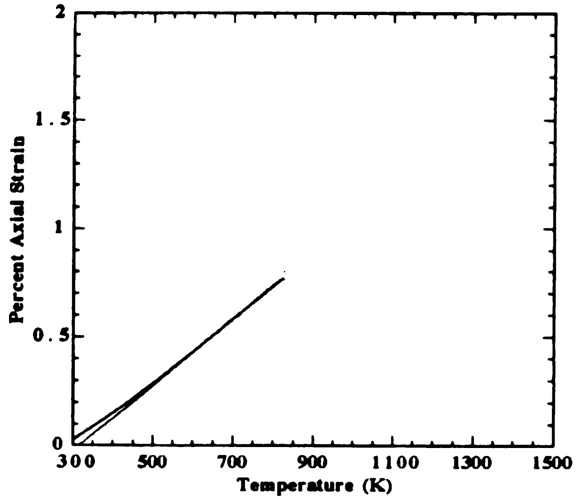

(b)

Figure 97 The strain of (a) uncoated, (b) Ti, (c) Ni, and (d) Nb-coated fiber composites.

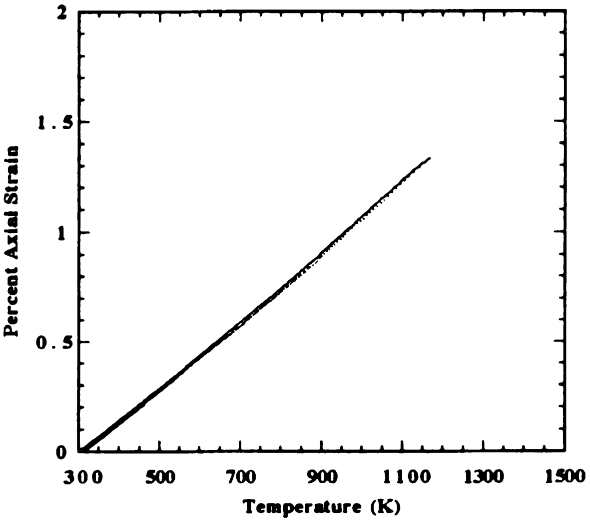

(c)

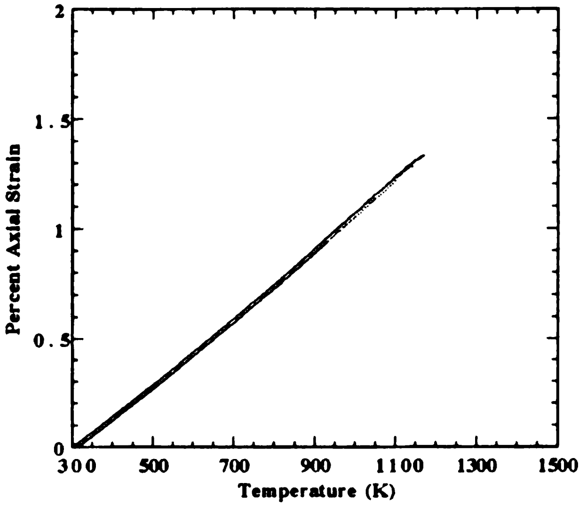

(d)

Figure 97 (con't).

temperature can not *a priori* be determined. In general, however, faster heating rates allow less time per temperature increment for occurrence of thermally activated processes, such as diffusion and creep . This indicates that increasing the heating rate would shift the knee to higher temperatures.

Similar to the expression for the interfacial shear strength given by equation 4-23, the rate dependent material properties of the interface should also influence the interfacial shear stress. Once plastic flow begins, the shear stress, τ, at the fiber-matrix interface is described by[1],

$$\tau = K_{\tau}\left(\beta' \dot{\varepsilon}_{\mathrm{matrix}}\right)^{m}\left(\frac{x}{d_f}\right)^{m}, \qquad 4\text{-}30$$

where K_{τ} is a measure of the intrinsic matrix shear stress (which depends implicitly on the amount of strain provided that work hardening occurs), β' is a proportionality constant that is a function of the fiber volume fraction, $\dot{\varepsilon}$ is the matrix tensile strain rate, m is the strain rate sensitivity of the matrix, x is a distance along the fiber, and d_f is the fiber diameter [Kelly, 1972]. Equation 4-30 indicates that the shear stress increases when the matrix strain rate sensitivity increases. Furthermore, this expression shows that when m is small (near zero), the shear stress is constant along the fiber length and equal to the matrix yield strength. Similarly, the tensile stress carried by the fiber, σ_f, is a function of the matrix strain rate sensitivity and is given by

$$\sigma_f = \left(\frac{4K_{\tau}}{m+1}\right)\left(\beta' \dot{\varepsilon}_{\mathrm{matrix}}\right)^{m}\left[\left(\frac{1}{2d_f}\right)^{m+1} - \left(\frac{x}{d_f}\right)^{m+1}\right], \qquad 4\text{-}31$$

where the symbols carry the same meaning as above. As might be expected, the fiber tensile stress builds up most rapidly in strain-rate sensitive matrices (when m is large the

---

[1] This description of the rate dependent properties compliments the discussion of the work hardening rate in section 4.9.3.3.

load transfer is more effective). Likewise, the fiber is loaded to higher stress levels with increases in matrix strain rate.

For a given material, the strain rate sensitivity depends on a number of parameters including grain size, composition, and temperature. Generally, increasing the strain rate increases the yield stress, the flow stress, and the work hardening rate. In addition, increasing the temperature increases the strain rate sensitivity of the material. The average strain rates of the composites can be estimated from

$$\dot{\varepsilon} = \alpha \bullet \text{Heating Rate} \ . \qquad 4\text{-}32$$

Using this expression and the average CTEs listed in Table 17 for each heating rate, the composite strain rates range from $2 \times 10^{-3}\ s^{-1}$ to $4 \times 10^{-3}\ s^{-1}$. Thus, though the heating rates are quite different, the effects on the composite strain rate are relatively small.

Two cycles of the thermal response of a 7-vol.% NiAl-(Al_2O_3) fiber composite are shown in Figure 98a and resemble the plots shown in Figure 83. Though no apparent knee is present in the first cycle, the second cycle shows a knee at ~1230 K. Both cycles show a small hysteresis strain. The thermal expansion curves for a 7-vol.% NiAl-(Nb-Al_2O_3) composite are shown in Figure 98b. The plots are similar to those reported in Figure 88, however, these plots show a consistent trend of decreasing hysteresis and compressive residual strain with increasing cycle. These resuslts suggest the occurence of plastic shakedown. No trend(s) are discernible for the 7-vol.% NiAl-(Ni-Al_2O_3) fiber composite plots shown in Figure 98c.

The histogram in Figure 99 shows that for the uncoated and niobium-coated fiber composites, the knee temperature increases slightly as the heating rate increases. In performing the heating rate experiments, the same composite was used for each heating rate. Therefore, the composites not only experience different heating rates, but are also thermally cycled. The shifts in the knee temperatures are therefore a combination of

Table 18 Thermal expansion parameters for composites tested at different heating rates.

7-vol.% NiAl-Al_2O_3 Composite

Cycle #	Heating Rate (K/min.)	Knee Temperature Heating (K)	Knee Temperature Cooling (K)	Hysteresis Strain	$\Delta\varepsilon_p$	Avg. CTE < T_{knee}	Avg. CTE > T_{knee}
1	2.54	-	-	-0.0350	-0.0439	12.8	12.8
2	3.75	1230 ± 5	924 ± 10	-0.0585	-0.0116	12.8	10.6
3	4.54	1250 ± 5	-	-0.0232	~0	13.0	10.9

7-vol.% NiAl-(Ni-Al_2O_3) Composite

Cycle #	Heating Rate (K/min.)	Knee Temperature Heating (K)	Knee Temperature Cooling (K)	Hysteresis Strain	$\Delta\varepsilon_p$	Avg. CTE < T_{knee}	Avg. CTE > T_{knee}
1	2.54	1212 ± 5	1029 ± 10	-0.1193	-0.0890		
2	3.75	1229 ± 5	924 ± 10	-0.1859	-0.1380		
3	4.54	1170 ± 5	854 ± 10	-0.0527	-0.0397		

7-vol.% NiAl-(Nb-Al_2O_3) Composite

Cycle #	Heating Rate (K/min.)	Knee Temperature Heating (K)	Knee Temperature Cooling (K)	Hysteresis Strain	$\Delta\varepsilon_p$	Avg. CTE < T_{knee}	Avg. CTE > T_{knee}
1	2.54	1191 ± 5	992 ± 10	-0.0611	-0.0370	12.3	8.6
2	3.75	1211 ± 5	1016 ± 10	-0.0407	-0.0204	12.6	10.7
3	4.54	1216 ± 5	1002 ± 10	-0.0510	-0.0102	12.7	11.2

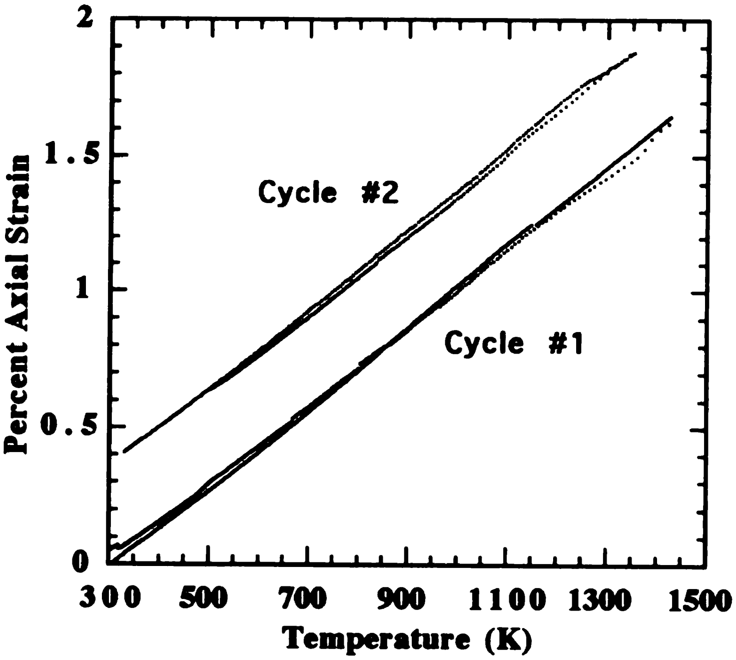

(a)

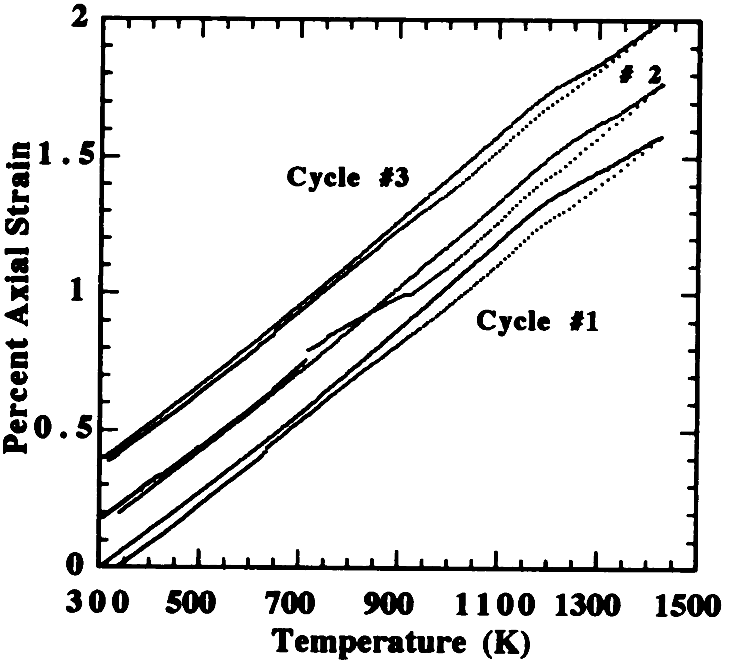

(b)

Figure 98 The strain for (a) uncoated, (b) Nb-, and (c) Ni-coated fiber composites.

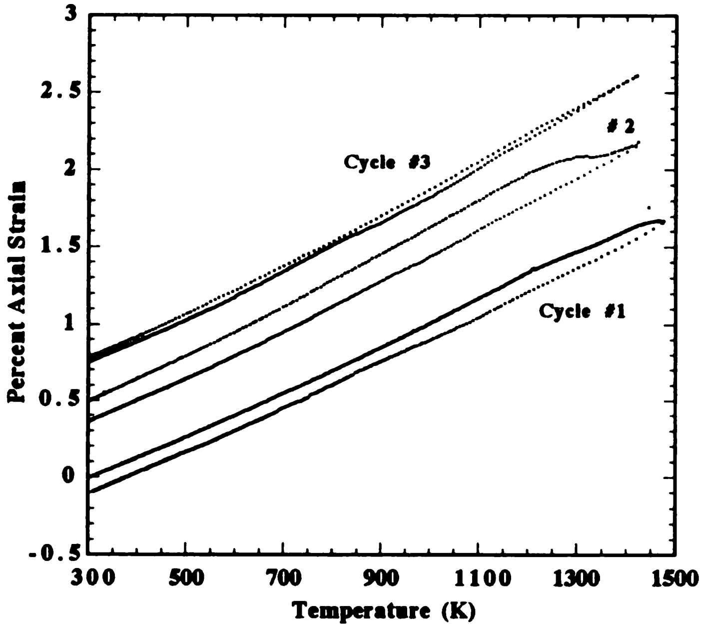

(c)

Figure 98 (cond't).

thermal cycling and changing heating rates. Comparing the second and third cycles of the niobium-coated fiber composite with the first cycle shows that the knee becomes less prominent. In addition, the average CTE above the knee temperature increases. In general, the knee temperature is relatively insensitive to the heating rates used.

The primary effect of a change in the heating rate is the amount of creep deformation (and the consequent stress relief) that can occur.

4.10 Axial Matrix Stress Analysis

Matrix and fiber residual stresses arise from differences between the fiber and matrix thermal expansion coefficients. Since these stresses affect the load carrying capacity of the composite, it is important to measure them. These stresses are limited by matrix flow to values corresponding to the von Mises stress condition. The application of nickel, titanium, and niobium fiber coatings may alter theses stresses. This section of the thesis describes a qualitative analysis procedure for calculating the temperature dependence of the matrix stress using thermal expansion curves [Masutti, 1990]. In this analysis, which assumes no sliding at the fiber interface (perfect bonding) and no yielding of the fibers, the strain of the composite is assumed to be equal to the strain of the fibers, ε_f. The fiber expansion is expressed as a sum of the thermal and mechanical strains,

$$\varepsilon_f = \alpha_f \Delta T + \frac{1}{E_f}\left[\sigma_z^f - 2V_f \sigma_r^f\right], \qquad 4\text{-}33$$

where α_f, E_f, and V_f are the thermal expansion coefficient, Young's modulus, and Poisson's ratio of the fibers, respectively. σ_z^f and σ_r^f are the fiber axial and radial stresses, respectively, and are assumed uniform throughout the fibers.

In the absence of an external axial load, ROM analysis gives

$$\sigma_z^f V_f = -\langle \sigma_z^m \rangle V_m, \qquad 4\text{-}34$$

where $\langle \sigma_z^m \rangle$ is the average of the axial stresses in the matrix and V_f and V_m are the volume fraction of the fibers and matrix. The distribution of the stress components in the vicinity of the fiber-matrix interface during yielding of the matrix has been calculated by Yano et al. [Yano, 1988]. These calculations indicate that (i) σ_r^f has the same sign as σ_z^f and is on the order of 0.1 σ_z^f and (ii) although large gradients of the stress components σ_z^m, σ_r^f, and σ_θ^f are observed in the vicinity of the interface, the distribution of the equivalent yield stress is nearly uniform and not very different from the absolute value of $\langle \sigma_z^m \rangle$. Thus in this calculation, the radial stress may be neglected. Combining equations 4-33 and 4-34, the average axial matrix stress can be calculated from

$$\langle \sigma_z^m \rangle = \frac{V_f}{V_m} E_f \left(\alpha_f \Delta T - \varepsilon_f \right), \qquad 4\text{-}35$$

where $E_f = 414$ GPa, $\alpha_f = (5.96 + 0.0039T) \times 10^{-6} K^{-1}$.

After meeting the requirements of the assumptions, the most critical parameter to be determined is the initial (room temperature) matrix stress. In general, the initial thermal stress in the composite is deduced by heating the composite to a high temperature ($\sim 0.8\ T_m$), where the matrix stress becomes small and the absolute values of the flow stresses are equivalent in tension and compression. Extrapolating the fiber thermal expansion from the maximum temperature to room temperature allows the fiber thermal strain, ε_f, to be determined. This strain is then used in equation 4-35 to determine the initial matrix stress. In the present cases (see Figures 83, 86, and 88), the maximum temperature of 1450 K corresponds to approximately 70% of the melting point of NiAl, which may not be high enough to completely minimize interfacial stresses. Also, the large difference in thermal response at the highest temperatures (large slope differences in

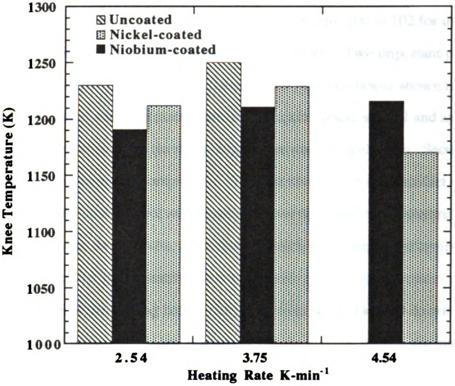

Figure 100 The knee temperature for uncoated, Ni-, and Nb-coated fiber composites.

the heating and cooling parts of the curves) for the nickel- and niobium-coated fiber composites makes an absolute determination of the initial matrix stress difficult to determine. Furthermore, in the uncoated fiber composite case, the condition of perfect fiber-matrix bonding is probably not realized.

These deficiencies make quantitative calculations impractical; however, the calculations can be performed to establish reasonable bounds on the stress to make relative comparisons among the composites. To make qualitative comparisons, the additional requirement of zero matrix stress at the highest temperature was imposed.

The results of these calculations are shown in Figure 100 to 102 for uncoated, nickel-, and niobium-coated fiber composites, respectively. Two important points are notable concerning the matrix stress of the uncoated fiber composite shown in Figure 100. First, the initial and final matrix stresses are approximately equal and appear reasonable when compared to the room temperature matrix yield stress. Secondly, the matrix stress never becomes compressive. The last observation is an artifact of the additional imposed constraint of zero matrix stress at the highest temperature.

In contrast to these results, the nickel- and niobium-coated fiber composites show a substantially smaller initial matrix stress and sizable compressive stresses. (Note that the poor qualities of the cooling half-cycles result from noisy data and do not necessarily reflect physical phenomena.) Also, because of the net residual strains, the matrix stress at the end of a cycle is always greater than the initial stress of the next cycle. Furthermore, the initial stress of the second cycle does not equal the matrix stress of the end of the first cycle. This trend is also seen in the data reported by Masutti et al. and is a result of the difficulty of determining the initial matrix stress [Masutti, 1990]. The large differences seen between the initial and final matrix stresses are evidence of accumulated plastic strain.

Figures 101 and 102 indicate that the maximum compressive stress for the nickel- and niobium-coated fiber composites is approximately 40 MPa, which are approximately

50% of the NiAl yield stress. (Note that this represents a maximum compressive stress). The creep behavior in NiAl follows that for metals and alloys and has been briefly summarized in section 2.3.1.2 and Table 3. Furthermore, at 1175 K applied stresses of 30 MPa lead to strain rates among 10^{-5} and 10^{-4} s^{-1} [Noebe, 1993]. Comparing the calculated stress of 40 MPa with the creep strain rates of 10^{-5} at 30 MPa, suggest that, at 1200-1450 K a significant amount of composite creep strain can occur during thermal expansion of the nickel- and niobium-coated fiber composites.

These plots also provide a qualitative indication of the temperature range for the transition from tensile to compressive matrix stress (~600 - 800 K). This temperature range is well below the measured knee temperatures, but is suggestive of the behavior shown in Figure 302. The last major distinction among the stress temperature curves is the exhibition of compressive stresses during the cooling half-cycle for the niobium-coated fiber composite. This behavior is a consequence of the mild concavity in the cooling half-cycles of the thermal strain versus temperature plots seen in Figure 296. In contrast, cooling half-cycles of the uncoated and nickel-coated fiber composites contract in a linear manner. The concavity represents the occurrence of creep processes and implies that the niobium coating produces more creep strain than either the uncoated fiber or nickel-coated fiber.

4.11 Summary of the Results and Discussions

The results in this thesis serve as a step toward understanding the effects of employing titanium, nickel, and niobium fiber coatings to alter the fiber-matrix interfacial behavior in NiAl-Al_2O_3 composites. As described in section 1.3 and schematically illustrated in Figure 23 the experimental approach consisted of investigating the as-

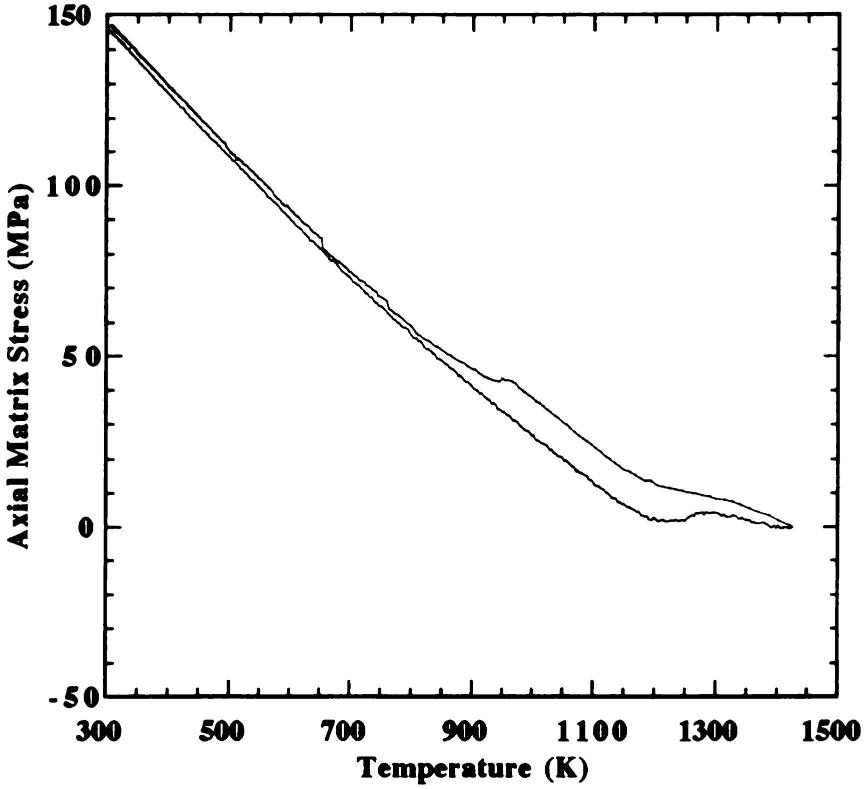

Figure 100 Matrix stress for the a 7-vol.% NiAl-Saphikon composite.

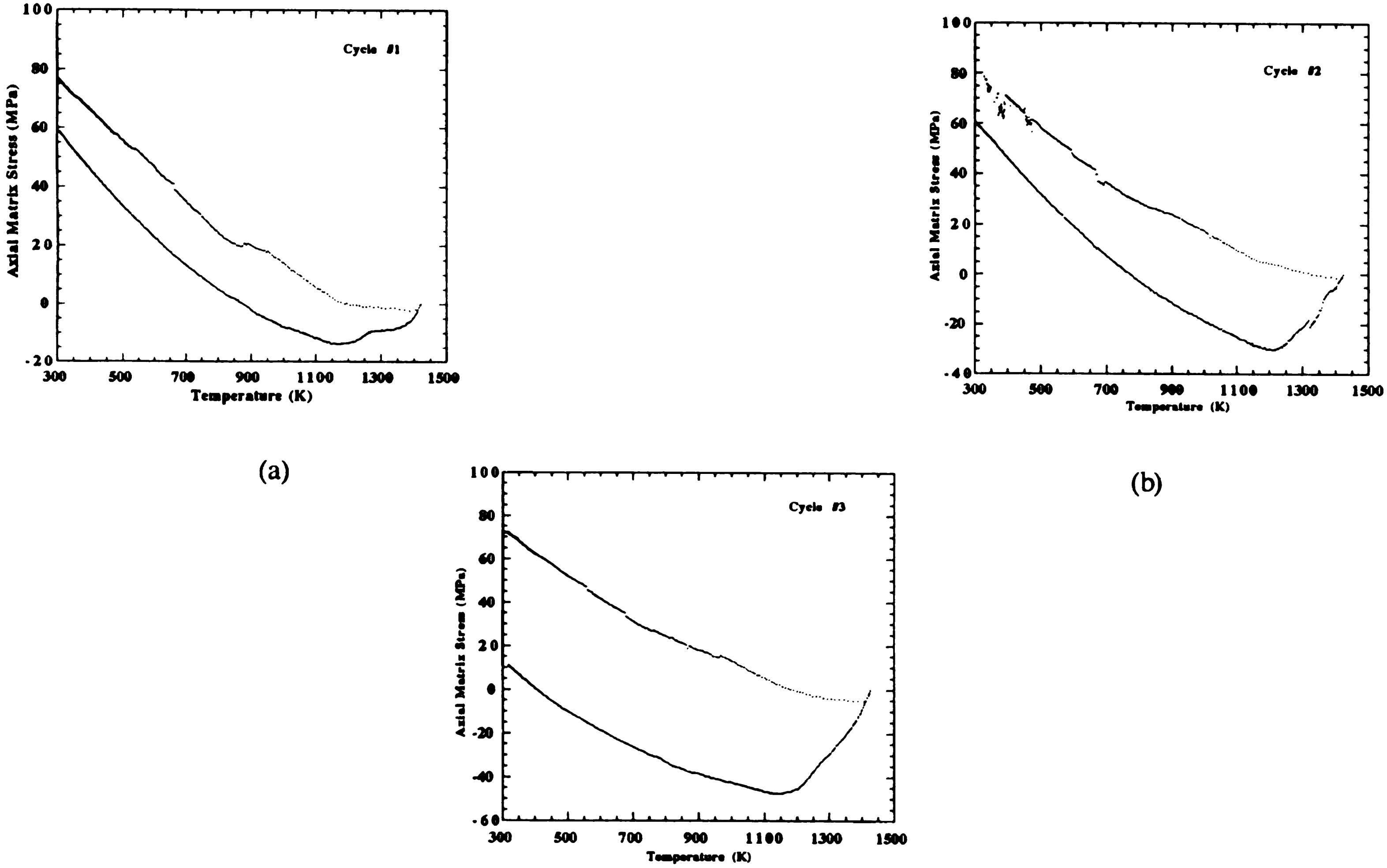

(a)

(b)

(c)

Figure 101 Matrix stress for a Ni-coated fiber composite.

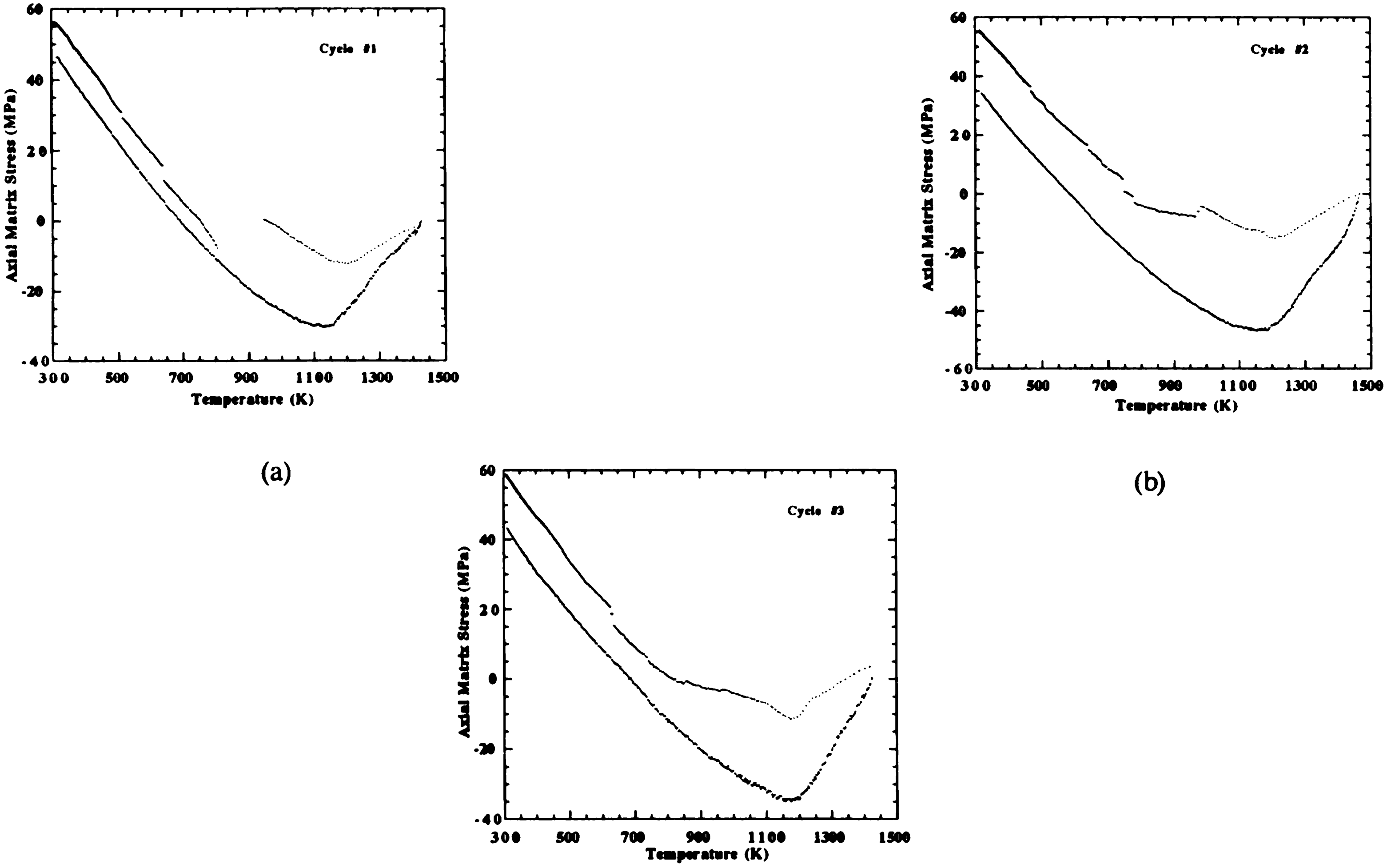

(a)

(b)

(c)

Figure 102 Matrix stress for a Nb-coated fiber composite.

consolidated fiber properties, the thermal cycling behavior of the composites, and the thermal expansion behavior of the composites.

The conclusions of these studies are sumarized in Table 19. These results indicate that the fiber coatings (nickel, niobium, and titanium) produce considerable changes in the fiber and composite properties. In particular, the as-composited fiber- fragment aspect ratio distribution of the niobium-coated fibers and the uncoated fibers showed approximately equal numbers of small, intermediate, and large ratios. In contrast, the titanium- and nickel-coated fiber-fragment aspect ratios were skewed to the small ratios.

Dilatometry has been shown to be very effective in providing baseline quantitative and qualitative data for understanding the thermal response of NiAl-Saphikon composites. The instantaneous CTE of the composites were found to be sensitive to plastic deformation processes and fiber-matrix interfacial bonding. Dilatometry can, therefore, be used to indicate if the fiber-matrix interfacial bonds are generally strong or weak. The fiber coatings affected the thermal expansion behavior of the compoistes quite differently. All of the coatings increased the fiber-matrix adhesion; however, the different high-temperature deformation processes in the nickel-, niobium-, and titanium-coated composites were clearly different.

Table 19 Summary of the structure-property relationships.

	Composite Property (Relative to An Uncoated Fiber Composite)							
Fiber Coating	Average Fiber Aspect Ratio (4.7.2)	Thermal Racheting (4.9.3.2)	Plastic Shakedown (4.9.3.2)	Fiber Surface Roughness (4.4)	Avg. CTE Above the Knee Temperature (4.9.3.2)	Interfacial Work Hardening Rate (4.9.3.2)	Interfacial Ductility (4.8.3)	Fiber-Matrix Adhesion (4.9.3)
Nickel	Less	Yes	No	Greater	Less	Less	Unaffected	Increases
Niobium	Same	Yes	???	Greater	Less	Less	Increases	Increases
Titanium	Less	No	Yes	Greater	—	—	Decreases	Increases

CHAPTER FIVE

CONCLUSIONS

1.) Scanning electron microscopy and atomic force microscopy investigations of the as-composited fiber surface morphology indicates that the FP and Saphikon fiber surface roughness increased according to the fiber coating material as: uncoated, nickel coating, niobium coating, and titanium coating.

2.) High-temperature (between 373 K and 1423 K) cyclic oxidation studies of uncoated and coated fiber composites with ends exposed to the environment indicate severe interfacial oxide scale formation. In contrast, composites with fiber ends embedded in the matrix showed no presence of oxide scale formation.

3.) Two consolidation induced fiber fragment distributions were found: (1) a distribution consisting of uncoated and niobium-coated (representing weak fiber-coating, or fiber-matrix chemical reactions) fiber fragments having approximately equal numbers of short, intermediate, and long fragments, and (2) a distribution represented by the nickel and titanium coated (strong chemical reaction) fiber fragments consisting of short fragments.

4.) Room-temperature fractographic investigations indicate a ductile niobium interphase region in and a thermally cycled 7-vol.% NiAl-(Nb-Saphikon) composite. In contrast, a brittle interphase region was found in a 7-vol.% NiAl-(Ti-Saphikon) thermally cycled four times.

5.) The nickel- and niobium-coated fiber composites's average heating half-cycle CTE, measured above the knee temperature, were substantially less than the uncoated fiber composite. These results indicate that the high-temperature behavior of the nickel- and niobium-fiber composites were fiber dominated and, hence, good fiber-matrix adhesion was achieved.

6.) Strain ratcheting (composite shrinks upon each thermal cycle) occurred in the nickel- and niobium-coated fiber composites.

7.) The thermal strain response of 5- and 7-vol.% titanium-coated fiber composites lacked a knee and showed considerable shakedown upon thermal cycling.

9.) Of the three fiber coating materials investigated (titanium, nickel, and niobium), niobium emerges as the most favorable since the coating-matrix chemical reactions did not increase the amount of consolidation induced fiber damage, enhanced high-temperature adhesion was achieved, and some evidence of low-temperature interfacial ductility was observed.

BIBLIOGRAPHY

BIBLIOGRAPHY

Alam, M.K. and Jain, S.C., "The CVD Coating of Fibers for Composite Materials," J. Metals, **42**, 56-58 (1990).

Adamson, A.W., Physical Chemistry of Surfaces, Interscience, New York (1960).

Amato, R.A. and Yang, J.-M., "Status and Development of Nickel Aluminide (NiAl) Composites," Mat. Res. Symp. Proc., **350**, 203-212 (1994).

Amateau, M.F., "Progress in the Development of Graphite-Al Composites using Liquid Infiltration Technology," J. Comp. Mat., **10**, 289-296 (1976).

Anton, D.L. and Shah, D.M., "Mechanical Evaluation of FP Alumina Reinforced NiAl Composites", Mat. Res. Soc. Symp., **273**, 157-164 (1992).

Arnold, S.M., Arya V.K., and Melis, M.E., "Reduction of Thermal Residual Stresses in Advanced Metallic Composites by Application of a Compensating/Compliant Layer Concept," HITEMP Review 1990: Advanced High Temperature Engine Materials Technology Program, NASA, CP-10051, 28-1 to 28-11 (1990).

Arnold, S.M., Arya V.K., and Melis, M.E., "Reduction of Thermal Residual Stresses in Advanced Metallic Composites Based Upon a Compensating/Compliant layer Concept," J. Comp. Materials, **26**(9), 1287 (1992).

Arsenault, R.J. and Taya, M., "Thermal Residual Stress in Metal Matrix Composite," Acta Metall. Vol. 35, No. 3, 651-659 (1987).

Asthana, R., Tewari, S.N., and Bowman, R.R., "Influence of the Fabrication Technique on the Fiber Pushout Behavior in a Sapphire-Reinforced NiAl Matrix Composite," Metall. and Materials Trans., **26A**, Jan. 209-223 (1995).

Baker, I, Nagal, P., Liu, F., and Munroe, P.R., "The Effect of Grain Size on the Yield Strength of FeAl and NiAl," Acta Met. Mat., **39**(7), 1637 (1991).

Barrett, C. and Massalski, T.B., Structure of Metals, 3rd ed., Chap 10, 1980, New York, Pergamon Press.

Barin, I. and Knacke, O., Thermochemical Properties of Inorganic Substances, Springer, New York (1993).

Bhatt, R.T. and Grimes, H.J., Mechanical Behavior of Metal-Matrix Composites, edited by J.E. Hack and M.F. Amateaux, TMS of AIME, 1983, pp. 51-64.

Bourke, M.A.M, Goldstone, J.A., Stout, M.G., and A. Needleman, in Fundamentals of Metal Matrix Composites, Eds. Suresh, S., Mortensen, A., and A. Needleman, Butterworth-Heinmann, Boston, MA, 61-80 (1993).

Bowman, R.R. and Noebe, R.D., "Processing and Mechanical Evaluation of Continuous Fiber Reinforced NiAl Composites," HITEMP Review 1990: Advanced High Temperature Engine Materials Technology Program, NASA, CP 10051, 40-1 to 40-13, (1990)

Bowman, R.R., personal communication (1994).

Bowman, R.R., "Influence of Interfacial Characteristics on the Mechanical Properties of Continuous Fiber Reinforced NiAl Composites," Mat. Res. Soc. Symp., **273**, 145-155 (1992).

Bowman, R.R., Noebe, R.D., Raj, S.V., and Locci, I.E., "Correlation of Deformation Mechanisms with the Tensile and Compressive Behavior of NiAl and NiAl(Zr) Intermetallic Alloys," Metall. Trans., **23A**, 1493-1508 (1992).

Bowman, R.R., Misra, A.K., and Arnold, S.M., "Processing and Mechanical Properties of Al_2O_3 Fiber-Reinforced NiAl Composites," Met. and Mat. Trans., **26A**, 615-628.

Broutman, L. J. and Krock, R.H., Composite Materials Volume 1: Interfaces in Metal Matrix Composites, Academic Press, New York, NY, 1974.

Broutmann, L. and Krock, R.: Modern Composite Materials, Addison-Wesley Publishing Co., 1967.

Chawla, K.K., Composite Materials, eds., B. Ilschner and N.J. Grant, Springer-Verlag, New York (1987).

Clark, R.W. and Whittenberger, J.D., "Thermal Expansion of Binary CoAl, FeAl, and NiAl Alloys," in Thermal Expansion 8, ed., T.A. Hahn, New York Plenum Press, 189-196 (1984).

Clyne, T.W. and Withers, P.J., An Introduction to Metal Matrix Composites, Cambridge Univ. Press, New York, NY (1993).

Clyne, T.W., "A Compressibility-based Derivation of Simple Expressions for the Transverse Poisson's Ratio and Shear Modulus of an Aligned Long Fiber Composite," J. Mat. Sci. Letts., **B9**, 336-339 (1990).

Copper, M.J., "The Electron Distribution in the Phases of CoAl and NiAl," Philos. Mag., **8**, 811-821 (1963).

Cotton, J.D., Noebe, R.D., and Kaufman, M.J. , "Ternary Alloying Effects in Polycrystalline β-NiAl, Structural Intermetallics, Eds. R. Darolia, J.J. Lewandowski, C.T. Liu, P.J. Martin, D.B. Miracle, and M.V Nathal, TMS, 513-522, 1993

Cox, H.L., "The Elasticity and Strength of Paper and other Fibrous Materials," Brit. J. Appl. Physics, **3**, 73-79 (1952).

Crispin, R.M. and Nicholas, M.G., "The Wetting and Bonding Behavior of Some Nickel Alloy-Alumina Systems," J. Mater. Sci., **11**, 17-21 (1976)

Curtin, W.A., "Exact Theory of the Fiber Fragmentation in a Single-Filament Composite," J. Mat. Sci., **26**, 5239-5253 (1991).

Delannay, F. Froyen, L., and Deruyterre, "Wetting of Solids by Liquid Metals in Relation to Squeeze Casting of MMCs, in Cast Reinforced Metal Composites, eds. S.G. Fishman and A.K. Dhingra, ASM, 81-84 (1988).

Darolia, R., "NiAl Alloys for High-Temperature Structural Applications," J. of Metals, **43**, 44-49 (1991).

Darolia, R., "NiAl for Turbine Airfoil Applications," Structural Intermetallics, Eds. R. Darolia, J.J. Lewandoski, C.T. Lui, P.L. Martin, D.B. Miracle, and M.V. Nathal, TMS, 495-504 (1993).

DeSilva, A.R.T. and Chadwick, G.A., "Thermal Stresses in Fiber Reinforced Composites," J. Mech. Phys. Solids, **17**, 387-403 (1969).

Doychak, J. and Ruhle, M., "TEM Studies of Oxidized NiAl and Ni_3Al Cross Sections," Oxidation of Metals, Vol. 31, Nos. 5/6, 431-452 (1989).

Doychak, J., Nesbitt, J. A., Noebe, R.D., and Bowman, R.R., "Oxidation of Al_2O_3 Continuous Fiber-Reinforced/NiAl Composites," Oxidation of Metals, **38**, (1/2), 45-71 (1992).

Doychak, J., Smialek, J.K., and Mitchell, T.E., "Transient Oxidation of Single-Crystal β-NiAl," Met. Trans., **20A**, 499 (1989).

Drzal, L.T., Rich, M.J., and Floyd, P.F., "Adhesion of Graphite Fibers to Epoxy Matrices: I. The Role of Fiber Surface Treatment," J. Adhes., **16**, 1-30 (1982).

Dutta, I., Mitra, S., and Wiest, A.D., "Some Effects of Thermal Residual Stresses on the Strain Response of Graphite-Aluminum Composites During Thermal Cycling," in Residual Stresses in Composites: Measurement, Modeling, and Effects on Thermo-Mechanical Behavior eds. E.V. Barrera and I.Dutta, TMS 273-292 (1993).

Dwight, A.E., Intermetallic Compounds, ed., J.H. Westbrook, Chap. 10, Huntington, NY, R.E. Krieger Pub (1977).

Elssner, G., Suga, T., and Turwitt, M., "Fracture of Ceramic-to-Metal Interfaces," J. Phys. Colloq. (France), **46** (C-4), 597 (1985).

Everett, R.K., "Deposition Technologies for MMC Fabrication," Metal Matrix Composites: Processing and Interfaces, eds., R.K. Everett and R.J. Arsenault, Academic Press, Boston, MA, 103-109 (1991).

Garmong, G., "Elastic-Plastic Analysis of Deformation Induced by Thermal Stress in Eutectic Composites: I. Theory," Metallurgical Transactions, Vol. 5, 2183-2190 (1974).

Garmong, G., "Elastic-Plastic Analysis of Deformation Induced by Thermal Stress in Eutectic Composites: II. Thermal Expansion," Metallurgical Transactions, Vol. 5, 2191-2197 (1974).

Garmong, G., "Elastic-Plastic Analysis of Deformation Induced by Thermal Stress in Eutectic Composites: III. Thermal-Cycling Damage," Metallurgical Transactions, Vol. 5, 2199-2205 (1974).

Gebhardt, E. and Rothenbacher, R.Z., "Untersuchgen im System Niob-Sauerstoff," Z. Metallkd., **54**, 623 (1963).

Glushko, V.I., Kovalenko, V.P., Mileiko, S.T., and Tvardovsky, V.V., "Evaluation of the Fiber Strength Characteristics on the Basis of the Fiber Fragmentation Test," J. Mat. Sci., **28**, 6307-6312 (1993).

Grimes, H.H., Lad, R. A., and Maisel, J.E., "Thermal Degradation of the Tensile Strength of Unidirectional Boron/Aluminum Composites," Metal. Trans., Vol. 8A, 1999-2005 (1977).

Groves, G.W. and Kelly, A., "Independent Slip Systems in Crystals," Philos. Mag., **8**, 877-887 (1963).

Handwerker, C.A., Cahn, J.W., and Manning, J.R., "Thermodynamics and Kinetics of Reactions at Interfaces in Composites," Materials Science and Eng., **A126**, 173-189 (1990).

Hartley, M.V., "The Effect of Isothermal Exposure on the Mechanical Properties of a Continuous Fiber Reinforced Titanium Matrix Composite," Mechanical and Physical Behavior of Metallic and Ceramic Composites, 9th Riso Int. Symp., eds., S.I. Anderson, H. Lilholt and O.B. Pedersen, Riso Nat. Lab., Denmark, 383-390 (1988).

Henrich, V.E., Surfaces and Interfaces of Ceramic Materials, Ed. L.-C. Dufour, Kluwer Academic, Norwell, MA (1989).

Hellman, J.R., Koss, D.A., Moose, C.A., Petrich, R.R., and M.N. Kallas, "Interfacial Shear Studies in Sapphire-Fiber Reinforced Niobium and Nickel Aluminide Composites," in HITEMP Review, NASA CP-10051, 41-1 to 41-11 (1990).

Hindam, H.M. and Smeltzer, W.W., "Growth and Microstructure of α-Al_2O_3 on β-NiAl," J. Electrochem. Soc. **127**, 1639 (1980).

Holliday, L. and Robinson, J., "Review: The Thermal Expansion of Composites Based on Polymers," J. Mater. Sci., **8**, 301 (1973).

Howe, J.M., "Bonding, Structure, and Properties of Metal/Ceramic Interfaces: Part 1 Chemical Bonding, Chemical Reaction, and Interfacial Structure," Int. Mat. Rev., Vol. 38, No. 5, 233-256 (1993).

Howe, J.M., "Bonding, Structure, and Properties of Metal/Ceramic Interfaces: Part 2 Interface Fracture Behavior and Property Measurement," Int. Mat. Rev., Vol. 38, No. 5, 233-256 (1993).

Igarashi, M. and Senba, H., "High Temperature Deformation and Oxidation Resistance of NiAl Based Intermetallic Compounds," Structural Intermetallics, Eds., R. Darolia, J.J. Lewandowski, C.T. Liu, P.L. Martin, D.B. Miracle and M.V. Nathal, TMS (1993)

Iwasa, M. and Bradt, R.C., Structures and Properties of MgO and Al_2O_3 Ceramics, Ed. W.D. Kingery, Am. Ceram. Soc., Columbus, OH, 767 (1984).

James, M.R., and O. Buck, in CRC Critical Reviews in Solid State and Materials Science, **61**, 105-109 (1980).

Jansson, S. and Leckie, F.A., "Reduction of Thermal Stresses in Continuous Fiber Reinforced Metal Matrix Comosites With Interface Layers," J. Comp. Materials, **26**(10), 1474 (1992).

Jedlinski, J. and Mrowec, S., "The Influence of Implanted Yttrium on the Oxidation Behavior of β-NiAl," Mat. Sci. and Eng., **87**, 281-287 (1987).

Jero, P. D., Parthasarathy, T. A. and Kerans, R.J., "Interface Evaluation in Ceramic Composites," NATO AGARD Conference, Autalya, Turkey, 21-22 April 1993.

Katzman, H.A., "Fiber Coatings for the Fabrication of Graphite Reinforced Mg Composites," J. Mat. Sci., **22**, 144-148 (1987).

Kelly, A. "Reinforcement of Structural Materials by Long Fibers," Met. Trans. **3**, 2313 (1972).

Kelly, A. and Tyson, W.R., "Tensile Properties of Fiber-Reinforced Metals: Copper/Tungsten and Copper/Molybdenum," J. Mech. Phys. Solids, Vol. 13, 329-350 (1965).

Khadkikar, P.S., Michal, G.M., and K. Vedula, "Preferred Orientation in Extruded Nickel and Iron Aluminides," Metall. Trans., **21A**, 279-288 (1990).
Kieschke, R.R., Somehk, R.E., and Clyne, T.W., "Sputter Deposited Barrier Coatings on SiC Monofilaments for use in Reactive Metallic Matrices - Part I: Optimization of Barrier Structure," Acta Met. et Mat., **39**,427-436 (1991).

Kingery, W.K., Bowen, H. K., and Ulhman, R., Introduction to Ceramics, Wiley, New York, 210 (1976).

Kinloch, A.J., Gledhill, R.A., and Dukes, W.A., in Adhesion Science and Technology, ed. L.H. Lee, Plenum Press, 597 (1975).

Klein, M.J., Reid, M.L., and Metcalfe, A.G., "Compatibility Studies for Viable Titanium Matrix Composites," AFML-TR-69-242, (1969).

Klomp, J.T., in "Ceramic Microstructures '86, Role of Interfaces," eds. J.A. Pask and A.G. Evans, New York, Plenum Press, 307, (1987).

Kyono, T., Hall, I.W., and Taya, M., Composites '86: Recent Advances in Japan and the United States, edited by K. Kawata *et al.* Japan Society for Composite Materials, 1986, pp. 553-561.

Larsson, L.O.K. "Thermal Stresses in Metal Matrix Composites," ICCM/2, Metallurgical Society of AIME, April 16, 1978, Toronto, Canada, 805-821.

Lenev, L.M. and Novokhatskii, I.A., "Thermodynamic Characteristics of $NiAl_2O_4$," Russ. J. Inorgan. Chem., **10**, 1307 (1965).

Ludwik, P., Elemente der Technologischen Mechanik, Springer, Berlin, p. 92 (1909).

Mackay, R.A., Brindley, P.K., and Froes, F.H., "Continuous Fiber-Reinforced Titanium Aluminide Composites," JOM, **43**, 23-31 (1991).

Manor, A. and Clough, R.B., "In-situ Determination of Fiber Strength and Segment Length in Composites by Means of Acoustic Emission", Composite Science and Technology, **45**, 73-81 (1992).

Masutti, D., Lentz, J.P., and Delannay, F., "Measurement of Internal Stresses and of the Temperature Dependence of the Matrix Yield Stress in Metal Matrix Composites from Thermal Expansion Curves," J. Mater. Sci. Let., **9**, 340-342 (1990).

McCullough, C. and Kieschke, R.R., "Fiber Coating Performance in TiAl," Mat. Res. Soc. Symp. Proc., **350**, 119-124 (1994).

McDonald, J.E. and Eberhart, J.G., "Adhesion in Aluminum Oxide-Metal Systems," Trans. AIME, **233**, 512 (1965).

Metcalfe, A.G., Composite Materials, Vol. 4 Metallic Matrix Composites, ed. K.G. Kreider, New York, Academic Press, 269 (1974).

Metcalfe, A.G. and Klein, M.J., Composite Materials, Vol. 1 Interfaces in Composites , eds. Broutmann and Krock, Academic Press, 125-168 (1972).

Min, B.K., in Advances in Composite Materials and Structures, eds. S.S. Wang and Y. Rajapakse, ASME, New York, in press.

Miracle, D.B., smith, P.R., and Graves, J.A., "A Review of the Status and Developmental Issues for Continuously-Reinforced Ti-Aluminide Composites for Structural Applications," Mat. Res. Soc. Symp. Proc., **350**, 133-142 (1994).
Miracle, D.B., "The Physical and Mechanical Properties of NiAl," Acta Metall. Mater., Vol 41, No. 3, 649-684 (1993).

Misra, A.K., Crandall, K.S., and Bowman, R.R., "Modification of Interface in Al_2O_3/NiAl Composite," HITEMP Review 1992: Advanced High Temperature Engine Materials Technology Program, NASA, CP 10104, 39-1 to 39-15 (1992).

Misra, A.K., "Thermodynamic Analysis of Chemical Interactions Between Reinforcement Materials and Matrices in Aluminide-Based High Temperature Intermetallic Matrix Composites", Interfaces in Metal-Ceramic Composites, eds. R.Y. Lin, R.J. Arsenault, G.P. Martins and S.G. Fishman, TMS, 85-102 (1989).

Misra, A.K., Bowman, R.R., Locci, I.E., and Matthiesen, M.M., "Interface Mo Coatings for Al_2O_3/NiAl Composite," HITEMP Review 1993: Advanced High Temperature Engine Materials Technology Program, NASA, CP 19117, 58-1 to 58-13 (1993).

Moose, C.A., Koss, D.A., and Hellman, J.R., "Interfacial Shear Behavior of Sapphire-Reinforced NiAl Composites," Mat. Res. Soc. Symp., **194**, 293-299 (1990).

Morel, M. and Saravanos, D.A. "Computational Procedure to Tailor Compliant Layer Characteristics and Processing History for Minimal Residual Stresses," HITEMP Review 1990: Advanced High Temperature Engine Materials Technology Program, NASA, CP 10051, HITEMP, 44-1 to 44-9, (1990).

Morozuni, S., Kikuchi, M.and Nishino, T., "Bonding Mechanism between Alumina and Niobium", J. Mater. Sci. **16**, 2137-44 (1981).

Murr, L.E., Interfacial Phenomena in Metals and Alloys, Addison-Wesley, Reading, MA, (1975).

Meyers, M.A. and Chawla, K.K., Mechanical Metallurgy: Principles and Applications, Prentice-Hall, New Jersey (1984).

Nagpal, P. and Baker, I., "The Effect of Grain Size on the Room-Temperature Ductility of NiAl," Scr. Met. et Mat., **24**, 2381 (1990).

Netravali, A.N., Topoleski, L.T.T., Sachse, W.H., and Phoenix, S.L. , "An Acoustic Emission Technique for Measuring Fiber Fragment Length Distributions in the Single-Fiber-Composite Test," Comp. Sci. and Tech., **35**, 13-29 (1989).

Nicholas, M.G., Surfaces and Interfaces of Ceramic Materials, ed. L.-C. Dufour, Kluwer Academic, Norwell, MA (1989).

Noebe, R.D., Bowman, R.R., and Eldridge, J.I., "Initial Evaluation of Continuous Fiber Reinforced NiAl Composites," Mat. Res. Soc. Symp., **194**, 323-331 (1990).

Noebe, R.D., Bowman, R.R., and Nathal, M.V., "Physical and Mechanical Properties of the B2 Compound NiAl," Int. Mat. Rev., Vol. 38, No. 4, 193-232 (1993).

Ochiai, S., Okuda, S., Shimonmura, K., and Murakami, Y., "Effects of Interfacial Conditions on the Shear Strength of the Interface and Critical Aspect Ratio in Tungsten-Copper Composites," Trans. JIM, Vol. 17, 649-654 (1976).

Ochiai, S. and Osamura, K , "Multiple fracture of a Fiber in a Single Tungsten Fiber-Copper Matrix Composite," Z. Metallkde, **77**, 255-259 (1986).
Ohuchi, F.S. and Kohyama, M., "Electronic Structure and Chemical Reactions at Metal-Alumina and Metal-Aluminum Nitride Interfaces," J. Am. Cer. Soc., **74** (6), 1163-87 (1991).

Okamoto, H., "Ni-Al," J. Phase Equilibria, **14**(2), 257 (1993).

Paley, M., and Aboudi, J., "Micromechanical Analysis of Composites by the Generalized Cell Model," Mechanics of Materials, **14**, 127-133 (1992).

Polvani, R.S., Tzeng, W.-S., and Strutt, P.R., "High Temperature Creep in a Semi-Coherent NiAl-Ni_2AlTi Alloy," Met. Trans., **7A**, Jan. 33-40 (1976).

Park, Y.H. and Marcus, H.L., Mechanical Behavior of Metal-Matrix Composites, edited by J.E. Hack and M.F. Amateaux, TMS of AIME, 1983, pp. 65-75.

Parthasarathy, T.A., Marshall, D.B., and Kerans, R.J., "Analysis of the Effect of Interfacial Roughness on Fiber Debondiing and Sliding in Brittle Matrix Composites," Acta Metall. Mater., **42**, No. 11, 3773-3784 (1994).

Pascoe, R.T. and C.W.A. Newey, "The Mechanical Behavior of the Intermediate Phase of NiAl", Met. Sci. J., **2**, 138-143 (1968).

Pauling, L. "The Nature of the Chemical Bond", 2nd ed., New York, Cornell University Press, 69 (1948).

Pettit, F.S., "Oxidation Mechanisms for Nickel-Aluminum Alloys at Temperatures Between 900° and 1300° C," Trans. Met. Soc. AIME **239**, 1296 (1967).

Pindera, M-J., Freed, A.D., and Arnold, S.M., "Effects of Fiber and Interfacial Layer Morphologies on the Thermoplastic Response of Metal Composites," Int. J. Solids and Structures, **30** (9), 1213-1238 (1993).

Pierik, S.M., Baker, D.R. and Kaufman, M.J., "Preliminary Interfacial Study on NiAl Matrix Composites", Fundamental Relationships Between Microstructure and Mechanical Properties of Metal-Matrix Composites, Eds. P.K. Liaw and M.N. Gungor, TMS, 341-352 (1990).

Pierson, H.O. and Randich, E., "Titanium Diboride Coatings and Their Interaction with Substrates", Thin Solid Films, **54**, pp. 119-128. (1978).

Polvani, R.S., Tzeng, W.S., and Strutt, P.R, "High Temperature Creep in a Semi-Coherent NiAl-Ni_2AlTi Alloy," Metall, Trans. **7A**, 33-40 (1976).

Pysher, D.J. and Tressler, R.E., "Creep Rupture Studies of Two Alumina-Based Ceramic Fibers," J. Mater. Sci., **27**, 423-428 (1992).

Reddy, S.N.S, Betrabet, H.S., Purushothaman, S.P., and Narayan, C., "Interface Mixing Between Metals and Ceramics: Classification, Thermochemistry, and Processing," Ceram. Eng. Sci. Proc. **10**[11-12], 1696-1707 (1989).

Reed-Hill, R.E., Physical Metallurgy Principles, 2nd ed., Litton Educational Publishing, Inc. (1973).

Rusovic, N. and H. Warlimont, "Young's Modulus of β_2-NiAl Alloys," Phys. Status Solidi (a), **53**, 283-288 (1979).

Schapery, R.A., "Thermal Expansion Coefficients of Composite Materials Based on Energy Principles," J. of Composite Materials, Vol. 2, no. 3, 380-401 (1968).

Schulson, E.M. and Barker, D.R., "A Brittle to Ductile Transition in NiAl of a Critical Grain Size," Scripta Metallurgica, **17**, 519-522 (1983).

Shahinian, P., "High-Temperature Strength of Sapphire Filament," J. Am. Cer. Soc., Vol. 54, No. 1, 67-68 (1971).

Shankar, S. and Seigle, L.L., "Interdiffusion and Intrinsic Diffusion in the NiAl (δ) Phase of the Al-Ni System," Metall. Trans., **9A**, 1978 1467-1476 (1978).

Shida, Y., Stott, F.H., Bastow, B.D., Whittle, D.P., and Wood, G.C., " Development of Preferential Intergranular Oxides in Nickel-Aluminum Alloys at High Temperatures," Oxidation of Metals, Vol. 18, Nos. 3/4, 93-113 (1982).

Speyer, R.F., Thermal Analysis of Materials, Marcel Dekker, New York, N.Y. (1994).

Stacy, M.H., "Development in Continuous Alumina-Based Fibers," Br. Ceram. Trans. J., **87**, 168-172 (1988).

Stoloff, N.S., "Ordered Alloys-Physical Metallurgy and Structural Applications," International Metals Reviews, **29**, No. 3, 123-135 (1984).

Stott, F.H. and Ashby, D.J., "The Oxidation Characteristics of Electrodeposited Nickel Composites Containing Silicon Carbide Particles at High Temperature," Corros. Sci., **18**, 183-198 (1978).

Strutt, P.R. and Kear, B.H., "Creep in Ordered Nickel Base Alloys," High Temperature Ordered Intermetallic Alloys, eds. C.C. Koch, C.T. Liu and N.S. Stoloff, Mat. Res. Sym. Proc. 39, 288-292 (1985).

Taya, M. and Arsenault, R.J., Metal Matrix Composites: Thermomechanical Behavior, Pergamon Press, New York, N.Y. (1989).

Taya, M. and Mori, T., in Proc. IUTAM Symp.: Thermo-mechanical Couplings in Solids, eds. H.D. Bui and Q.S. Nguyen, Elsevier, Amsterdam (1987).

Traumbauer, E.R., Hellman, J.R., Shelleman, D.L., and Koss, D.A., "Effect of Fiber Surface Cleaning Procedures on Tensile Strength of Sapphire Fibers," HITEMP Review 1992: Advanced High Temperature Engine Materials Technology Program, NASA, CP 10104, HITEMP, 16-1 to 16-9, (1992)

Tressler, R.E. and Barber, D.J., "Yielding and Flow of c-Axis Sapphire Filaments," J. Am. Cer. Soc., Vol. 57, No. 1, 13-19 (1974).

Tressler, R.E., Moore, T.L., and Crane, R.L., "Reactivity and Interface Characteristics of Titanium-Alumina Composites," J. Mater. Sci., **8**, 151 (1973).

Theocaris, P. S. and Demakos, C.B., "The Influence of the Elastic Properties and Dimensions of Coatings on the Stiffness of Encapsulated Fiber Composites," Composites Science and Technology, **45**, 293-305 (1992).

Touloukiasn, Y.S., Kirby, R.K., Taylor, R.E., and Desai, P.D., "Thermal Expansion - Metallic Elements and Alloys," IFI/Plenum, New York, 17a (1975).

Turwitt, M. Elssner, G., and Petzow, G., "Manufacturing and Mechanical Properties of Interfaces Between Sapphire and Niobium," J. Phys. Colloq. (France), **46** (C-4), 123 (1985).

Tyson, W.R., "Discussion of "Elastic-Plastic Analysis of Deformation Induced by Thermal Stress in Eutectic Composites," Metallurgical Transactions A, Vol. 6A, 1674-1677 (1975).

Urquhart, E.E., Arnold, S.M., Pindera, M-J., and Aikin, B. J. M., "Simulation of Experimentally Observed Thermal Expansion Behavior of FeCrAlY Based Composites," HITEMP Review 1993: Advanced High Temperature Engine Materials Technology Program, NASA, CP 10051, 54-1 to 54-11 (1993).

Vincent, H., Vincent, C., Ponthenier, J.L., Mourichoux, H., and Bouix, J., "Elaboration en Continu d'un Depot Mince de Carbure Refractaire en Surface des Fibres de Carbone: Caracterisation de la Fibre C/SiC", in *Proc. 3rd European Conf. on Comp. Mat. (ECCM3)*, eds. A.R. Bunsell, P. Lamicq, and A. Massiah, Elsevier, 257-264 (1989).

Wang, H.F., Gerberich, W.W., and Skowronek, C.J., "Fracture Mechanics fo Ti/Al_2O_3 Interfaces," Acta Metall. Mater., Vol. 41, No. 8, 2425-2432 (1993).

Wakashima, K.,Otsuka, M., and Umekawa, S., "Thermal Expansions of Heterogeneous Solids Containing Aligned Ellipsoidal Inclusions," J. Compos. Mater., **8**, 391-404 (1974).

Walston, W.S., Field, R.D., Dobbs, J.R., Lahrman, D.F., and Darolia, R., "Microstructure and High Temeprature Strength of NiAl Alloys," Structural Intermetallics, Eds. R. Darolia, J.J. Lewandoski, C.T. Lui, P.L. Martin, D.B. Miracle, and M.V. Nathal, TMS, 523-532 (1993).

Ward-Close, C.M. and Partridge, P.G., "A Fibre Coating Process for Advanced Metal-Matrix Composites," J. Mat. Sci. **25**, 4315-4323 (1990).

Warren, R. and Andersson, C.-H., "Silicon Carbide Fibers and Their Potential for Use in Composite Materials: Part II," Composites, **15**, 101(1984).

Warwick, C.M., Kieschke, R.R., and Clyne, T.W. "Measurement and Control of the Stress State in Sputtered Diffusion Barrier Coatings on Monofilaments," in Interfacial Phenomena in Compsoite Materials, F.R. Jones (ed.) Butterworth, 267-275 (1989).

Warwick, C.M. and Clyne, T.W., "The Micromechanisms of Strain Ratchetting During Thermal Cycling of Fibrous MMCs," Fundamental Relationships Between Microstructure and Mechanical Properties of Metal-Matrix Composites, eds., P.K. Liaw and M.N. Gungor, TMS, 209-223 (1990).

Warwick, C.M. and Clyne, T.W., "Development of Composite Coaxial Cylinder Stress Analysis Model and its Application to SiC Monofilament Systems," J. Mat. Sci., **26**, 3817-3827 (1991).

Wasynczuk, J.A. and Ruhle, M. in "Ceramic Microstructures '86, Role of Interfaces," eds. J.A. Pask and A.G. Evans, New York, Plenum Press, (1987).

Waterbury, M., Matikas, T., Karpur, P., and Krishnamurthy, K., "In-situ Ultrasonic Imaging and Acoustic Emission Monitoring of Single Fiber Fragmentation in Metal Matrix Composites," TMS Fall Meeting, Pittsburgh, PA, (1993).

Weber, C.H., Yang, J.Y., Lofvander, J.P.A., Levi, C.G., and Evans, A.G., "The Creep and Fracture Resistance of γ-TiAl Reinforced with Al_2O_3 Fibers," Acta Metall. Mater. Vol. 41, No. 9, 2681-2690 (1993).

Weddle, J.K., "Continuous Ceramic Fibers," J. Text. Inst., **81**, No. 4, 333-359 (1990).

Wei, W., "The Effect of Long Term Exposure on the Interfacial Chemistry and Mechanical Properties of Metal Matrix Composites," Fundamental Relationships Between Microstructure and Mechanical Properties Of Metal Matrix Composites, eds., M.N. Gungor and P.K. Liaw, TMS, 353-370 (1990).

Wiederorn, S.M., Hockey, B.J., and Roberts, D.E., "Effect of Temperature on the Fracture of Sapphire," Philos. Mag., 28, 783-796 (1978).

Whittenberger, J.D., Viswanadham, R.K., Mannan, S.K. and Kumar, K.S., "1200 to 1400 K Slow Strain Rate Compressive Properties of NiAl-Ni2AlTi Base Materials", High Temperature Ordered Intermetallic Alloys III, C.T. Liu, A.I. Taub, N.S. Stoloff and C.C. Koch, eds., Vol. 133, (Materials Research Society, Pittsburgh, PA, 621-626 (1989).

Whittenberger, J.D., Westfall, L.J. and Nathal, M.V., "Compressive Strength of a B2 Matrix NiAl-Nb Intermetallic at 1200 and 1300 K," Scr. Metall., **23**, 2127-2130 (1989).

Whittenberger, J.D., "The Influence of Grain Size and Composition on 1000 to 1400 K Slow Plastic Flow Properties of NiAl," J. Mater. Sci., **23**, 235 (1988).

Whittenberger, J.D., Gaydosh, D.J., and Kumat, K.S., "1300 K Compressive Properties of Several Dispersion Strengthened NiAl Materials," J. Materials Sci., **25**, 2771-2776 (1990).

Whittle, D.P. and J. Stringer, "Improvements in High Temperature Oxidation Resistance by Additions of Reactive Elements or Oxide Dispersions," Phil. Trans. R. Soc. Lond. (GB), **A295** (1413), 309 (1980).

Whitney, J.M. and L.T. Drzal, "Axisymmertic Stress Distribution Around an Isolated Fiber Fragment," in Toughened Composites, ASTM Special Technical Publication, 179-196 (1985).

Wright, M.A., "The Effect of Thermal Cycling on the Mechanical Properties of Various Aluminum Alloys Reinforced with Unidirectional Boron Fibers," Metal. Trans., Vol. 6A, 129-134 (1975).

Xia, Z., "Role of Coatings in Axial Tensile Strength of Long Fiber-Reinforced Metal-Matrix Composites," Acta Metall. Mater. Vol 41, No. 7, 2097-2104 (1993).

Yano, T.; Yanagisawa, O., and Ohmuri, M., "Defromation of a Fiber-reinforced Composite Induced by Temperature Change and External Loading," J. Jpn. Inst. Metals, **52**, 229-235 (1988).

Yoda, S., Kurihara, N., Wakashima, K., and Umekawa, S., "Thermal Cycling-Induced Deformation of Fibrous Composites with particular reference to the Tungsten-Copper System," Metal Trans., Vol. 9A, 1229-1236 (1978).

Yoda, S., Takahashi, R., Wakashima, K., and Umekawa, S., "Fiber/Matrix Interface Porosity Formation in Tungsten Fiber/Copper Composites on Thermal Cycling," Metal Trans., Vol. 10A, 1796-1798 (1979).

Zener, C., "Theory of Growth of Spherical Precipitates from Solid Solutions," J. Appl. Phys. **20**, 950 (1949).

Zhang, H., Anderson, P.M., and Daehn, G.S., "Analysis of Thermally Induced Stress and Strain in Continuous Fiber-Reinforced Composites," Met. Trans. A, Volume 25A, 1-11 (1994).